Taxonomic predictions of seabird identity using 3D bone shape

A thesis presented in partial fulfilment of the requirements for the degree of

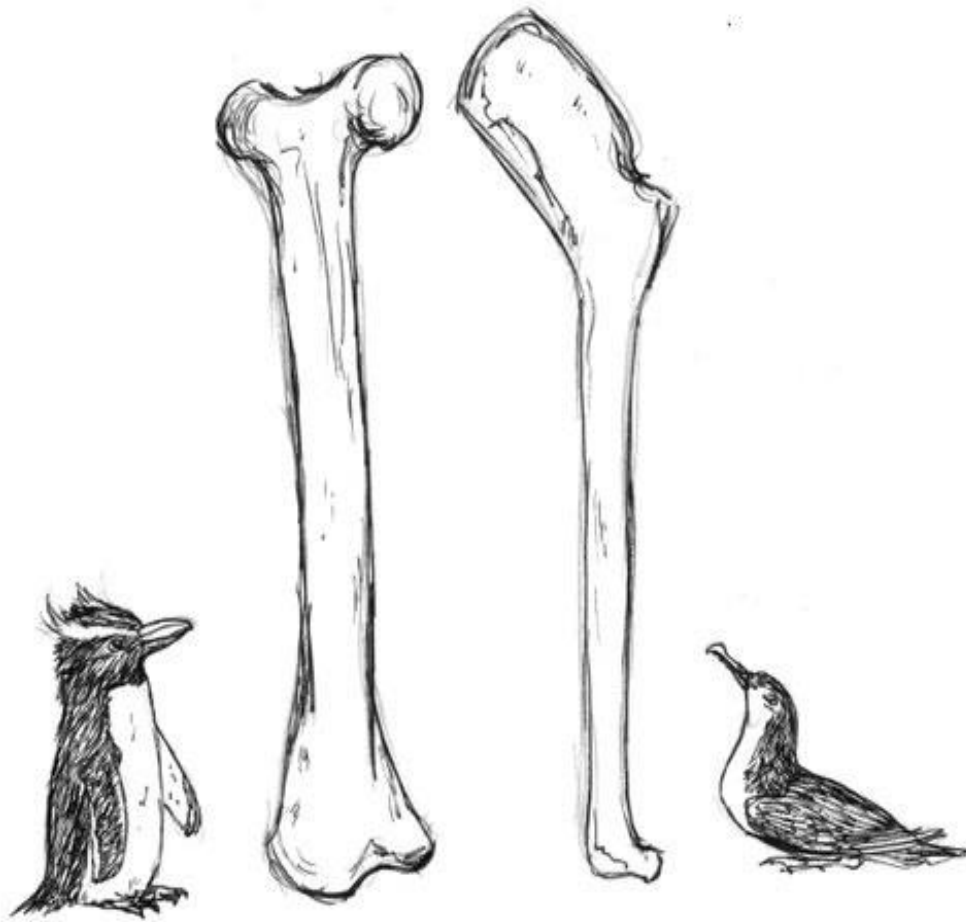Master of Science
in
Zoology

at Massey University, Albany,
New Zealand.

Emma Jane Holvast

2021

MASSEY UNIVERSITY
TE KUNENGA KI PŪREHUROA
UNIVERSITY OF NEW ZEALAND

Erect crested penguin (*Eudyptes sclateri*) (left), seabird femur and humerus (centre), and rako / Buller's shearwater (*Puffinus bulleri*) (right). Sketched by Edin Whitehead on June 06 during the presentation of: Holvast EJ, Thomas DB. Taxonomic predictions of seabird identity using 3D bone shape. NZ Bird Conference 2021. 05-06 June, Thames, New Zealand.

Image credit: Edin Whitehead @edinatw.

Abstract

Identifying a species from an isolated bone can be an important first step in faunal analysis research. Identifications using molecular methods are not always possible (e.g. fossils), and specialist taxonomic expertise is not always available. Here we have investigated a shape-based (i.e. geometric morphometric) method for identifying taxa from a single bone that doesn't require specialised taxonomic knowledge. Three-dimensional (3D) shape analyses are routinely used to study variation in bone shape among species, primarily to understand the role of environment and other drivers of shape evolution. Here we used 3D geometric morphometrics to predict taxonomic identities for seabird bones using partial least squares discriminant analysis (PLS-DA). We tested the hypothesis that digitised humeri and femora from seabirds can be confidently classified at order- or family-level using PLS-DA. Our analytical protocol aimed to accurately assign a bird bone to the correct taxonomic family, given that family-level analyses are useful for both modern and fossil bones. This protocol emphasised a minimal knowledge of osteological terminology on the part of the user, and instead used 3D geometric morphometrics and partial least squares discriminant analysis. Datasets of digitised seabird humeri and femora were generated from the collections at Auckland War Memorial Museum, Canterbury Museum and Te Papa Tongarewa Museum of New Zealand. Our novel taxonomic classification protocol used both well-established landmark-based techniques and novel landmark-free methods. Both the bootstrap and repeated cross-validation partial least squares discriminant analysis models as applied to both femur and humerus shape were highly successful in their ability to correctly predict new samples into their respective classes at both order- and family-level. Landmark-based PLS-DA assigned femora from penguins and tubenosed birds to the correct order and family with 100% and 93.5% accuracy, respectively. Pseudolandmark-based PLS-DA assigned femora and humeri from penguins and tubenosed birds to both the correct order and family with 100% accuracy. These results are a promising indication of the future utility of this method which may allow for taxonomic identification using more-automated landmark-free shape analysis techniques. Furthermore, this method could be used to produce finer-level classifications (genus or species), and could be applied to groups beyond seabirds.

Keywords: classification, bone, seabird, taxonomy, geometric morphometrics, partial least squares discriminant analysis, New Zealand

Acknowledgements

First and foremost, I thank my supervisor Daniel Thomas. For everything. Words cannot describe how grateful I am for all that you have taught me and done to help me over the (I lose count how many) years that we have worked together. I greatly appreciate the opportunity to work on such an amazing and enjoyable research project. Thank you for the incredible effort that you put into not only my project, but also my development as a researcher. Thank you for your patience, counsel, endless support and reassurance, faith in my abilities, and the countless opportunities you have provided for my growth. I simply would not have made it to this point or be the researcher that I am without your encouragement and commitment. I feel incredibly privileged and proud to work with you.

I would like to thank a number of people and institutions for allowing me access to museum specimens, without which this study would not have been possible. A huge thank you to Ruby Moore, Collections Manager and Matt Rayner, Curator of Land Vertebrates at Auckland War Memorial Museum for granting me access to the seabird collections, and for your collaboration on our work with 3D bird bone models. A special thank you to Alan Tennyson, Senior Curator at Te Papa for sharing your Procellariiformes collections and expertise, for the opportunity to join in on a fossil dig, and for your ongoing support and encouragement of my research. Thanks also to Thomas Schultz, Jess Calcutt and Colin Miskelly at Te Papa for hosting me during my research visits. I really enjoyed my time working in the collections and appreciate that you were all so welcoming and accommodating. A special thank you to Paul Scofield, Senior Curator at Canterbury Museum for allowing me to visit the seabird collections, for your enthusiasm and encouragement of my project and furthermore for providing the exciting opportunity to study an unidentified fossil petrel specimen.

Financial support during this thesis was awarded through a Graduate Women North Shore Scholarship and the *Birds NZ* 2020 David Medway Scholarship. I would like to thank the Graduate Women North Shore Charitable Trust for their support and excitement for my research and its applicability, and everyone at the Ornithological Society of New Zealand for their support and enthusiasm for my project. I would like to acknowledge the Massey University Capital Equipment Fund which provided the 3D scanning equipment used for data collection in this study. I am also grateful for the financial support provided by the Massey University Research Fund which allowed me to undertake museum research visits to collect the data essential for this study.

I would like to thank my friends and colleagues, without whom I would not have made it this far. Simone for always being happy to chat and collaborate; I greatly appreciate the time and effort taken to help produce 3D models and for your advice and help throughout this project. Juliane, Claudia,

Table of Contents

List of Figures

List of Tables

1 Introduction

1.1 Seabirds

New Zealand is the seabird capital of the world for having over a third of all seabird species present in or around the country and for having the greatest diversity of seabird species for any one country (Taylor, 2000; Croxall et al., 2012; Forest & Bird, 2018). Around 25% of all seabird species breed in the New Zealand region and 10% of these species are endemic (Taylor, 2000; Gill et al., 2010; Thomas et al., 2020b).

Here the New Zealand region includes all islands in the New Zealand Exclusive Economic Zone ranging from the Kermadec Islands in the north to Campbell Island in the south and eastward to the Chatham Islands. Seabirds breeding in the New Zealand region represent four orders: Procellariiformes (i.e. the tubenosed birds - albatrosses, shearwaters, petrels and prions), Sphenisciformes (i.e. penguins), Charadriiformes (i.e. skuas and some terns) and Suliformes (i.e. gannets, frigatebirds and some cormorants) (Chown et al., 1998; Miskelly et al., 2008). Of these, the most diverse are the tubenosed birds (Marchant, 1990; del Hoyo et al., 1994; Gill et al., 2010).

The tubenosed birds are an order of pelagic seabirds that globally comprise more than 140 extant species within four families (Marchant, 1990; del Hoyo et al., 1994; Gill et al., 2010; Fischer, 2016; IUCN, 2021). This clade is widely distributed with taxa found in every ocean around the world but predominantly in the southern hemisphere (del Hoyo et al., 1994; Fischer, 2016; Stidworthy & Denk, 2018). Tubenosed birds are particularly abundant throughout New Zealand with 19 species endemic to the region (Taylor, 2000; Gill et al., 2010). The size diversity of tubenosed birds in New Zealand ranges from the very large wandering albatross *Diomedea exulans* weighing up to 11 kg with a wingspan of up to 3.5 m, to the very small New Zealand storm petrel *Fregetta maoriana* weighing 20 g with a wingspan of 32 cm (Marchant, 1990; del Hoyo et al., 1994; Taylor, 2000; Croxall et al., 2012; Fischer, 2016). Many tubenosed birds are threatened or at risk of extinction with 67 currently listed as either vulnerable, endangered or critically endangered globally according to the International Union for Conservation of Nature Red List (Stidworthy & Denk, 2018; IUCN, 2021). New Zealand is also home to endangered penguins.

Penguins (order Sphenisciformes) are flightless pelagic seabirds comprising six genera in a single family (Spheniscidae) (Jouventin & Dobson, 2018). Currently 18 penguin species are recognised by the International Ornithological Commission (IOC) World Bird List (Jouventin & Dobson, 2018; Gill et al., 2021). All but one of these species live only in the Southern Hemisphere with habitats ranging from cold Antarctic coasts and mainland (i.e. Emperor penguin *Aptenodytes forsteri*) to warm islands

at the equator (i.e. Galapagos penguin *Spheniscus mendiculus*) (Borboroglu & Boersma, 2015; Jouventin & Dobson, 2018). The Galapagos penguin is notable for having a range that reaches slightly across the equator thereby extending penguins into the northern hemisphere (Jouventin & Dobson, 2018). The greatest diversity of penguins can be found in the New Zealand region or its territories where seven species breed and another ten species have been recorded as vagrants (Robertson et al., 2016). Among those breeding in New Zealand is the kororā / little penguin *Eudyptula minor* which is commonly found along coasts of the mainland and surrounding islands (Marchant, 1990; del Hoyo et al., 1994; Cargill et al., 2020). Both the hoiho / yellow-eyed penguin *Megadyptes antipodes* and tawaki / Fiordland crested penguin *Eudyptes pachyrhynchus* breed along the shores of the South Island and Stewart Island and are endemic (Mattern et al., 2007; Borboroglu & Boersma, 2015). Along with tawaki, a further three crested penguin species (genus *Eudyptes*) breed on New Zealand's associated offshore islands and two of these species are endemic, Snares crested penguin *E. robustus* and erect-crested penguin *E. sclateri* (Sagar et al., 2001; Borboroglu & Boersma, 2015; Cole et al., 2019b; Mattern et al., 2021).

Six species of tern (order Charadriiformes) breed in the New Zealand region while another eight species are either vagrants or migrants (Robertson et al., 2016). Also within Charadriiformes are skuas, a group of predatory seabirds of which only the subantarctic skua *Catharacta antarctica lonnbergi* breeds in New Zealand (Gill et al., 2010; Robertson et al., 2016). Four other species of skua are migrants to New Zealand (Robertson et al., 2016). A number of non-seabird charadriiform species are also New Zealand residents e.g. banded dotterel *Charadrius bicinctus*, shore plover *Thinornis novaeseelandiae* (Gill et al., 2010; Robertson et al., 2016). Order Suliformes in New Zealand includes two species of frigatebird, three species of booby, three species of gannet, and the Australasian darter *Anhinga novaehollandiae* (Robertson et al., 2016). These species are all vagrants with the exception of the Australasian gannet *Morus serrator* which breeds on the mainland (Bunce et al., 2002; Robertson et al., 2016). Twelve species of shag (cormorant) either breed in New Zealand (including eight endemic species) or are vagrants to New Zealand (Gill et al., 2010; Croxall et al., 2012; Robertson et al., 2016). Although the clades Charadriiformes and Suliformes are part of the New Zealand avifauna they are not included in analyses hereafter.

1.2 Avifaunal analysis

Seabirds have a long history in the New Zealand region with the fossil record for penguins reaching back at least 60 million years (e.g. Slack et al., 2006; Jouventin & Dobson, 2018), while fossil Procellariiformes date back to at least 3 million years ago (e.g. Worthy et al., 2007; Henderson & Gill,

2010; Tennyson & Mannering, 2018; Mayr & Tennyson, 2020). New Zealand has an extraordinary Holocene fossil record of birds, with many well-preserved avian subfossil sites (i.e. <12,000 years ago) (Gill, 2006) and large numbers of bone assemblages, many of which have been recovered, identified and described (e.g. Worthy & Holdaway, 2002) (Duncan & Blackburn, 2004; Gill, 2006; Tennyson, 2010; Worthy et al., 2017). Many bird extinctions occurred in the Holocene (i.e. 0 to c. 12,000 years before present), all of which likely followed human arrival (Holdaway, 1989; Tennyson, 2010). These include for example, the laughing Owl *Sceloglaux albifacies* Gray, 1844; New Zealand Raven *Corvus antipodum* Forbes, 1893; and all nine species of moa (Dinornithiformes) (Gill et al., 2010; Worthy & Scofield, 2012; Worthy et al., 2017). Most Holocene bird extinctions are thought to be the result of human hunting, but predation by introduced taxa (predominantly mammals e.g. rats, cats), and the loss of prey also had significant impacts on the survival of the New Zealand avifauna (Tennyson & Martinson, 2006; Tennyson, 2010). Bone assemblages of procellariiform seabirds in particular are commonly found along coastlines and in midden deposits throughout both the mainland of New Zealand and its offshore islands (Wood, 2016).

Examination of the Holocene record in general has furthered our understanding in several areas of faunal research including taxonomy (e.g. Mitchell et al., 2014; Cole et al., 2019a), zooarchaeology (e.g. Eda et al., 2016a; Douglass et al., 2018), domestication (e.g. Vermeersch et al., 2015; Eda et al., 2016b), palaeoenvironmental reconstruction (e.g. Rawlence et al., 2012; Goodman et al., 2013; Rawlence et al., 2016), and conservation (e.g. Cooper et al., 1996; Rawlence et al., 2015) (Grealy et al., 2017). More specifically, several studies have analysed the Holocene record in the context of the extant and extinct New Zealand avifauna to investigate the taxonomy (i.e. taxonomic identifications, descriptions and revisions; e.g. Allentoft et al., 2012; Tennyson et al., 2015; Tennyson & Mannering, 2018), biogeography (e.g. Rawlence et al., 2017b), biology (e.g. Wood et al., 2008; Wood et al., 2017) and biodiversity turnover (e.g. Rawlence et al., 2015; Rawlence et al., 2017a) of these taxa.

For example, Cole et al. (2019a) discovered an extinct penguin species and subspecies that were endemic to the Chatham Islands using combined morphological and molecular (near-complete mitochondrial genomes) analyses of Holocene bones found in midden deposits. The two newly-described lineages were the extinct Chatham Island crested penguin *Eudyptes warhami* Cole, Tennyson, Ksepka & Thomas, 2019, and an extinct dwarf subspecies of the yellow-eyed penguin, *Megadyptes antipodes richdalei* Tennyson & Cole, 2019 (Cole et al., 2019a). Tennyson et al. (2015) confirmed the existence of an undescribed species of extinct gadfly petrel from bone remains found in Holocene fossil deposits on Chatham, Pitt and Mangere Islands, New Zealand. Combined morphological and molecular evidence (Ancient DNA; aDNA extracted using a novel method of soaking

DNA from bones) was used to identify and describe the new species *Pterodroma imberi* Tennyson, Cooper & Shepherd, 2015 (Tennyson et al., 2015). Rawlence et al. (2017b) investigated the biogeographic history of *Leucocarbo* shags on mainland New Zealand using combined genetic, morphometric and osteological analyses of Holocene subfossils. Three species of *Leucocarbo* shag, king *L. carunculatus*, Otago *L. chalconotus* and Foveaux *L. stewarti* were found to have had a much wider prehistoric (<1450 CE) distribution on mainland New Zealand prior to human arrival, when compared to their restricted modern ranges (Rawlence et al., 2017b). Furthermore, the authors described a new extinct species from the Holocene fossil material, Kohatu shag *Leucocarbo septentrionalis* Rawlence, Till, Easton, Spencer, Schuckard, Melville, Scofield, Tennyson, Rayner, Waters & Kennedy, 2017, whose distinctive northern New Zealand populations were previously assigned to the king shag (Rawlence et al., 2017b).

Family-level analyses based on the Holocene record have been useful for taxonomic classification of both modern and fossil bird bones. For example, Seersholm et al. (2018) analysed approximately 5,000 morphologically unidentifiable bone fragments from 38 different subfossil bone assemblages across New Zealand, using aDNA from Bulk Bone Metabarcoding (BBM) assays. DNA sequences from BBM corresponded to 635 taxa, of which 436 could be identified to at least family-level, including 54 different bird species (36 New Zealand endemics, and 13 extinct species) (Seersholm et al., 2018). This study demonstrated the value of aDNA in analysing fossil bone assemblages that comprise mostly nondiagnostic material i.e. bone fragments which are often unidentifiable using a traditional morphological approach (Seersholm et al., 2018).

The aim of my study was to develop a taxonomic classification method for individual bones using advanced 3D shape analyses, which may allow for the identification of bird remains if only undiagnostic bones are available or found in the field, and if molecular analysis is not possible or feasible. The focal orders for these analyses were Procellariiformes and Sphenisciformes which form the clade Austrodyptornithes (Yuri et al., 2013). Both well-established landmark-based techniques and novel landmark-free 3D geometric morphometric methods were used to predict taxonomic groups using partial least squares discriminant analysis (PLS-DA). The objective was to make order- and family-level predictions of bird bone taxonomy given that family-level analyses are useful for both modern and fossil bones.

The IOC World Bird List revisions (Gill et al., 2021) were used as authority on the latest taxonomic names for all taxa referred to in this study.

1.3 Geometric morphometrics

1.3.1 Landmarks and homology

In biology a landmark is a feature of a biological structure that can be readily identified by any trained person or trained software according to some well-established rules (see Bookstein, 1991, 1997; Webster & Sheets, 2010; Cooke & Terhune, 2015). The geometry of a biological structure like a bone can be captured using the Cartesian coordinates of landmarks (Bookstein, 1991, 1997; Jensen, 2003; Webster & Sheets, 2010). This is because as well as containing information about among-landmark distances (i.e. size), landmark coordinates contain information about the position of landmarks relative to one another (i.e. shape, as characterised by a configuration of landmarks for each object) (Webster & Sheets, 2010; Dujardin, 2011; Cooke & Terhune, 2015). Historically, only fixed landmarks which are based on biological homology were used (Bookstein, 1991; Cooke & Terhune, 2015). A homologous landmark position denotes biological correspondence of a landmark location across each object i.e. for 3D landmarks, each fixed landmark comprises a set of x, y, z coordinates in the same location across each object in the sample (Bookstein, 1991; Webster & Sheets, 2010).

However, descriptions of shape are considerably enhanced by incorporating semi-landmarks into a landmark configuration (Webster & Sheets, 2010). Semi-landmarks comprise several points placed along an outline such as a curve or border (i.e. a sliding semi-landmark), or a patch of landmarks (i.e. a surface sliding semi-landmark) comprising both fixed landmarks and curves to define complex shapes or regions (Bookstein, 1991; Webster & Sheets, 2010; Adams et al., 2013; Bardua et al., 2019a). As such, semi-landmarks are not biologically homologous but are instead mathematically homologous and their inclusion is now routine practice in landmark-based geometric morphometrics (Bookstein, 1991; Cooke & Terhune, 2015). In this study, Institute for Data Analysis and Visualization (IDAV) Landmark Editor (Wiley et al., 2005) was used to place landmarks on 3D digitised bones and these raw landmark data sets were exported for statistical analysis (Webster & Sheets, 2010; Cooke & Terhune, 2015).

The aim of using landmarks for bone shape comparisons was to emphasise anatomical features that vary across tubenosed birds and penguins to inform analyses of shape variation across these groups. Examples of important shape features described in this study using landmarks are mostly regions of bones where muscles attach (see Figure A.1 Landmark Scheme). As outlined above, landmark positions were selected on the requirement that 1) they were each a homologous position on digital replicas of bones that could be found across all specimens in the dataset, and 2) placement could be replicated accurately and consistently across all specimens in the sample (Webster & Sheets, 2010).

1.3.2 Procrustes superimposition

The analytical methods that are now commonly used for landmark-based analyses of biological shape were first popularised during the 1970s to early 1900s (e.g. Bookstein, 1977; Siegel & Benson, 1982; Rohlf & Slice, 1990; see also; Bookstein, 1991; Rohlf & Marcus, 1993) and have more-recently become widely accessible through dedicated packages for the R programming language and other freely-available software tools (e.g. Klingenberg, 2011; Adams & Otárola-Castillo, 2013). Procrustes superimposition is a statistical shape analysis method used to standardise the shapes of objects across a dataset, thereby allowing geometric comparisons to be made among objects in subsequent analyses (Bruner, 2006; Puckett et al., 2020; Newton et al., 2021). Procrustes superimposition involves optimally centering, scaling and rotating all landmark configurations by iteratively aligning them to an optimal mean reference configuration (i.e. an initial estimate of the average shape across the dataset) (Webster & Sheets, 2010; Breno et al., 2011). When three or more objects are involved, and alignment of these objects is to an estimated optimal mean reference shape, the superimposition method is referred to as Generalized Procrustes analysis (GPA) (Gower, 1975; Bruner, 2006; Webster & Sheets, 2010), as applied in my study.

The superimposition procedure removes all non-shape variation (i.e. differences in location, size and orientation) between configurations, resulting in shape variables (i.e. Procrustes-transformed landmark coordinates) which can then be used in analyses aimed at quantifying shape variation (Webster & Sheets, 2010; Breno et al., 2011). This is because any differences in corresponding landmark coordinates between configurations must then be due only to differences in shape (Cardini & Elton, 2007; Webster & Sheets, 2010; Puckett et al., 2020; Newton et al., 2021) i.e. pairwise distances calculated between corresponding landmarks (i.e. their Procrustes distance) provide a quantitative measure of shape disparity (Cardini & Elton, 2007; Webster & Sheets, 2010; Cooke & Terhune, 2015). Procrustes superimposition is used for shape research in a wide range of fields e.g. evolutionary biology (e.g. Randau et al., 2017; Tokita et al., 2017; Puckett et al., 2020), archeology (e.g. Drake et al., 2015; Yravedra et al., 2018; Dhoop et al., 2020), medicine (e.g. Cavaignac et al., 2017; Daboul et al., 2018), and geology (e.g. Vermeesch & Garzanti, 2015).

1.4 Statistical classification

The goal of this thesis was to predict the order or family for a group of seabird bones through comparisons of shape information from bones that were known to belong to particular families within Procellariiformes and within Sphenisciformes. This type of methodology falls within the field of statistical classification. Statistical classification is structured around training and test sets which are

used to train, evaluate and apply a classification (i.e. prediction) model. Splitting samples into training and test sets avoids the problem of overfitting whereby the model fit the data perfectly but fails to make reliable predictions on new data (Kuhn & Johnson, 2013). A training set is a subsample of data whose class membership is known and is used to train the classification on, hence allowing the model to recognise (i.e. predict) the class of new samples (Oliveri et al., 2018). A test set is essential in model validation as it comprises a set of new samples whose class membership is known but which have not been included in model building (Oliveri et al., 2018). It is the ability of the model, once completely trained, to make accurate class predictions on the test set that is evaluated and used to determine its reliability (Oliveri et al., 2018). The test set should contain a balanced representation of all classes in the total dataset (i.e. stratification of data by class) to account for differences in the number of data points and variation across each class (Oliveri et al., 2018).

1.4.1 *Partial least squares discriminant analysis*

Partial least squares discriminant analysis (PLS-DA) is a powerful machine learning method for classification that is widely used for modelling high dimensional data (Barker & Rayens, 2003; Lee et al., 2018; Oliveri et al., 2018), including when there are many more variables than samples in the dataset and variables are noisy or highly correlated (i.e. redundancy or multicollinearity among the predictor variables) (Tobias, 1995). Predictive modelling using the PLS-DA algorithm combines dimension reduction (i.e. constructing partial least squares; PLS components) and discriminant analysis (i.e. constructing a prediction model) (Lee et al., 2018). Unlike other discriminant algorithms such as linear discriminant analysis (LDA) (Fisher, 1936) PLS-DA does not assume the data come from a normal distribution, thereby making it a more flexible algorithm (Lee et al., 2018). However, the versatility of the PLS-DA algorithm means that several parameters must be optimised to construct a reliable prediction model (Lee et al., 2018). The flexibility of PLS-DA modelling has allowed it to be successfully applied across many different fields such as forensic science (e.g. Fernández de la Ossa et al., 2014; Ahlinder et al., 2015), banking (e.g. Serrano-Cinca & Gutiérrez-Nieto, 2013; Sghaier et al., 2018), medical diagnosis (e.g. Sattlecker et al., 2014; Liu et al., 2017) and food analysis (e.g. Bassbasi et al., 2014; Wu et al., 2017) (Lee et al., 2018). Here, PLS-DA modelling was used to develop a novel method for predicting taxonomic groups for seabirds based on 3D shape information from their bones.

At least eight practical steps are involved in the PLS-DA modelling procedure, each requiring a decision to be made (Lee et al., 2018). The first step is selection of modelling algorithm (Lee et al., 2018). The PLS1 algorithm models one class (i.e. one Y, response variable) at a time or more than one class independently (i.e. one versus all framework), while the PLS2 algorithm models more than one class at the same time (Lee et al., 2018). Data pre-processing may be performed (i.e. mean-centring and scaling) so that all variables have similar ranges and distributions (Lee et al., 2018). Dimension

reduction can be performed using either linear combination (e.g. PLS regression) (Wold et al., 2001; Lee et al., 2018) or variable selection to construct PLS components. Partial least squares regression results in a smaller number of latent (i.e. those most important in modelling the response variables; PLS components) and uncorrelated variables which reduces the risk of overfitting and makes the model more interpretable (Tobias, 1995; Wold et al., 2001; Lee et al., 2018).

In PLS regression the information in an X data matrix (i.e. predictor variables) is correlated to the information in a Y data matrix (i.e. response variables, which in this study is class membership) derived from a training dataset (Wold et al., 2001; Barker & Rayens, 2003; Wehrens & Mevik, 2007). The latent variables (i.e. PLS components) are found using the criterion of having maximum covariance between score values calculated for the X matrix and scores for the Y matrix (Höskuldsson, 1988; Tobias, 1995; Wold et al., 2001; Lee et al., 2018). This is in contrast to principal component regression where the scores in X are chosen to explain as much of the variation in Y as possible (Tobias, 1995; Lee et al., 2018). In PLS regression the Y scores can be predicted using the X scores and loadings (i.e. the X variation and the regression model) and from these we can use the Y loadings to get a prediction of Y (i.e. class membership) (Tobias, 1995; Wold et al., 2001; Lee et al., 2018). As the X scores can be correlated to the Y scores the relationship between pairs of corresponding X and Y scores is as strong as possible, giving us the ability to predict new samples (Tobias, 1995; Wold et al., 2001; Barker & Rayens, 2003; Lee et al., 2018).

Following dimension reduction, model validation including choice of method and strategy is an important step in generating reliable predictions (Lee et al., 2018). Resampling is used to estimate how well a model might perform when making predictions on data not used to train the model (Kuhn & Johnson, 2013). Generally, resampling procedures split the training data set into a subset of samples, some of which are fit to a model while others are used as a hold-out (i.e. validation) set to evaluate model performance (i.e. prediction ability) on new data (Kuhn & Johnson, 2013). A review of PLS-DA modelling found that internal methods for model validation (i.e. cross-validation) were preferred over external testing and methods such as bootstrapping (Lee et al., 2018). However, no single method has proven optimal across all modelling settings (i.e. the aim of the analysis, and the structure and properties of the dataset) (Lee et al., 2018). As such, this study compares the performance of two resampling methods (bootstrap for model 1 and repeated *k*-fold cross-validation for model 2; see Chapter 3.2.4) with the results from these analyses compared to determine the best method and model for the data.

Using the bootstrap method, a sample size is drawn with replacement from the original sample (i.e. representing one bootstrap sample/iteration) (Kuhn & Johnson, 2013). A sample size

equal to the original dataset is commonly used when estimating the performance of a machine learning model (i.e. PLS-DA model), which means that a sample may by chance be represented many times in the bootstrap sample or may not be selected at all (Kuhn & Johnson, 2013). The number of repetitions of the method must also be chosen i.e. a minimum of 20 or 30 repeats is required to allow meaningful statistics such as mean prediction accuracy to be calculated on the sample (Kuhn & Johnson, 2013). A model is fit to the bootstrap sample and used to predict those samples not selected in the sample (i.e. out-of-bag samples, OOB) (Kuhn & Johnson, 2013). Estimates of model performance (i.e. prediction accuracy) on the OOB sample are then used to evaluate prediction ability of the model (Kuhn & Johnson, 2013).

Repeated *k*-fold cross-validation is a variation on *k*-fold cross-validation in which a data set is randomly split into a number of groups equal to *k* that are approximately equal in size (Kuhn & Johnson, 2013; Brownlee, 2020). A number of models equal to *k* are trained and evaluated with each group (fold) given the opportunity to be the hold out (test) set, while the remaining folds are collectively used as the training set (Kuhn & Johnson, 2013; Brownlee, 2020). The average of the *k* performance estimates (i.e. for each fold) would be the cross-validation estimate of model performance (Kuhn & Johnson, 2013; Brownlee, 2020). Repeated *k*-fold cross-validation involves repeating this method many times to obtain a mean result of estimated model performance across all folds and from all runs (Kuhn & Johnson, 2013; Brownlee, 2020). For example, in a resampling method using 3-fold cross-validation with 10 repeats, 30 different models and 30 different held-out test sets would be fit and evaluated to estimate model performance (Brownlee, 2020). Repeated runs of the procedure should result in more reliable estimates of the average performance of the model when compared with the single run method (Brownlee, 2020). This is because in the latter the data are split into *k*-folds differently each time the method is run, which may result in different average estimates of model performance, thereby making final model selection difficult (Kuhn & Johnson, 2013; Brownlee, 2020). The best resampling method and model for the data would be determined by comparing the results from the repeated *k*-fold cross-validation model and the bootstrap model.

Model optimisation for order-level analyses (i.e. binary classification into either Procellariiformes or Sphenisciformes) is based on the area under the receiver operating characteristic (ROC) curve which encompasses the sensitivity and specificity of the classification model. Sensitivity is the true positive rate which is defined as the percentage of samples belonging to the 'positive' (first) class that are correctly predicted to that class. Specificity is the true negative rate and is defined as the percentage of samples belonging to the 'negative' (second) class that are correctly rejected by the model (Kuhn, 2009, 2015; Oliveri et al., 2018). The ROC curve shows the trade-off between these two measures, at different probability thresholds (Kuhn, 2009, 2015). The higher the area under the ROC

curve, the more predictive power the model has for the data i.e. the better the model is at making correct predictions (Kuhn, 2009).

1.5 Humeri and femora

The humerus (i.e. the upper-most arm bone) and femur (i.e. the thigh bone) were the elements chosen for shape comparisons and class predictions in this study. Humeri and femora are two of the most robust bones in the body of a bird and are therefore among the more commonly recovered bird bones from fossil or subfossil deposits (e.g. Livingston, 1989; Chiappe & Witmer, 2002; Worthy et al., 2007; Tennyson & Mannering, 2018). The humerus is a diagnostic bone as it has many discrete characters (i.e. phylogenetically informative features) which vary among species, and is often important in traditional systematic methods for identifying and classifying taxa (e.g. Ksepka et al., 2012; Degrange et al., 2018; Thomas et al., 2020b). For this project we expect the humerus to work well in making predictions of taxonomic identity of seabirds using classification analyses based on the 3D shape of this bone.

Conversely, the femur is not a typically informative bone within Procellariiformes (e.g. Mayr & Smith, 2012; Tennyson & Mannering, 2018) or Sphenisciformes (e.g. Ksepka et al., 2012; Ksepka & Thomas, 2012; Thomas et al., 2020b). Unlike for the humerus, trait matrices do not contain extensive morphological character data for the femur and this bone has not proven especially useful for distinguishing between closely-related and similarly-sized species in the same family (e.g. Mayr & Smith, 2012; Tennyson & Mannering, 2018; Thomas et al., 2020b). However, my study investigated the potential for 3D geometric morphometric descriptions of the femur to be taxonomically informative, for which a thorough exploration in Procellariiformes and Sphenisciformes has not previously been reported. In the same way as the humerus, it was thought that 3D shape information from the femur may have the potential for distinguishing taxonomic groups as part of a taxonomic classification method. The major implication of this work would be that, through the use of 3D geometric morphometrics, typically uninformative bones such as the femur and others which are not traditionally used for classifying taxa might then allow for the identification of bird remains if only incomplete skeletons (i.e. isolated, fragmentary or uninformative bones) containing no useful molecular sequence data are available.

1.6 Aims

The aim of this thesis was to develop a taxonomic classification method for individual bones using advanced 3D shape analyses i.e. using both well-established landmark-based techniques and novel

landmark-free 3D geometric morphometric methods. I aimed to test the hypothesis that 3D shape analyses of digitised bones can be used to confidently predict taxonomic groups for seabird bones using partial least squares discriminant analysis.

The key objective was to make family-level predictions of bird bone taxonomy given that family-level analyses are useful for both modern and fossil bones. My objectives were to discover if: 1) femora or humeri from species of tubenosed bird can be distinguished from femora or humeri of penguins using 3D geometric morphometrics; and if 2) femora or humeri from species of tubenosed bird in one family can be distinguished from femora or humeri of tubenosed birds in another family using 3D geometric morphometrics.

2 Materials and 3D digitisation methods

2.1 Specimen access

Procellariiformes is one of the best represented taxonomic groups in New Zealand museum collections with extensive material housed at Auckland War Memorial Museum (Auckland), Te Papa Tongarewa Museum of New Zealand (Wellington), and Canterbury Museum (Christchurch) (Gill, 2006). This meant that specimens belonging to species within Procellariiformes were easily accessible for 3D scanning and were in sufficient number for building the statistically-robust datasets of 3D digitised bones needed for this study. Anatomical and orientation terminology follows Baumel and Witmer (1993).

2.2 Library of 3D digitised bones

A library of digital femora and humeri was generated from the bird skeleton collections of the Auckland War Memorial Museum (AM), Canterbury Museum (CM), and the Museum of New Zealand Te Papa Tongarewa (NMNZ) using 3D surface scanning and microCT methods (see 2.3 3D digitisation). The goal was to produce 3D digital replicas from up to ten individuals from at least three species for three families within Procellariiformes (i.e. the tubenosed birds - Diomedeidae, Oceanitidae and Procellariidae) and in Sphenisciformes (i.e. penguins – Spheniscidae). Note that due to a lack of specimens in New Zealand institutions we were not able to include Hydrobatidae in this study. Previous studies have found that a minimum sample size of between 25 to 40 individuals per group is required to achieve accurate estimates of mean shape when comparing closely-related taxa (Cardini & Elton, 2007; Cardini et al., 2015; Cardini et al., 2021). However, this is not always possible due to time and funding limits, rarity of taxa, availability of specimens in museum collections, and it is relatively common in geometric morphometric studies for at least some of the groups under comparison to be represented by fewer than 10 individuals (Cardini & Elton, 2007; Cardini et al., 2015) (e.g. Bruner, 2004; Stayton & Ruta, 2006; Gunnell et al., 2018; Bardua et al., 2019b; Marcy et al., 2020).

3D digital replicas were generated of 312 left femora from 291 extant species in Procellariiformes and 21 extant species in Sphenisciformes, and 274 left humeri were generated from 249 extant species in Procellariiformes and 25 extant species in Sphenisciformes. Thus, a total dataset size of 585 bones was achieved for this thesis (Table 2.1; see Table B.1 Complete specimen list). Left femora and left humeri were selected when available. When only right elements were available these were 3D scanned and mirrored in Blender 2.8.1 (Blender Online Community, 2019) or 3D Slicer version 4.11.20200930 (http://www.slicer.org; Fedorov et al., 2012). Only adult bones were selected for the datasets.

The full datasets of digital bone replicas (i.e. 312 femora and 274 humeri) were used for Generalized Procrustes Surface Analysis (GPSA), separately (see Chapter 4 GPSA). Digital femora from 188 individuals were used for landmark analysis in Chapter 3: Femur landmarks. This was the dataset size achievable within the time constraints of this thesis given that landmark digitisation is both time- and labour-intensive.

Table 2.1. Number of specimens in femur and humerus datasets. See Appendix B Table B.1 for full details.

	Dataset	
Family	**Femur**	**Humerus**
Diomedeidae	82	70
Oceanitidae	19	20
Procellariidae	190	159
Spheniscidae	21	25
Total dataset size	**312**	**274**

2.3   3D digitisation

An increasing availability of 3D imaging equipment including computed tomography (CT) and surface scanners has enabled researchers to generate large datasets of high resolution 3D digital replicas of specimens from museums and elsewhere (e.g. Weber et al., 2001; Tocheri et al., 2005; Tocheri, 2009; Gould, 2014; Bright et al., 2016; Hipsley et al., 2020; Puckett et al., 2020; Thomas et al., 2020a; Newton et al., 2021). Direct shape comparisons may then be performed through the use of freely available software tools (e.g. Geomorph, (Adams & Otárola-Castillo, 2013); Institute for Data Analysis and Visualization (IDAV) Landmark Editor, (Wiley et al., 2005).

2.3.1   Structured light scanning

Structured light scanning (i.e. surface scanning) was used for high throughput of medium to large-sized bones (i.e. ≥2.5 cm long). This type of scanning involves the projection of light and shade patterns onto an object at the same time that images of the object are captured (Geng, 2011; Creaform Inc., 2015, 2020). Pattern variations and the geometry of the data are detected by the scanner and used to reconstruct the features of an object in three dimensions (Geng, 2011; Creaform Inc., 2015, 2020). Multiple images must be taken from different positions in order to collect enough surface data to produce a complete 3D digital replica (also termed a 3D mesh) (Geng, 2011; Creaform Inc., 2015, 2020).

At the beginning of this study an SLS-2 structured light scanner (HP Inc., CA, USA, formerly DAVID Vision Systems GmbH, Koblenz, Germany) was used for digitising bones, with each bone taking

approximately 15 minutes to scan. Using DAVID 3 software version 3.10.4.4657 (HP Inc.) surface scans were aligned and fused to produce 3D digital replicas which preserve key anatomical features (Niven et al., 2009; Thomas et al., 2016) and could be subsequently used for landmark placement in 3D shape analyses (Webster & Sheets, 2010; Cooke & Terhune, 2015).

This project used a similar scanning method to the one described by Thomas et al. (2016). The 3D scanning system comprised two cameras (DAVID-CAM-3.1-M; DAVID Vision Systems) and a projector (Acer Incorporated, New Taipei City, Taiwan) mounted on a support bar attached to either an adjustable tripod, or a moveable arm clamped to the edge of a workbench, as well as an automated turntable. Both setup and scanning were performed in a dimly-lit room to enable the camera to more easily detect the interface between the black and the white stripes projected over the object. Cables connected the cameras, projector and turntable to a computer running DAVID 3. One camera was positioned to the left, and the other to the right of the projector on the support bar. Both cameras were rotated between 19 and 21°, clockwise for the left camera and anti-clockwise for the right camera. The bone to be scanned was placed in the centre of the turntable. The position and height of the tripod or arm in relation to the bone, and also the distance between the camera and projector, were adjusted to have the bone appear centred in camera view (using the live camera view on the monitor for guidance). The focus of both the projector and cameras, as well as the exposure of the cameras, were adjusted to get the clearest image of the bone (again, using the live camera view from the monitor for guidance). The specimen was removed from the turntable in order to calibrate the scanner.

Prior to 3D imaging, calibration of the cameras and projector is critical in establishing the measurement accuracy of the scanning system (Geng, 2011; Thomas et al., 2016). The cameras and projector both required geometric calibration which was achieved using images on a pair of checkerboard-patterned calibration panels (Geng, 2011). As the projector was an active light source, the intensity of its illumination also required calibration (Geng, 2011). To calibrate the scanner the turntable was moved aside and the calibration panels setup in front of the scanner with a chosen calibration pattern size based on the size of the bone to be scanned. The support bar was then pivoted upwards for the cameras and projector to be directed straight at the chosen calibration pattern on the panels. If the projector was not level with the calibration pattern then the height of the panels was adjusted until this was so. Readjustment of all parts may be needed for a successful calibration.

Having successfully calibrated the scanner the specimen was then placed back onto the turntable in centred camera view and 3D scanned in four orientations: cranial, caudal, anterior and posterior for humeri, and cranial, caudal, lateral and medial for femora. Firstly, eight scans of the

cranial surface of the bone were taken, with each scan following a 45° automated turntable rotation of the specimen. The bone was then rotated for eight scans to be taken of the caudal surface. The anterior and posterior (or lateral and medial) surfaces were also scanned in this way, with dark fabric material or a dark object such as a camera lens cap used to position and rest the bone against. After evaluating how well scanning of each of the four surfaces had captured the entire specimen, additional scans were obtained if needed to ensure that complete coverage of the bone was achieved. Thus, at least 32 surface scans were used to produce the final 3D digital replica model. DAVID 3 software was used to align and fuse the 3D scans into 3D models. The raw surface scans were loaded into DAVID 3 and any background vertices were removed. A set of eight scans from the same surface were globally aligned to form four groups of aligned scans. Any scans that overlapped with other scans and therefore did not provide new information to the model were not used. The four groups were then pairwise-aligned and grouped to one another to form a composite model. All scans were ungrouped and global alignment was performed to ensure optimal alignment of all contributing scans. The final model was fused at either 500, 700, or 1000 mm resolution; whichever resulted in a model with 0.2 mm spacing or less between vertices**.** This would allow for resolution of the smallest required observable feature of the bones used in this study i.e. nutrient foramina. In R Studio version 1.2.1335 (R Team., 2019) using the function 'vcgQEdecim' from the Rvcg 0.19.1 package (Schlager, 2017) mesh densities of the models were decimated to approximately 10% of the original mesh density to allow for easier handling in IDAV Landmark (Wiley et al., 2005; Thomas et al., 2020a).

2.3.2   HandySCAN laser scanner

A HandySCAN BLACK 3D laser scanner (Creaform Inc., Quebec, Canada) using VXelements software version 7.0 (Creaform Inc.) was acquired for our research group at Massey during the thesis year of my project and became the main instrument for data collection (see Figure C.1). As well as being effective in scanning a range of different sized bones, from relatively small specimens (approximately 2 cm long) to very large species (>50 cm long), this scanning system allowed for faster and easier generation of 3D scan data and production of high quality 3D models with exceptional accuracy and resolution, making data collection much more efficient.

The HandySCAN BLACK 3D scanner is a handheld surface scanning device with two inbuilt lasers aimed by the user at the object to be scanned. The scanner emits a grid of laser lines onto the object which allows a camera in the scanner to record the intersection of the beam and the object (Creaform Inc., 2015, 2020). Positioning targets were placed in a random scatter approximately 3 cm apart on or around the object. The position of the scanner in 3D space relative to the object is informed by the targets (Creaform Inc., 2015, 2020). A cable connected the scanner to a computer running VXelements. This software was used to generate 3D surface scans as well as produce and edit 3D

digital models from the scans. Initial setup involved a short scanning procedure to calibrate the scanner. Guided by on-screen prompts the handheld device was manually aligned with a 15-step scanning sequence using the calibration plates. With the bone placed on the board the scanner was then configured to the lighting conditions of the room with 'auto adjust' selected to optimise the exposure.

The targets were scanned in isolation to the bone and the placement of these targets was recorded in the scanning software. A clipping plane was created by selecting three of the outermost positioning targets and then adjusting the height of the plane to exclude anything below this point from being scanned. This meant that only data from the bone itself would be detected by the scanner and not any part of the environment surrounding or beneath the bone. A resolution of 0.5 mm was applied for collecting the initial surface scan data of medium to large-sized bones which allowed me to collect sufficiently well-resolved surface scans while not overusing computer memory during the scanning process (specifically random access memory; RAM). Scans would later be aligned into models at a resolution of 0.2 mm thereby producing a final higher resolution model. Smaller bones were scanned at an initial resolution of 0.2 mm. This was because a higher resolution (i.e. a denser cloud of scan points representing the object) is required in order to capture detailed scans of very small objects (RangeVision, 2021).

With the positioning targets and clipping plane visible two scans were generated for each bone, one of the cranial surface and one of the caudal surface, which when merged and aligned together provided sufficient coverage to produce a complete digital replica of the bone. This was done holding the scanner approximately 30 cm away from the specimen with the lasers aimed at and moved across the bone surface until coverage of the entire detectable surface had been achieved. The scan was then saved and the bone rotated with the process repeated for the opposite surface. Vertices captured from the environment and other noise was removed from each scan and the two scans were merged and aligned into a single object representing the entire bone. A resolution of 0.2 mm was applied to the aligned scan which was then finalised and exported as a mesh to the 'VXmodel' module for editing. The mesh was cleaned and any holes where data were not collected during scanning were filled to produce a final watertight model. Finally, I aligned the model to its origin which would later facilitate manoeuvrability of the model and accuracy of landmark placement in IDAV Landmark Editor software. The final mesh was then exported as both an .obj and .ply file.

2.3.3   MicroCT scanning

MicroCT analyses allowed me to digitise bones that were too small for surface scanning equipment. I was then able to generate a more inclusive dataset for order Procellariiformes. In particular, microCT

allowed me to include more specimens from Oceanitidae which is comprised of species that tend to have very small femora (≤2.5 cm long i.e. *Fregetta maoriana*, *Oceanites oceanicus*), as well as femora from other small species within Procellariidae (i.e. *Pachyptila* spp., *Pterodroma cookii*). Specimens were borrowed from the collections at Auckland War Memorial Museum and transported to the microCT suite in the Auckland Bioengineering Institute at the University of Auckland for imaging. Imaging was performed on a Skyscan 1172 microCT instrument (Bruker Optiks., Ettlingen, Germany) that was operated by Dane Gerneke, University of Auckland.

The method outlined here for grouping and imaging multiple small bones was adapted from Hipsley et al. (2020). A single bone (maximum 25 mm length) was placed inside a size 00 gelatin capsule along with a specimen label for tracking purposes and a small piece of acid-free archival tissue to prevent any movement of the bone during imaging (see Figure D.1). Hipsley et al. (2020) found that fewer specimens per capsule (i.e. 1 or 2 maximum) resulted in less movement during the scanning process. This was an important consideration as even small movements can introduce artifacts such as shadows or streaking which may affect the quality of the image reconstruction (Hipsley et al., 2020). Labels were written on acid-free archival tissue to allow identification of each specimen and therefore avoid mistaking bones for one another when returning them to the collections. Capsules were stored in labelled Falcon tubes (Figure D.1a). Each capsule was sealed with clear tape and labelled with its storage tube number, one or two-letters to identify the row it was assigned to (i.e. P, Q, R) and a number to represent its position within the row (1-5) using a permanent marker (Figure D.1a-c). Capsules were attached to a plastic straw using a small amount of screen-printing glue (Figure D.1a-c). This was done in three rows of five capsules maximum each, with each row of capsules positioned at the same level around the circumference of the straw (Figure D.1b-c). A mylar marker was placed above capsule one. This produced a shadow on the x-ray images and working anti-clockwise, facilitated the tracking of bones in each row.

This specimen-holder design ensured that at least ten bones would fit within the limits of the imaging window for a single scanning session (see Figure D.1e). For ease of specimen tracking, one capsule was filled with an especially distinctive bone or a different type of bone (e.g. a coracoid) in a different position across each row. A clear tube was then placed over the straw and capsules (Figure D.1d) and the entire tube was placed onto the imaging stage inside the instrument. The imaging stage helped to achieve precise positioning of the object in the centre of the scanning field, thereby improving the quality of scans and achieving optimal speed of scanning (Bruker, 2021). Setup and operation of the Skyscan microCT scanner was performed by Dane Gerneke, University of Auckland. The detector was calibrated and the imaging settings adjusted in order to optimise the parameters specific to the object size and required results. Here, bones were scanned at a resolution of 27 μm,

with a voltage 54 kV, amperage 185 μA, and power 10 W. These settings reduced the amount of time required for imaging, therefore maximising the total number of specimens imaged without compromising on image quality. The number of steps per degree was set to 0.45. With an image taken at each step of the 360° stage rotation, this resulted in a total of 162 stacked x-ray images (i.e. raw data). Bones were imaged in four parts with ten bones requiring 2.5 to 3 hours.

Following the workflow of Buser et al. (2020) the software NRecon (Skyscan NV., 2011) was used to preview and reconstruct the 2D cross-section images obtained from x-ray computed tomography scans, with the contrast optimised in order to remove any artifacts (Skyscan NV., 2011). The final image stack was exported in tagged image file (TIFF) .tif format and loaded into DataViewer software (Skyscan NV., 2011) to visualise the image quality of the data. Here, slices were subset to produce new files containing data for only a single bone per image stack for ease of processing in the following steps. The subset images were imported into Fiji (Schindelin et al., 2012), an expansion of ImageJ (version 2.0.0; Schneider et al., 2012; Rueden et al., 2017), which was used to create an image stack for each bone separately with the option 'use virtual stack' selected in order to reduce the time required for reading-in the image sequence. Voxel size was specified as 0.027 mm pixel width and the image stack was compressed to reduce file size before being exported in the nearly raw raster data (NRRD) .nrrd file format. File size reduction was necessary so as to overcome the high demand on computation and available computer memory associated with CT analysis in the following steps of the workflow.

Finally, to create a 3D object from the image stack the NRRD volume was loaded into the image analysis and visualisation software platform 3D Slicer version 4.11.20200930 (http://www.slicer.org; Fedorov et al., 2012). The first step was to set the image spacing of the volume to 0.027 mm resolution in the 'Volumes' module. In the 'Segment Editor' module a blank volume was created after adding a segment and filling it based on a threshold range manually adjusted to show the least amount of colour. The CT imaging process was able to capture the trabecular (i.e. lattice-like) structure of the inner bone which was found to be problematic for landmark placement on the 3D models in IDAV Landmark Editor software. Therefore, the cavity of the bone was also filled using various tools in the 'effects' submenu. The volume was converted to a 3D model in the 'Segmentations' module and saved and exported as an .obj file.

3 Femur landmarks

3.1 Introduction

The objective of this thesis was to determine if 3D shape analyses of digitised bones can be used to confidently predict taxonomic groups for seabirds using partial least squares discriminant analysis. Here the focus was to investigate if the femur, a typically uninformative bone for taxonomic identification within seabirds (e.g. Tennyson & Mannering, 2018; Watanabe et al., 2018; Thomas et al., 2020b), may be informative in 3D bone shape analyses i.e. using landmark-based geometric morphometrics. The specific objective of this study was to test the hypothesis that landmark-based analyses can predict the taxonomic family to which a bird femur belongs. This is because family-level analyses are useful for both modern and fossil bones (Eda et al., 2016b; Zeder & Spitzer, 2016; Seersholm et al., 2018; Horn et al., 2019). Humeri were analysed in a separate study (see Chapter 4 GPSA). The taxonomic classification method developed here would be considered successful if the classification rate was substantially higher than the null classification rate (Oliveri et al., 2018).

In 3D geometric morphometric methods a fixed landmark represents a homologous point for every bone in the sample (Webster & Sheets, 2010). A curve is comprised of several points (i.e. a sliding semi-landmark) placed along an outline or border with a fixed landmark defining the beginning and end points of the curve (Webster & Sheets, 2010). A patch of landmarks comprises both fixed landmarks and curves to capture complex shapes or entire regions of the bone (Bookstein, 1991; Webster & Sheets, 2010; Adams et al., 2013; Bardua et al., 2019a). Landmarks were used to summarise the shape of each digitised bone for subsequent geometric morphometric analyses (Webster & Sheets, 2010; Cooke & Terhune, 2015). Landmark-based geometric morphometrics were combined with statistical classification (i.e. partial least squares discriminant analysis) to determine how well the taxonomic identification could be predicted. As described in Chapter 1, seabirds were the focal group for this study due to their incredible abundance and fossil record throughout New Zealand.

3.2 Materials and Methods

3.2.1 Materials

One hundred and eighty-eight digital left femora from extant species in Diomedeidae (n = 48), Oceanitidae (n = 19), Procellariidae (n = 100), and Spheniscidae (n = 21) were used for landmark analysis (see Chapter 2.2 Library of 3D digitised bones). Ten individuals from three species within both Diomedeidae (*Diomedea antipodensis, Phoebetria palpebrata, Thalassarche chrysostoma*) and Procellariidae (*Ardenna grisea, Pachyptila turtur, Pterodroma inexpectata*), and ten individuals from one species within Oceanitidae (*Pelagodroma marina*) formed the core of this library (see Table B.1 in

Appendix B). The library was divided into randomly-assigned training and test sets for statistical classification analyses. Approximately one quarter of the library was assigned to the test set in any one analysis.

3.2.2 Landmarks

Landmarks were manually placed by myself on the digital femora using IDAV Landmark Editor 3.0 (Wiley et al., 2005). A total of 188 digital replicas were generated (i.e. one copy of 188 femora). I developed the femur landmark scheme used in this study which comprised 72 landmarks including seven fixed landmarks, four curves (sliding semi-landmarks), and one patch (surface sliding semi-landmark) (see Table A.1 and Figure A.1 in Appendix A). Fixed landmarks delimited the extremities of the distal femur (s0-s7), while curves captured the position and projection of the trochanteric crest (c0), as well as mid-shaft width (c1-c2) and shaft length (c3). A single patch encompassed the entire region of the femoral head (p0) (see A.1 Landmark scheme in Appendix A).

The landmark scheme was applied to an arbitrarily chosen digital replica which was then used as the 'atlas' or reference when placing landmarks on all remaining replicas in the dataset. Landmarks were then placed on the remaining digitised femora. Note that landmarks were placed in the same sequence (i.e. starting with p0) for all digital bones. Bones were not landmarked in taxonomic sequence to avoid bias in landmark placement that may arise from consecutive landmarking of digital bones representing the same genus or species.

3.2.3 Generalised Procrustes analysis and principal component analysis

In Landmark Editor (Wiley et al., 2005) configurations of landmarks for each specimen were exported as .pts files and read into R studio version 1.2.1335 (R Team., 2019) using the 'read.pts' function in the Morpho 2.8 package (Schlager, 2017). Using the 'gpagen' function from the Geomorph 3.3.1 package (Adams & Otárola-Castillo, 2013) the landmark sets from each bone were Procrustes-transformed before being further analysed with principal component analysis (PCA) (Figure 3.2; see Appendix E.1 R code for landmark-based analyses) using the 'gm.prcomp' function from the same package.

Principal component analysis (PCA) was used as a visualisation tool to explore and understand the information and structure in the femur landmark data. This technique reduced the dimensionality of the data down to the most important sources of variation, thereby revealing the groupings that the classification analysis would be based on (Figure 3.2) i.e. by revealing groupings of specimens based on similar shape, and detecting any outliers including landmark digitisation errors (Webster & Sheets, 2010; Cooke & Terhune, 2015). Loadings derived from the PCA illustrated where the variation in the landmarks was loaded by showing the degree to which each landmark varied about mean x, y, z

coordinates across all configurations in the sample, and therefore which landmarks contributed the most to the variance explained by a given principal component (Figure 3.3a-d).

3.2.4   Classification analyses on 3D landmarks in training set

Membership of each bone to an order or family was predicted using partial least squares discriminant analysis (PLS-DA) classification performed in RStudio using functions from several packages including caret 6.0-86 (Kuhn, 2008; Kuhn et al., 2020), pls 2.7-3 (Mevik et al., 2020) and abind 1.4-5 (Plate et al., 2016).

Training and test sets

The 'createDataPartition' function from the caret package (Kuhn, 2008; Kuhn et al., 2020) created a balanced split of the data with approximately 75% of the femur landmark sets (142 out of 188 total) assigned to the training set and the remaining approximately 25% assigned to the test set. This was the default ratio for partitioning data in caret (Kuhn, 2008; Kuhn et al., 2020). Assignment into training and test sets was stratified by class (i.e. proportional to the number of landmark sets in each order or family), and random within each stratum. Stratification was important for ensuring a balanced representation of all classes in the training and test sets given that some classes (i.e. Procellariidae) contained significantly more landmark sets and encompassed more variation than others (see Figure 3.2).

Resampling choice and model evaluation

As outlined in Chapter 1, two different PLS-DA models that each use different resampling methods were built and evaluated at both order- and family-level using the 'train' function from the caret package (Kuhn, 2008; Kuhn et al., 2020). The default resampling method for the 'train' function in the caret package is bootstrapping, as used in model 1 below. Repeated *k*-fold cross-validation was used for resampling in model 2 below. The model with the highest prediction accuracy for family-level analyses, or area under the receiver operating characteristic (ROC) curve for order-level analyses, as well as the lowest number of optimal PLS components, would show the best fit to the data and would be the model chosen for the classification analyses.

Model training and optimisation

The bootstrapping and repeated *k*-fold cross-validation PLS models were trained on the approximately 75% of samples selected for the training dataset. The first step in training these models was to determine the number of PLS components needed to optimise the performance of each model (i.e. an initial 'tuning' step) (Kuhn & Johnson, 2013). Component number was measured against classification accuracy to determine how many should be retained in the optimal model (Kuhn &

Johnson, 2013). Centering and scaling was specified for the predictor variables for all samples using the 'preProcess' function to ensure that the ranges and distributions of all variables were comparable (Lee et al., 2018). The 'tuneLength' function was set to 20 to expand on the default setting in caret in which 15 candidate values are tuned across to find the optimal number of PLS components. This was because initial iterations in model training found 15 components to be optimal and therefore extending the range of candidate values to 20 allowed for the possibility of a higher optimal value to be found for this parameter. The type of resampling used (i.e. bootstrapping and repeated k-fold cross-validation) to tune the parameter values (i.e. the number of PLS components) was modified using the 'trainControl' function from caret, with the candidate values (i.e. 1 to 20) adjusted iteratively until the optimal number of components and overall accuracy (i.e. the percentage of correctly classified samples across the entire sample) was reached. As outlined above, the default method 'boot' (i.e. simple bootstrap) was used in model 1 with 25, 50, 100 and 200 bootstrap samples computed iteratively. In model 2 'repeatedcv' (i.e. repeated k-fold cross-validation) with 10 repeats was specified in which 10 separate 3, 5 and 10-fold cross validations were iteratively computed as the resampling scheme.

The 'summaryFunction' from caret was used to evaluate the effect of the tuning parameters on the performance of bootstrap model 1 and repeatedcv model 2 at both order- and family-level. The average resampled estimates of performance (i.e. estimated values of either accuracy or ROC, sensitivity and specificity associated with each parameter value) were calculated across hold-out predictions (i.e. a subset of samples predicted by the model which are not used in model training) (Kuhn, 2009, 2015). As outlined in chapter 1, in binary classification (i.e. order-level analyses) the ROC curve is computed which shows how well the model performs in discriminating one class from the other, based on the predicted class probabilities. The option 'classProbs' = TRUE was used to compute class probabilities and from these the ROC curve, based on an optimised probability threshold automatically applied for predicting new samples using caret (Kuhn, 2009). The function 'twoClassSummary' was specified with "metric = ROC" to compute and optimise performance measures specific to two-class problems as shown in the resultant confusion matrix. For family-level analyses (i.e. classification into one of the four possible classes) the function 'defaultSummary' was specified as this is required for computing measures in multi-class classification problems (i.e. a confusion matrix showing the outcomes of the discriminant classification will include both overall prediction accuracy and how this is partitioned across the classes).

Finally, for both order- and family-level analyses the optimal parameter set was determined by selecting the tuning parameter associated with the best results. This was based on ROC (order-level) or accuracy (family-level), using the largest performance value as the optimality criterion. The

best model performance was found using resampling schemes consisting of 25 bootstrap samples for model 1, and 10 separate 3-fold cross-validations for model 2. For order-level analyses one PLS component was found to be optimal in both models 1 and 2. In family-level analyses six PLS components was the optimal number to be included in both models 1 and 2 (Appendix F Table F.1; F.2). Importantly, both model 1 and model 2 were found to be equally optimal for both order- and family-level analyses, and thus both models 1 and 2 were used in subsequent analyses (see Model selection below).

Using the final specifications two PLS models (i.e. model 1 using 25 bootstrap samples and model 2 using 10 separate 3-fold cross-validations) were fit to all of the training data separately for both order-level and family-level analyses (Appendix F Table F.1; F.2). These models were then applied to the test set using the function 'predict' from the stats package version 4.0.2 (R Core Team., 2020). Class probabilities were computed from the model to make class predictions (i.e. order or family) for new samples. Model predictions were transformed to "probability-like" values (i.e. between 0 and 1, summing to 1) using the argument 'probMethod' with the default method 'softmax' in caret (Kuhn, 2009). The decision rule determining the predicted class was the one with the largest class probability (Kuhn, 2009; Kuhn et al., 2020).

The confusion matrix and associated statistics including overall prediction accuracy (the percentage of correctly predicted samples across the entire test sample), and balanced accuracy (the average of the sensitivity and specificity values with 1 = best and 0 = worst) across each class for each model fit were computed using the function 'confusionMatrix' from caret. A confusion matrix is the output of classification results summarising the performance of the PLS-DA model (i.e. percentage of correctly classified samples; which class samples were classified to) (Kuhn, 2009). By default the caret package uses the first level of the outcome factor (i.e. class) when computing the confusion matrix in binary classification problems (i.e. 'positive' class = Procellariiformes) (Kuhn, 2009). Therefore at order-level a second confusion matrix was computed with the 'positive' argument set to 'Sphenisciformes' to obtain performance measures across both classes. Results from the confusion matrix outputs were used to compare the two model fits for both order-level and family-level analyses (Table 3.1; 3.2).

Model selection

For both order- and family-level analyses the best-performing model was selected based on the criteria of highest overall accuracy and lowest optimal number of PLS components. For order-level analyses both model 1 (bootstrapping, ncomp = 1) and model 2 (repeated 3-fold cross-validation, ncomp = 1) had a 100% overall classification accuracy, 100% sensitivity, 100% specificity and 100%

balanced accuracy with either Procellariiformes or Sphenisciformes set as the 'positive' class (Table 3.1). Both models 1 and 2 were determined as the best-performing and final model as they had an equal overall accuracy, number of optimal PLS components, and sensitivity, specificity and balanced accuracy values. For family-level analyses model 1 (bootstrapping, six PLS components) and model 2 (repeated 3-fold cross-validation, six PLS components) produced identical results (overall 93.5% classification accuracy) (Table 3.2). Both models 1 and 2 were determined as the best-performing and final model as they had an equal overall accuracy and number of optimal PLS components.

Using models 1 and 2 the classification rate (i.e. prediction accuracy) for each class was evaluated on the test set at both order- and family-level. This was computed as the balanced accuracy i.e. the number of samples correctly classified (or predicted) as a percentage, out of the total number of samples belonging to the class (Oliveri et al., 2018) and used to evaluate the hypotheses for this study. According to Oliveri et al. (2018) a classification result is deemed acceptable if the value of the rate is substantially higher than the null classification rate which can be defined as the probability percentage of correct assignments by chance, calculated by dividing 100 by the number of classes. In this case the null classification rate would be 25%.

3.3   Results

3.3.1   Principal component analysis

The first 25 principal components (PCs) accounted for 95% of the variation in landmark configurations (Figure 3.2). Principal component one (PC1) explained 31.6% of the variation in femoral shape as defined by landmark positions, and PC2 explained 19.2% of the variation (Figure 3.1). Principal component three, four and five accounted for 13.7%, 7.5%, 5.9% respectively. The most distinct separation at order-level (i.e. between tubenosed birds and penguins) was found along PC1 and PC2 (Figure 3.2a). The most distinct separation at family-level (i.e. between Procellariidae, Diomedeidae, Oceanitidae, Spheniscidae) was found along PC1 and PC4, and when plotted against one another allowed visualisation of the area of morphospace occupied by each order and family (Figure 3.2b). Scores representing femur shape in tubenosed birds and penguins clustered at the negative and positive ends of PC1 respectively, indicating a distinct separation between these groups (Figure 3.2a). Separation between tubenosed bird families was best along PC1 and PC4 with families forming clusters however, Diomedeidae showed overlap with both Oceanitidae and (in particular) Procellariidae. Clear separation of some tubenosed bird genera was found along PC1 and PC4 e.g. *Ardenna, Diomedea*, *Garrodia, Pelagodroma*, *Pterodroma* formed distinct clusters (within their respective families) (Appendix G Figure G.1).
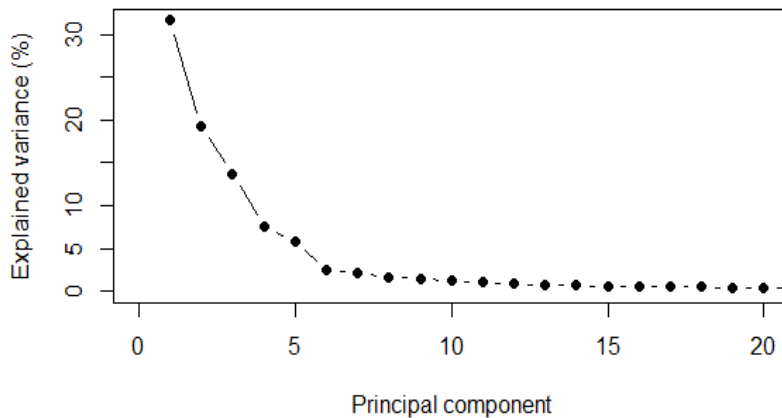
Figure 3.1. Scree plot showing the percentage of variance explained by each of the first 20 principal components from PCA on femoral shape data.

a)   b)
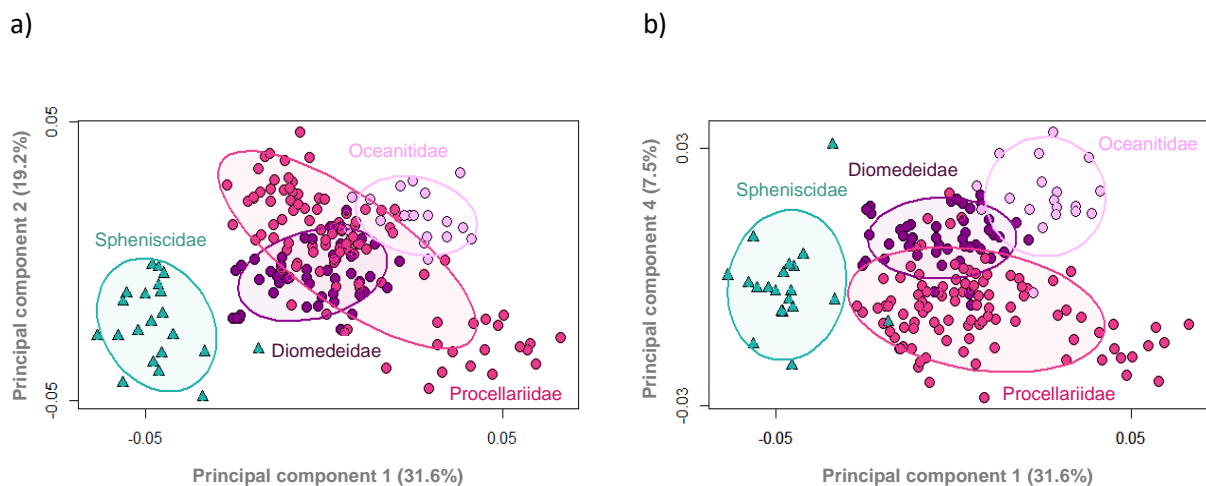
Figure 3.2. Morphospace reflecting disparity in the shape of the femur from tubenosed birds (Diomedeidae, Oceanitidae, Procellariidae) and penguins (Spheniscidae) as shown by scores from principal component analysis of Procrustes-transformed landmark data. a) PC1 vs PC2 and b) PC1 vs PC4. 95% confidence ellipses (a = 0.05) used here and throughout.

The curve tracing the trochanteric crest (c0) was a major source of variation for PC1, e.g. positioned more cranially in Procellariiformes, and more laterally in Sphenisciformes (Figure 3.3a, see Appendix A Figure A.1). The two curves defining the width of the shaft at its mid-point (c2-c3) depicted a thicker shaft in Sphenisciformes compared with Procellariiformes. All fixed landmarks delimiting the extremities of the distal femur but especially s3, s4, s5 and s7 were highly variable along PC1. Projection of the trochanteric crest was a major source of variation for PC2, e.g. in Procellariiformes

the lower two-thirds of the crest projected further craniolaterally than in Sphenisciformes (Figure 3.3b, see Appendix A Figure A.1). The distal end of the trochanteric crest was positioned more distally in Procellariiformes compared with Sphenisciformes. The fixed landmarks defining the most caudally-projecting points on the lateral condyle (s0), and lateral epicondyle (s1), as well as the terminal point of the curve tracing the medial margin of the diaphysis were highly variable along PC2. All fixed landmarks delimiting the extremities of the distal femur (s0-s5, s7) were major sources of variation for PC3. The two curves defining the width of the shaft at its mid-point were positioned more proximally and more tightly together in Sphenisciformes, depicting a shorter, more-stout shaft in Sphenisciformes compared with Procellariiformes. The distal end of the trochanteric crest was positioned more distally in Procellariiformes compared with Sphenisciformes. Projection of the trochanteric crest was a major source of variation for PC4, e.g. in Oceanitidae the upper-third of the crest projected further craniolaterally than in Procellariidae and some penguins (Figure 3.3d, see Appendix A Figure A.1). The proximal half of the curve tracing the medial margin of the diaphysis (c1) was positioned more medially for Oceanitidae and more laterally in Procellariidae and some penguins, depicting a wider proximal shaft in Oceanitidae. The fixed landmarks on the distal femur, especially s0, s1, s4, s5 and s7, were major sources of variation along PC4.
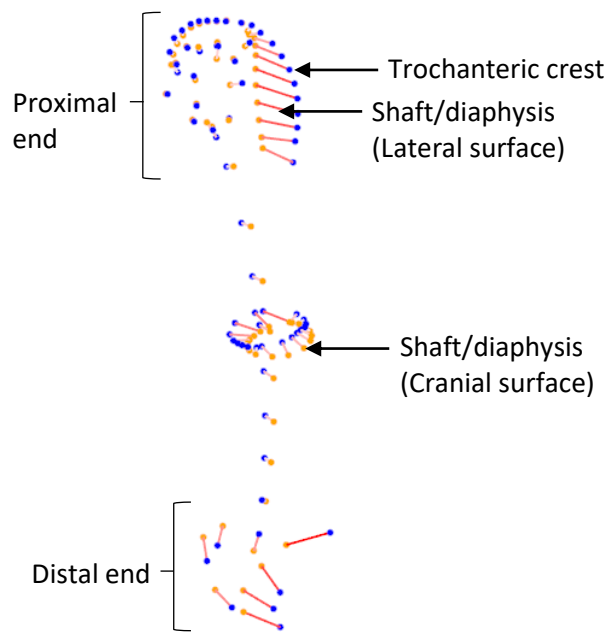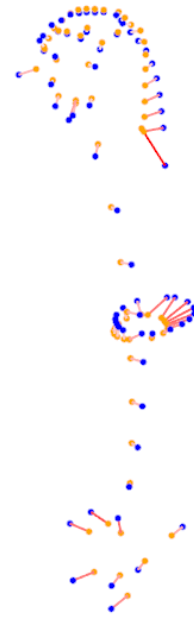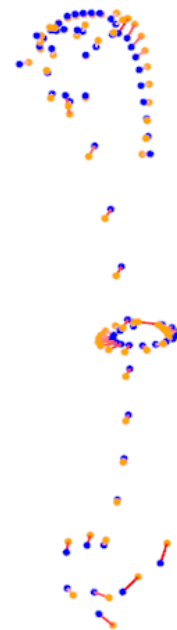
Figure 3.3. Variation in landmark configurations as represented by loadings for femora along (a) Principal component one (PC1), (b) PC2, (c) PC3 and (d) PC4. The length of the red line indicates the degree to which a landmark varies in its positioning (i.e. a longer line indicates greater variability).

3.3.2   Classification analyses on 3D landmarks in training set

Using both model 1 (bootstrap partial least squares discriminant analysis) and model 2 (repeated cross-validation partial least squares discriminant analysis) applied to femur shape all samples were assigned to the correct order with an overall 100% model prediction accuracy (Procellariiformes *n*= 41, Sphenisciformes *n* = 5) (Table 3.1). Performance measures for the 'positive' class Procellariiformes: balanced accuracy = 100%, sensitivity = 100%, specificity = 100%), and Sphenisciformes: balanced accuracy = 100%, sensitivity = 100%, specificity = 100%).

Using both model 1 (bootstrap partial least squares discriminant analysis) and model 2 (repeated cross-validation partial least squares discriminant analysis) applied to femur shape most samples were assigned to the correct family with an overall 93.5% model prediction accuracy (*n* = 46) (Table 3.2). This was partitioned into balanced accuracy computed as the average of the sensitivity and specificity values for each class respectively: Diomedeidae 95.6%, *n*= 12, Oceanitidae 100%, *n* = 4, Procellariidae 94%, *n* = 25, Spheniscidae 100%, *n* = 5). Three specimens belonging to Procellariidae were misclassified and assigned to Diomedeidae. All other specimens were assigned to the correct class.

Table 3.1. Order-level classification results from confusion matrix output using model 1 (bootstrap partial least squares discriminant analysis), and model 2 (repeated 3-fold cross-validation partial least squares discriminant analysis) applied to femur shape (ncomp = 1; Procellariiformes *n* = 41, Sphenisciformes *n* = 5). ncomp refers to the number of PLS components retained in the optimal model. Procellariiformes was the default 'positive' class outcome.

	Order-level classification					
	'Positive' class	Overall accuracy (%)	Sensitivity (%)	Specificity (%)	Balanced accuracy (%)	Specimens misclassified
Model 1	Procellariiformes	100	100	100	100	0
	Sphenisciformes	100	100	100	100	0
Model 2	Procellariiformes	100	100	100	100	0
	Sphenisciformes	100	100	100	100	0

Table 3.2. Family-level classification results from confusion matrix output using model 1 (bootstrap partial least squares discriminant analysis), and model 2 (repeated 3-fold cross-validation partial least squares discriminant analysis) applied to femur shape (ncomp = 6; Diomedeidae n = 12, Oceanitidae n = 4, Procellariidae n = 25, Spheniscidae n = 5). Note that overall accuracy is computed across all classes (i.e. the entire test set) and therefore only valid when considering all classes together (hence the n/a values for individual classes).

	Family-level classification						
	Class	**Overall accuracy (%)**	**Sensitivity (%)**	**Specificity (%)**	**Balanced accuracy (%)**	**Specimens misclassified**	**Misclassified to**
Model 1	Diomedeidae	n/a	100	91.1	95.6	0	n/a
	Oceanitidae	n/a	100	100	100	0	n/a
	Procellariidae	n/a	88	100	94	3	Diomedeidae
	Spheniscidae	n/a	100	100	100	0	n/a
	All classes	93.5	n/a	n/a	n/a	n/a	n/a
Model 2	Diomedeidae	n/a	100	91.1	95.6	0	n/a
	Oceanitidae	n/a	100	100	100	0	n/a
	Procellariidae	n/a	88	100	94	3	Diomedeidae
	Spheniscidae	n/a	100	100	100	0	n/a
	All classes	93.5	n/a	n/a	n/a	n/a	n/a

3.4 Discussion

Both the bootstrap and repeated cross-validation partial least squares discriminant analysis models (models 1 and 2, respectively) as applied to femur shape were highly successful in their ability to correctly predict new samples into their respective classes at both order- and family-level. Model performance was equally as good using either bootstrapping (with 25 repeats) or cross-validation (3-fold, repeated 10 times) as the resampling method for tuning and training the prediction models. The correct classification rates for both order- and family-level analyses (100%, 93.5%, respectively) were substantially higher than the null classification rate (25%).

Although the PCA based on femur shape revealed overlapping clusters between families of tubenosed birds (Diomedeidae, Oceanitidae and Procellariidae) along PC1 and PC2, clearer separation was found along PC1 and PC4 and hence these families were still able to be classified at a high rate through the inclusion of more (PLS) components in the PLS-DA model. The distribution of loadings revealed the shaft of the femur (i.e. degree of stoutness) and the position of the trochanteric crest as the major sources of variation in shape along PC1, distinguishing bones with scores at the extreme negative end (penguins) and the extreme positive end (tubenosed birds) (Figure 3.3). This explains the ability of the model to assign femora from penguins and tubenosed birds to the correct order with 100% accuracy. A potential application of the PLS-DA model could be in producing finer level classifications (genus or species) and applying this method to taxa other than birds.

4 GPSA

4.1 Introduction

As outlined in chapters 1 and 3, the objective of this thesis was to determine if 3D shape analyses of digitised bones can be used to confidently predict taxonomic groups for seabirds using partial least squares discriminant analysis (PLS-DA). For this chapter I have investigated the utility of a landmark-free shape analysis method for taxonomic classification. Generalized Procrustes Surface Analysis (GPSA; Pomidor et al., 2016) uses non-homologous 'pseudolandmarks' rather than traditional landmarks to quantify shape differences. A pseudolandmark is a point of correspondence among a collection of surfaces which is determined through an iterative process, whereas a fixed landmark represents a specifically-chosen homologous point for every object in a sample obtained through manual placement. The GPSA method automatically distributes a set of pseudolandmarks across an entire digital replica such that the pseudolandmarks are evenly spaced from one another. This is in contrast to the traditional landmark placement used in Chapter 3 where relatively few landmarks are manually placed on specific anatomical regions of interest. The GPSA method is a potentially more-automated approach that requires an operator to have very little anatomical knowledge, and therefore has the potential to be less susceptible to user-introduced error when compared with traditional landmark methods.

The specific objective of this study was to test the hypothesis that landmark-free 3D shape analyses using pseudolandmark-based PLS-DA can predict the taxonomic family to which a bird femur or humerus belongs. This is because family-level analyses are useful for both modern and fossil bones (as described in Chapter 1; see also: Eda et al., 2016b; Zeder & Spitzer, 2016; Seersholm et al., 2018; Horn et al., 2019). The classification methodology and objective used in this chapter are the same as was used in Chapter 3. For example, a classification rate substantially higher than the null classification rate is sought (Oliveri et al., 2018). The key difference between Chapter 3 and Chapter 4 is the source of the shape data for classification analysis. Here I used GPSA-derived shape data for partial least squares discriminant analysis to determine how well taxonomic groups could be predicted. As described in Chapter 1, seabirds were the focal group for this study due to the abundance of modern and older material in New Zealand museums.

4.2 Materials and methods

4.2.1 Materials

Three hundred and twelve digital replicas of left femora from extant species in Diomedeidae (n = 82), Oceanitidae (n = 19), Procellariidae (n = 190), and Spheniscidae (n = 21), and 274 digital replicas of left humeri from extant species in Diomedeidae (n = 70), Oceanitidae (n = 20), Procellariidae (n = 159), and Spheniscidae (n = 25), were used for Generalized Procrustes Surface Analysis (see Table 2.1; Table B.1 in Appendix B). Humeri and femora were used in separate analyses. The libraries of digitised bones were each divided into randomly-assigned training and test sets for statistical classification analyses. Approximately one quarter of each library was assigned to the test set in any one analysis.

4.2.2 Pseudolandmarks

Pseudolandmarks were used to describe the whole shape of bones belonging to tubenosed birds and penguins to inform analyses of shape variation across these groups. The automatic placement of pseudolandmarks allows for greatly reduced time and labour requirements compared with manual placement of landmarks. Homology and superimposition of surfaces are calculated using an iterative closest point (ICP) algorithm applied in Generalized Procrustes Surface Analysis version 20160308 (GPSA; Pomidor et al., 2016).

4.2.3 Generalized Procrustes Surface Analysis and principal component analysis

3D digital replicas were decimated to a common size before pseudolandmark placement by GPSA due to there being large differences in mesh sizes within both the femur and humerus datasets. Decimation to 2500 vertices was performed on all 3D digitised femora and humeri using the 'vcgQEdecim' function from the Rvcg package in R Studio (see Appendix I.1 R code for GPSA pseudo-landmark-based analyses). Following the method of Pomidor et al. (2016) shape data for each bone were then generated through the automatic placement of approximately 2500 evenly-spread pseudolandmarks onto each decimated 3D mesh using Generalized Procrustes Surface Analysis (GPSA) version 20160308 (Pomidor et al., 2016).

The first step in the GPSA method was to select a mean 'prototype' surface (i.e. the digital bone replica most representative of the typical shape across the sample of either femora or humeri). The prototype was then assigned as a reference to which each other digital replica in the sample was scaled and superimposed (Pomidor et al., 2016). Each point (i.e. vertex) on the reference was paired with its nearest vertex for each of the aligned digital replicas (Pomidor et al., 2016). The averaged position of the vertex pairings were then used to retopologise (i.e. remap) the vertices of the reference and aligned digital replicas (Pomidor et al., 2016). Correspondences between vertices in the reference and each other aligned replica were established using the retopologised vertices (Pomidor et al.,

2016). For this study, the retopologised vertices are characterised as pseudolandmarks that correspond between digital bone replicas. Pairwise distances calculated between corresponding pseudolandmarks provide a quantitative measure of shape disparity among the superimposed digital bone replicas i.e. their Procrustes surface metric (PSM; Pomidor et al., 2016). In a similar way to traditional Procrustes distance (i.e. generalized Procrustes analysis; GPA) (Gower, 1975) calculated between corresponding landmarks, the PSM can be used in subsequent analyses aimed at quantifying shape variation (Pomidor et al., 2016). The homologised points (i.e. Procrustes-transformed pseudolandmarks) for each 3D digital bone replica were exported from GPSA as a .dat file containing the homologised points of either the femora or humeri datasets. These .dat files were separately read into R studio version 1.2.1335 (R Team., 2019) using the 'fread' function in the data.table 1.13.0 package (Dowle et al., 2019). Pseuodolandmarks were then analysed with principal component analysis (PCA) (Figure 4.1; 4.2) using the 'gm.prcomp' function from the Geomorph 3.3.1 package (Adams & Otárola-Castillo, 2013) and partial least squares discriminant analysis (PLS-DA) (Table 4.1; 4.2) using functions from several packages including caret 6.0-86 (Kuhn, 2008; Kuhn et al., 2020), pls 2.7-3 (Mevik et al., 2020) and abind 1.4-5 (Plate et al., 2016) (see Appendix I.1 R code for GPSA pseudolandmark-based analyses).

Principal component analysis (PCA) was used as a visualisation tool to explore the variation in the femora and humeri pseudolandmark datasets separately. This technique reduced the dimensionality of the data down to the most important sources of variation, thereby revealing the groupings that the classification analysis would be based on (Figure 4.1; 4.2) i.e. by revealing groupings of specimens based on similar shape, and detecting any outlier bones (Webster & Sheets, 2010; Cooke & Terhune, 2015). Loadings derived from the PCA illustrated how the variation in pseudolandmarks was weighted across a mean shape i.e. they revealed the degree to which a pseudolandmark varied in each dimension (i.e. x, y, z coordinates) across all digital bone replicas in the sample, and therefore which regions of the bone contributed the most to the variance explained by a given principal component (Figure 4.4; 4.5).

4.2.4   *Classification analyses on pseudolandmarks in training set*
Membership of each bone to a taxonomic order or family was predicted using the PLS-DA classification modelling protocol developed in Chapter 3 Femur landmarks. For full classification method details see Chapter 1.4 Statistical classification and Chapter 3.2.4 Classification analyses on 3D landmarks in training set.

4.3 Results

4.3.1 Principal component analysis

The first 269 principal components (PCs) accounted for 95% of the variation in femur pseudolandmarks (Figure 4.3a). Principal component one (PC1) explained 21.5% of the variation in femoral shape as defined by pseudolandmarks, and PC2 explained 8.2% of the variation (Figure 4.1a). Principal component three, four and five accounted for 5.4%, 4.4%, 2.7% respectively. A relatively clear separation at order-level (i.e. between tubenosed birds and penguins) was found along PC2 and PC4 (Figure 4.1b). A relatively clear separation at family level (i.e. between Procellariidae, Diomedeidae, Oceanitidae, Spheniscidae) was found along PC4 and PC5 (Figure 4.1c-e). Scores representing femur shape in tubenosed birds and penguins clustered at the positive and negative ends of both PCs 4 and 5 respectively, indicating a distinct separation between these groups (Figure 4.1c-e). Separation between tubenosed bird families was also best along PC4 and PC5 with Oceanitidae in particular forming a cluster distinct from those of Diomedeidae and Procellariidae which overlapped with one another. Clear separation of some tubenosed bird genera was found along PC1 and PC5 e.g. *Diomedea*, *Pelagodroma*, *Procellaria* and *Pterodroma* formed distinct clusters (within their respective families) (Figure H.1).

The first 174 PCs accounted for 95% of the variation in humerus pseudolandmarks (Figure 4.3b). Principal component one (PC1) explained 26.8% of the variation in humeral shape as defined by pseudolandmarks, and PC2 explained 9.7% of the variation (Figure 4.2a). Principal component three, four and five accounted for 4%, 3.5%, 2.1% respectively. A relatively clear separation at order-level was found along PC1 and PC2 (Figure 4.2a). A relatively clear separation at family level was found along PC1 and PC3 (Figure 4.2b-d). Separation between tubenosed bird families was best along PC2 and PC3 with each family forming a distinct cluster. Clear separation of some tubenosed bird genera was found along PC2 and PC3 e.g. *Diomedea*, *Pelagodroma*, *Pelecanoides, Procellaria*, *Pterodroma* and *Puffinus* formed distinct clusters within their respective families (Figure H.2).
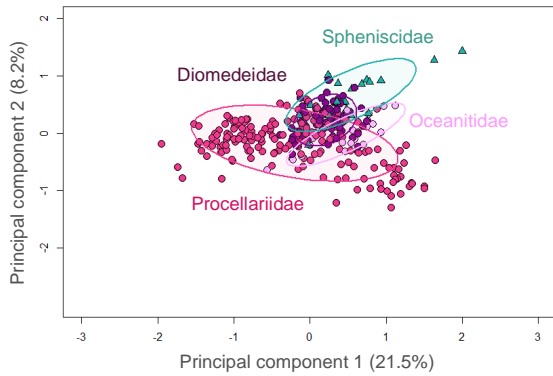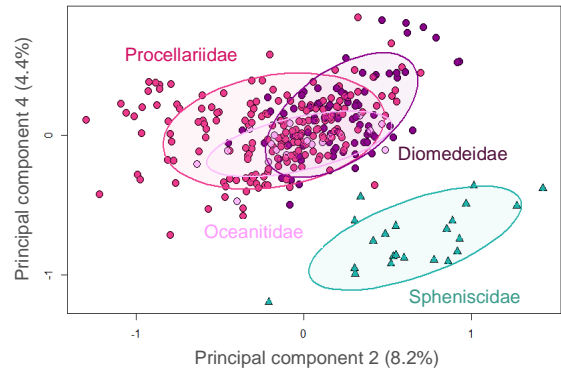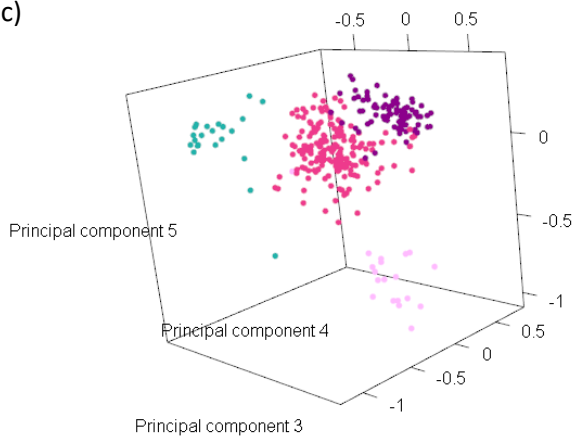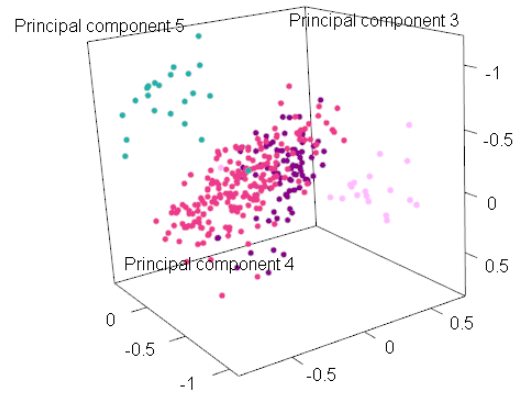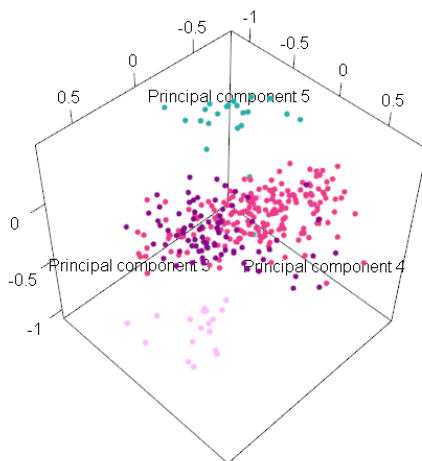
Figure 4.1. Morphospace reflecting disparity in the shape of femora from tubenosed birds (Diomedeidae, Oceanitidae, Procellariidae) and penguins (Spheniscidae) as shown by scores from principal component analysis of Procrustes-transformed pseudolandmark data. a) PC1 vs PC2, b) PC2 vs PC4 and c-d) PC3 vs PC4 vs PC5. All figures use the same colour key described in a) and b). 95% confidence ellipses (*a* = 0.05) used here and throughout.
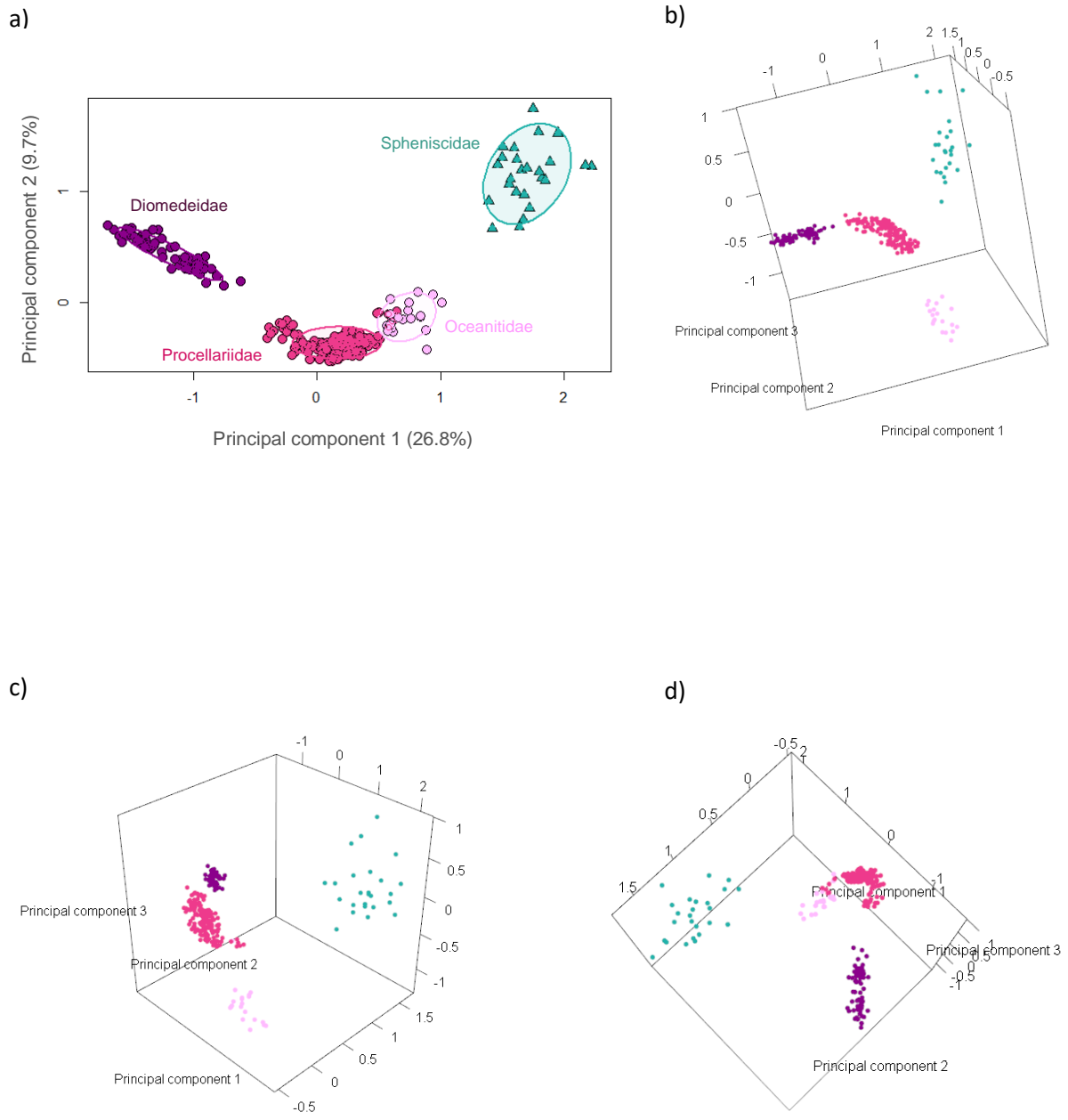
Figure 4.2. Morphospace reflecting disparity in the shape of humeri from tubenosed birds (Diomedeidae, Oceanitidae, Procellariidae) and penguins (Spheniscidae) as shown by scores from principal component analysis of Procrustes-transformed pseudolandmark data. a) PC1 vs PC2 and b-d) PC3 vs PC4 vs PC5. All figures use the same colour key described in a).

a)
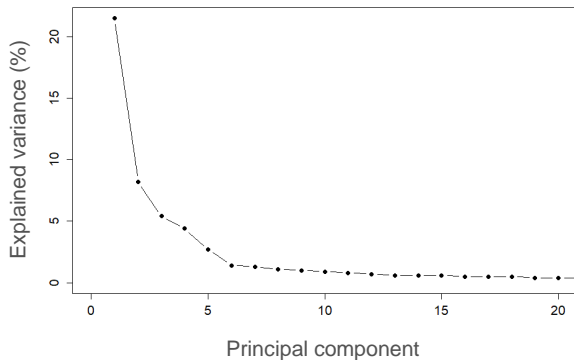
b)
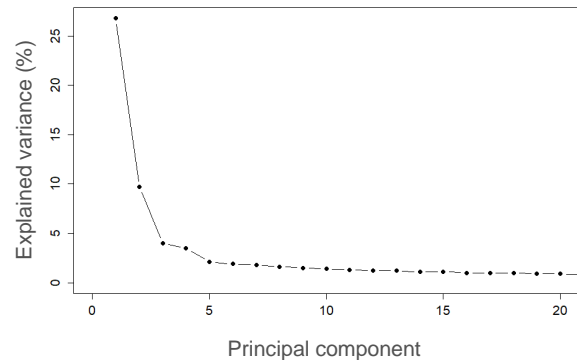
Figure 4.3. Scree plots showing the percentage of variance explained by each of the first 20 principal components from PCA on pseudolandmark shape data from a) femora and b) humeri.

Principal component one identified several highly variable regions of in the femur dataset including the articular surface of the head, impressions of the obturator muscles, caudal, medial and lateral surfaces of the proximal femur, the entire cranial surface (with partial inclusion of lateral and medial surfaces) of the shaft, proximal, proximolateral and caudal regions of the lateral condyle, and the medial surface of the medial condyle (Figure 4.4). Regions of the femora that were major sources of variation along PC2 included the trochanteric crest, proximal surface of the head, the lower two-thirds of the caudal surface of the shaft, the mid-craniolateral surface of the shaft, the cranial and distal surfaces of the medial condyle, and the region around the intercondylar sulcus. The greatest sources of variation along PC3 were the proximal surface of the head and the distal surface of the distal femur (specifically the region around the intercondylar sulcus). The major sources of variation along PC4 were the distal surface of the lateral condyle and the distal surface and mid-region of the proximal surface of the femoral head. The major sources of variation along PC5 were the proximomedial region of the head, the medial-articular surface of the head, the proximal end of the trochanteric crest, the cranial and cranio-lateral surfaces of the lateral condyle, the proximo-cranial surface of the medial condyle, and the region around the popliteal fossa.

For the humerus the major sources of variation along PC1 included the proximocaudal region of the head, ventral tubercle, dorsal crest, the upper-third of the posterocranial and anterior surfaces of the shaft, dorsal supracondylar tubercle, the proximal and posterior regions of the ventral epicondyle and the fossa musculus (m.) brachialis (Figure 4.5). The greatest sources of variation along PC2 were the distal and posterocranial regions of the tuberculum ventrale (i.e. including the dorsal crest and bicipital crest), the caudal region of the head including the tuberculum dorsale, both the distal humerus and humeral shaft, dorsal supracondylar tubercle, fossa m. brachialis, the proximal

37

surface of the dorsal condyle, the upper-third of the caudal and anterior surfaces (with partial inclusion of the posterior surface), upper two-thirds of the anterior surface and lower-third of the cranial surface of the shaft. The greatest sources of variation along PC3 were the ventral tubercle, dorsal crest, impressions of the caudal latissimus dorsi muscle and retinaculum scapulotricipitalis muscle, as well as the anterior surface, upper-third of the cranial surface and lower quarter of both the caudal and posterior surfaces of the shaft.
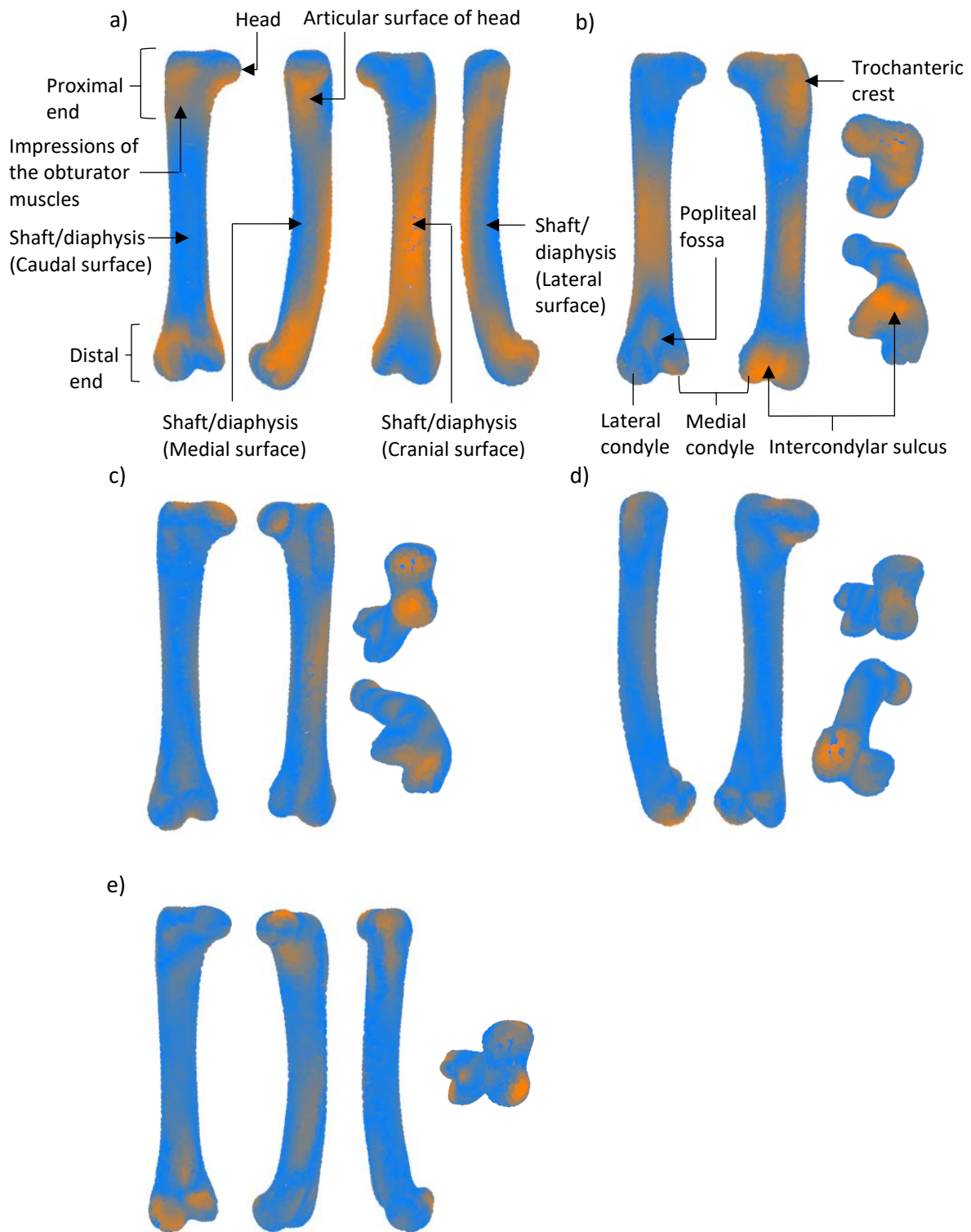
Figure 4.4. Variation in pseudolandmarks as represented by loadings for femora along (a) Principal component one (PC1), (b) PC2, (c) PC3 (d) PC4 and (e) PC5. Orange represents pseudolandmarks with comparatively larger loadings (i.e. greater amounts of variation) for the respective principal component, while blue shows pseudolandmarks with comparatively smaller loadings (i.e. smaller amounts of variation) for the respective principal component. Loadings code adapted from Adams and Otárola-Castillo (2013).
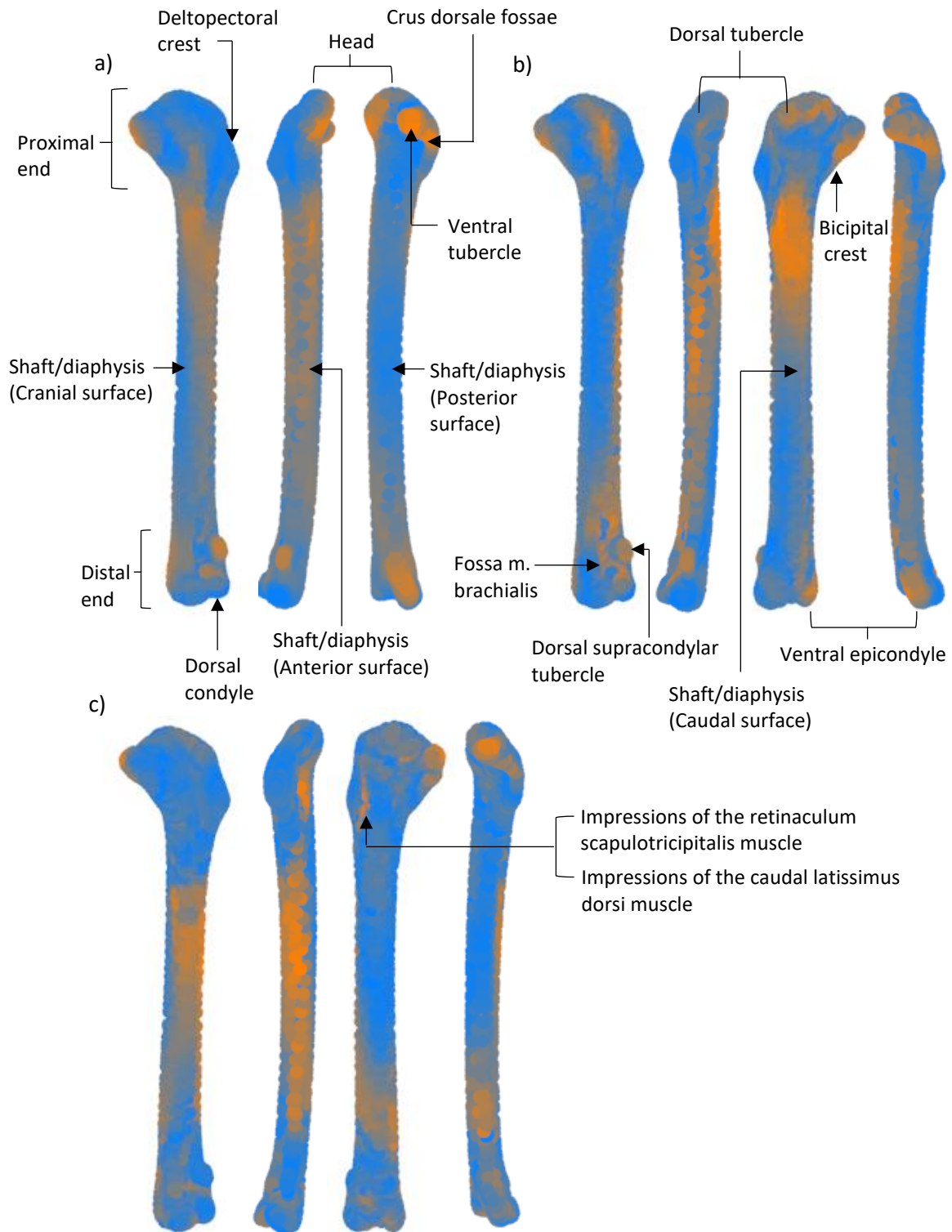
Figure 4.5. Variation in pseudolandmarks as represented by loadings for humeri along (a) PC1, (b) PC2, (c) PC3. Orange represents pseudolandmarks with comparatively larger loadings (i.e. greater amounts of variation) for the respective principal component, while blue shows pseudolandmarks with comparatively smaller loadings (i.e. smaller amounts of variation) for the respective principal component. Loadings code adapted from Adams and Otárola-Castillo (2013).

4.3.2 Classification analyses on pseudolandmarks in training set

Using both model 1 (bootstrap partial least squares discriminant analysis) and model 2 (repeated cross-validation partial least squares discriminant analysis) applied to femur shape all samples were assigned to the correct order with an overall 100% model prediction accuracy (number of components = 2; Procellariiformes n = 72, Sphenisciformes n = 5) (Table 4.1). Using both model 1 and model 2 applied to humerus shape all samples were also assigned to the correct order with an overall 100% model prediction accuracy (number of components = 1; Procellariiformes n = 62, Sphenisciformes n = 6) (Table 4.1).

Again, using both model 1 and model 2 applied to femur shape all samples were assigned to the correct family with an overall 100% model prediction accuracy (number of components = 11; N = 87) (Table 4.2). This was partitioned into balanced accuracy computed as the average of the sensitivity and specificity values for each class respectively: Diomedeidae 100%, n = 20, Oceanitidae 100%, n = 4, Procellariidae 100%, n = 47, Spheniscidae 100%, n = 5. Likewise, both model 1 and model 2 applied to humerus shape assigned all samples to the correct family with an overall 100% model prediction accuracy (number of components = 7; N = 67) (Table 4.2). This was partitioned into balanced accuracy computed as the average of the sensitivity and specificity values for each class respectively: Diomedeidae 100%, n = 17, Oceanitidae 100%, n = 5, Procellariidae 100%, n = 39, Spheniscidae 100%, n = 6).

Table 4.1. Order-level classification of femur and humerus shape. Results from confusion matrix output using model 1 (bootstrap partial least squares discriminant analysis) and model 2 (repeated 3-fold cross-validation partial least squares discriminant analysis). Femur shape analyses used two components (Procellariiformes *n* = 72, Sphenisciformes *n* = 5) and humerus shape analyses used one component (Procellariiformes *n* = 62, Sphenisciformes *n* = 6). Procellariiformes was the default 'positive' class outcome.

	Order-level classification					
	'Positive' class	**Overall accuracy (%)**	**Sensitivity (%)**	**Specificity (%)**	**Balanced accuracy (%)**	**Specimens misclassified**
FEMUR						
Model 1	Procellariiformes	100	100	100	100	0
	Sphenisciformes	100	100	100	100	0
Model 2	Procellariiformes	100	100	100	100	0
	Sphenisciformes	100	100	100	100	0
HUMERUS						
Model 1	Procellariiformes	100	100	100	100	0
	Sphenisciformes	100	100	100	100	0
Model 2	Procellariiformes	100	100	100	100	0
	Sphenisciformes	100	100	100	100	0

Table 4.2 (next page). Family-level classification of femur and humerus shape. Results from confusion matrix output using model 1 (bootstrap partial least squares discriminant analysis) and model 2 (repeated 3-fold cross-validation partial least squares discriminant analysis). Femur shape analyses required 11 components (Diomedeidae *n* = 20, Oceanitidae *n* = 4, Procellariidae *n* = 47, Spheniscidae *n* = 5). Humerus shape analyses required seven components (Diomedeidae *n* = 17, Oceanitidae *n* = 5, Procellariidae *n* = 39, Spheniscidae *n* = 6). Note that overall accuracy is computed across all classes (i.e. the entire test set) and therefore only valid when considering all classes together (hence the n/a values for individual classes).

	Family-level classification					
	Class	Overall accuracy (%)	Sensitivity (%)	Specificity (%)	Balanced accuracy (%)	Specimens misclassified	Misclassified to

FEMUR

Model 1

	Diomedeidae	n/a	100	100	100	0	n/a
	Oceanitidae	n/a	100	100	100	0	n/a
	Procellariidae	n/a	100	100	100	0	n/a
	Spheniscidae	n/a	100	100	100	0	n/a
	All classes	100	n/a	n/a	n/a	n/a	n/a

Model 2

	Diomedeidae	n/a	100	100	100	0	n/a
	Oceanitidae	n/a	100	100	100	0	n/a
	Procellariidae	n/a	100	100	100	0	n/a
	Spheniscidae	n/a	100	100	100	0	n/a
	All classes	100	n/a	n/a	n/a	n/a	n/a

HUMERUS

Model 1

	Diomedeidae	n/a	100	100	100	0	n/a
	Oceanitidae	n/a	100	100	100	0	n/a
	Procellariidae	n/a	100	100	100	0	n/a
	Spheniscidae	n/a	100	100	100	0	n/a
	All classes	100	n/a	n/a	n/a	n/a	n/a

Model 2

	Diomedeidae	n/a	100	100	100	0	n/a
	Oceanitidae	n/a	100	100	100	0	n/a
	Procellariidae	n/a	100	100	100	0	n/a
	Spheniscidae	n/a	100	100	100	0	n/a
	All classes	100	n/a	n/a	n/a	n/a	n/a

4.4   Discussion

Both the bootstrap and repeated cross-validation partial least squares discriminant analysis models (models 1 and 2, respectively) as applied to both femur and humerus shape were highly successful in their ability to correctly predict new samples into their respective classes at both order- and family-level. Model performance was equally as good using either bootstrapping (with 25 repeats) or cross-validation (3-fold, repeated 10 times) as the resampling method for tuning and training the prediction models. The correct classification rates for both order- and family-level analyses (100%, 100%, respectively) for both the femur and humerus were substantially higher than the null classification rate (25%).

Although the PCA based on femur shape revealed overlapping clusters between all families (Diomedeidae, Oceanitidae, Procellariidae and Spheniscidae) along PC1 and PC2, clearer separation between these classes was found along PC3, PC4 and PC5. Coupled with the observation that PLS-DA analyses required several components, we can see that class-informative variation for femora is distributed across several components. The distribution of loadings revealed the trochanteric crest, proximal surface of the femoral head, middle region on the cranial and caudal surfaces of the femoral shaft, as well as the cranial and distal surfaces of the distal femur as the major sources of variation in femur shape along PC2, distinguishing bones with scores at the negative end (tubenosed birds) and positive end (penguins). The distal surface of the lateral condyle, and distal surface and mid-region of the proximal surface of the femoral head were major sources of variation in femur shape along PC4, distinguishing bones with scores at the negative end (penguins) and positive end (tubenosed birds). These distributions of loadings (i.e. along PC2 and PC4) explain the ability of the model to assign femora from penguins and tubenosed birds to the correct order with 100% accuracy.

The PCA based on humerus shape revealed distinct clusters for all families (Diomedeidae, Oceanitidae, Procellariidae and Spheniscidae) along the axes of maximum variance (i.e. PC1 and PC2) which explains the relatively fewer PLS components required for optimal classification performance for the humerus (i.e. one component for order-level analyses and seven components for family-level) compared with the femur (i.e. two components for order-level analyses and 11 components for family-level). The distribution of loadings revealed the proximal surface of the humeral head, ventral tubercle, cranial and anterior surfaces at the proximal end of the humeral shaft, dorsal supracondylar tubercle, and ventral epicondyle as the major sources of variation in humerus shape, distinguishing bones with scores ranging from the extreme negative-to-slightly positive end (tubenosed birds) and the extreme positive end (penguins). The caudal and posterior surfaces at the proximal end, and the entire cranial surface of the humeral shaft, dorsal crest, and the cranial surface of the distal femur

were the major sources of variation in humerus shape along PC2. Variation in these features enabled the PLS-DA models to assign humeri from penguins and tubenosed birds to the correct order with 100% accuracy.

Classification results from pseudolandmark-based PLS-DA should be interpreted with caution if damaged or incomplete bones are included in the GPSA, as this will introduce sources of variation into the dataset through artifacts unrelated to shape. The femur dataset included some bones with specimen labels on the cranial shaft (e.g. 2006-48-4 *Ardenna creatopus*, 2006-48-5 *Ardenna creatopus,* AV39574 *Pelecanoides exsul cf georgicus*), caudal shaft (e.g. 2006471 *Pelecanoides georgicus*), and one bone with a damaged/incomplete femoral head (e.g. DM12840 *Eudyptes chrysolophus*) (see Table B.1 in Appendix B). However, note that none of these regions were highly loaded along any of the class-informative principal components (i.e. PCs 1-5; see Figure 4.4). The humerus dataset included some bones with flesh attached to the humeral head and ventral tubercle (e.g. AV22964 *Oceanites oceanicus*, LB9396 *Pelagodroma marina,* 214 *Phoebetria palpbebrata*), as well as an incomplete deltopectoral crest (e.g. AV30697 *Procellaria cinerea*, LB9396 *Pelagodroma marina*, LB13699 *Pelagodroma marina*, LB15101 *Pelagodroma marina*, 23141 *Pterodroma leucoptera caledonica*), and one bone with a specimen label on the caudoanterior surface of the shaft (e.g. 2006471 *Pelecanoides georgicus*) (see Table B.1 in Appendix B). Of these regions, the ventral tubercle was highly loaded along the most informative principal components (i.e. PCs 1-3; see Figure 4.5); however, we note that this is a morphological feature of the humerus that is known to vary in its orientation (i.e. oriented caudally, cranioventrally, or ventrally) among seabirds (see Ksepka et al., 2012; Degrange et al., 2018; Thomas et al., 2020b). All other regions of the humerus mentioned above were not highly loaded along PCs 1-3 (see Figure 4.5). A potential application of the pseudolandmark-based PLS-DA model could be in producing finer level classifications (genus or species) and applying this method to taxa other than birds.

5 Discussion

5.1 Classification accuracy

The 3D shape-based taxonomic classification method developed in this study was highly successful at correctly assigning seabird bones to their correct order and family. Landmark-based partial least squares discriminant analysis (PLS-DA) assigned femora from penguins and tubenosed birds to the correct order and family with 100% and 93.5% accuracy, respectively (Table 3.1; 3.2). Pseudolandmark-based PLS-DA assigned femora and humeri from penguins and tubenosed birds to both the correct order and family with 100% accuracy (Table 4.1; 4.2). The classification rates recovered in this study were therefore substantially higher than the null classification rate (25%) (Oliveri et al., 2018). The slightly higher classification accuracy from pseudolandmark-based PLS-DA may be due to the greater amount of shape data obtained for each bone through the Generalized Procrustes Surface Analysis method (i.e. 7500 data points per sample), compared with the landmark-based shape analysis (216 data points per sample). Overall though, classifications performed in this study support the hypothesis that both traditional landmark-based and novel pseudolandmark-based 3D shape analyses combined with partial least squares discriminant analysis can be used to confidently predict taxonomic identities for seabird femora and humeri to at least family-level.

5.2 Classification-informative variation

Loadings from both landmark- and pseudolandmark-based principal component analyses revealed that the position and projection of the trochanteric crest of femora, and the robustness of the femoral shaft, were the main features that distinguished Procellariiformes from Sphenisciformes (Figure 3.3; 4.4). The trochanteric crest is a recognised morphological feature for which the degree of extension distally, and projection out, from the lateral shaft of the proximal femur, as well as the degree of projection above the femoral head (i.e. degree of proximal projection) are characters included in discrete character matrices. This type of information about femoral morphology can be useful for identifying and classifying seabird taxa (e.g. Clarke et al., 2003; Slack et al., 2006; Ksepka & Clarke, 2010; Smith, 2011; Tennyson & Mannering, 2018; Thomas et al., 2020). Shaft robustness (i.e. midshaft width) is also a recognised feature of the femur used in discrete character analysis of seabirds (e.g. Thomas et al., 2020).

Interestingly, pseudolandmark-based analysis of humeri revealed the ventral tubercle as one of the main features distinguishing penguins from tubenosed birds, despite being just one small

feature contributing to a very different overall humerus shape between these taxa (Figure 4.5). The ventral tubercle is also a recognised morphological feature of the humerus for which both the orientation (i.e. oriented caudally, cranioventrally, or ventrally) and degree of caudal projection are known to vary among seabird taxa (see Smith & Clarke, 2011; Ksepka et al., 2012; Hoffmeister, 2014; Degrange et al., 2018; Thomas et al., 2020b). Other morphological features that distinguished humeri at order-level which are also recognised morphological characters were development of the dorsal supracondylar tubercle (e.g. Mayr et al., 2017; Thomas et al., 2020), depth, size and shape of the fossa for the origin of m. brachialis (e.g. Mayr et al., 2002; Tennyson & Mannering, 2018; Thomas et al., 2020), and shaft length, width and flatness i.e. shaft robustness (e.g. Olson, 2008; Hoffmeister, 2014; Tennyson & Mannering, 2018; Thomas et al., 2020). These findings show that the same highly-loaded regions are found using both a supervised approach (i.e. landmarks) and an unsupervised approach (i.e. pseudolandmarks) to shape analysis.

Principal component analysis of femur shape produced generally similar results for the manually-placed landmark dataset when compared with results from the automatically-placed pseudolandmark dataset (i.e. generally similar distributions of component scores, informed by similar loadings) (Figure 3.2; 4.1). The pseudolandmark analysis required 269 components to explain 95% of the variation in femur shape compared with the 25 components needed to explain 95% of the femur shape captured by manually-placed landmarks (Figure 4.3a; 3.2). More variation was explained by principal component 1 (PC1) and PC2 in the manually-placed landmark analysis of femur shape compared with PC1 and PC2 from the pseudolandmark analysis of femur shape (PC1 31.6% vs 21.5%; PC2 19.2% vs 8.2%). These differences are likely due to the greater amount of shape information included in the pseudolandmark analysis. This is because more coverage of each bone is achieved through the GPSA. Consequently, more components may be required to explain the additional sources of shape variation, with each component explaining a relatively low amount compared with the landmark analysis.

5.3   *Pseudolandmarks or landmarks?*

Loadings for both landmarks and pseudolandmarks showed that variation was weighted on similar anatomical regions (Figure 3.2; 4.3). The femoral shaft (i.e. degree of stoutness) was a major source of variation along PCs 1-4 for landmarks and along PC1 and PC2 for pseudolandmarks. The position and projection of the trochanteric crest was also a major source of variation along PCs 1-4 for landmarks and along PC2 and PC5 for pseudolandmarks. The lateral and medial condyles were major sources of variation along PCs 1-4 for landmarks and along PCs 1-5 for pseudolandmarks. For the

landmark dataset these sources of variation allowed us to distinguish bones with scores at the extreme negative end (penguins) and the extreme positive end (tubenosed birds) of PC1, while for the pseudolandmark dataset these same features or regions allowed order-level separation but this was instead found in relatively higher dimension components (i.e. PC2 and PC4) (Figure 3.2a; 4.1b). Again, the additional shape information included in the pseudolandmark analysis means that shape variation was spread across more components with each component explaining a relatively low amount of variation compared with the landmark analysis. However, as traditional landmarks and pseudolandmarks are identifying the same features or regions, and recovering the same classification rates, we recommend that future research utilise the more-automated pseudolandmark approach due to the greatly reduced time and labour requirements compared with manual landmark placement.

5.4 Future directions

5.4.1 Genus-level analyses

Principal component analysis of both femur and humerus shape revealed some readily identifiable clusters in morphospace that were occupied by a single genus. This was observed for both the femur landmark analysis (i.e. along PC1 and PC4) and pseudolandmark analysis (i.e. along PC1 and PC5), and for the humerus pseudolandmark analysis (i.e. along PC2 and PC3). Notably, the genera representing these clusters differed between the femur landmark and pseudolandmark analysis (Figure G.1; H.1). *Diomedea*, *Pelagodroma* and *Pterodroma* clustered across both femur analyses*,* while clustering of *Ardenna* and *Garrodia* was unique to the landmark morphospace and clustering of *Procellaria* was unique to the pseudolandmark morphospace. Genera that clustered in morphospace for the humerus pseudolandmark analysis included those that were common across both femur analyses, in addition to *Pelecanoides*, *Procellaria* and *Puffinus*. These findings are an initial indication that genus-level identifications may be possible through the application of our method. Future research could investigate this idea by incorporating more species into a much larger dataset.

We note that a large dataset was needed for the classification method developed here to be successful, even for family-level analysis. Throughout the dataset generation and model building process classification accuracy was shown to improve as more bones were included in the analysis (data not reported in this thesis). Furthermore, in addition to surface scanning, microCT imaging was also required to cover the full size range of specimens and therefore allow a more inclusive dataset for order Procellariiformes. For this study we were limited to family-level resolution of taxonomic identity as our sample size was not large enough to allow genus-level analysis. Here I would speculate

that at least twice the number of species would be needed to achieve genus-level resolution. This is because of the reduced shape disparity between genera compared with families within Procellariiformes.

5.4.2   Fossil preservation

An important consideration when using pseudolandmarks to quantify shape is the condition of the bones included in the Generalized Procrustes Surface Analysis (GPSA; Pomidor et al., 2016). As noted in Chapter 4, damaged or incomplete bones will introduce sources of variation into the dataset through artifacts unrelated to the original shape of the bone. These shape artifacts may negatively impact the classification results of the pseudolandmark-based PLS-DA. We note that both the femur and humerus datasets contained some bones with such artifacts i.e. dried muscle tissue, missing or damaged regions; however, only one of these regions was highly loaded along the class-informative principal components. The ventral tubercle on the humerus was associated with dried tissue attached to some bones and was a highly loaded region along PCs 1-3 (see Figure 4.5). However, the ventral tubercle is a recognised morphological feature of the humerus that is known to vary in its orientation among seabirds (see Smith & Clarke, 2011; Ksepka et al., 2012; Hoffmeister, 2014; Degrange et al., 2018; Thomas et al., 2020b) and is therefore not an unexpected source of variation. A future method might consider a pre-processing step that allows damaged or obscured regions of bones to be excluded from shape analyses. This might take the form of a region selection tool in R.

5.4.3   Novel taxonomic classification method

Few studies have explored 3D shape-based classification analysis for the taxonomic identification of individual bones. A study by Drake et al. (2015) used cross-validation quadratic discriminant analysis (QDA) based on cranial morphology in ancient and modern dogs and wolves to identify two Paleolithic fossil canid skulls. Hanot et al. (2017) used k-nearest neighbors (k-NN) classification based on equid bone shape of cranial and postcranial elements to identify domestic horses and donkeys from archaeological specimens. Here, we have used partial least squares discriminant analysis applied to both traditional landmark-based and novel pseudolandmark-based (i.e. GPSA) shape analyses for the classification of postcranial elements of seabirds. Our PLS-DA-based method can confidently predict taxonomic identities for seabird femora and humeri to at least family-level, with probable extension to genus- or species-level identifications and generalisation to other groups. This method could reliably contribute to the identification of both modern and fossil bird remains when only incomplete skeletons (i.e. isolated elements) are available and molecular methods are not possible. While traditional landmark-based shape analysis still requires some initial user training and considerable input of time and labour, our more-automated pseudolandmark-based method is free of these constraints, thus providing an advance on previous 3D-shape based taxonomic classification research.

The femur is a much more challenging bone than the humerus in that direct visual observations of femoral morphology of tubenosed birds and penguins are not especially useful for distinguishing between closely-related and similarly-sized species within the same family (e.g. Mayr & Smith, 2012; Tennyson & Mannering, 2018; Thomas et al., 2020b). Thus, the key test for our study was to determine if the femur could be used to classify seabird bones based on 3D geometric morphometric descriptions of shape. We found that femoral shape performed exceptionally well with classification rates comparable to those of the humerus. The major implication of this finding is that taxonomic classification may be performed using 3D geometric morphometrics of typically undiagnostic bones. Our pseudolandmark-based PLS-DA method could be adapted for analysing fragmentary bones and subsequently applied to zooarchaeological studies where reliably distinguishing postcranial elements between closely-related taxa can be difficult due to the often incomplete nature of the bones, and the unreliable or sometimes complete lack of morphological criteria for bone identification (e.g. Zeder & Lapham, 2010; Hanot et al., 2017).

5.5 Conclusions

Here we present a novel method for predicting taxonomic groups for seabirds using PLS-DA modelling applied to 3D bone shape. Our results are a promising indication of the future utility of this method which has so far been used to assign seabird bones to their correct order and family. Further study could allow finer-resolution identifications (e.g. genus-level) but would require a much broader comparative sample involving more species. Our method could be used for identifying both modern and fossil bone remains, with particular relevance to cases where only isolated or undiagnostic bones are available and molecular methods are not applicable. More generally the method could be applied to taxa other than birds e.g. mammals. Furthermore, our pseudolandmark-based method could enable a more-automated approach to taxonomic identification.

6   References

Adams, D. C., & Otárola-Castillo, E. (2013). geomorph: an R package for the collection and analysis of geometric morphometric shape data. *Methods in Ecology and Evolution, 4*(4), 393-399. https://doi.org/10.1111/2041-210X.12035

Adams, D. C., Rohlf, F. J., & Slice, D. E. (2013). A field comes of age: geometric morphometrics in the 21st century. *Hystrix, the Italian Journal of Mammalogy, 24*(1), 7-14. https://lib.dr.iastate.edu/cgi/viewcontent.cgi?article=1115&context=eeob_ag_pubs

Ahlinder, J., Nordgaard, A., & Lindström, S. W. (2015). Chemometrics comes to court: evidence evaluation of chem–bio threat agent attacks. *Journal of Chemometrics, 29*(5), 267-276. https://doi.org/10.1002/cem.2699

Allentoft, M. E., Scofield, R. P., Oskam, C. L., Hale, M. L., Holdaway, R. N., & Bunce, M. (2012). A molecular characterization of a newly discovered megafaunal fossil site in North Canterbury, South Island, New Zealand. *Journal of the Royal Society of New Zealand, 42*(4), 241-256. https://doi.org/10.1080/03036758.2011.574821

Bardua, C., Felice, R. N., Watanabe, A., Fabre, A.-C., & Goswami, A. (2019a). A practical guide to sliding and surface semilandmarks in morphometric analyses. *Integrative Organismal Biology, 1*(1), obz016. https://academic.oup.com/iob/article/1/1/obz016/5526881

Bardua, C., Wilkinson, M., Gower, D. J., Sherratt, E., & Goswami, A. (2019b). Morphological evolution and modularity of the caecilian skull. *BMC Evolutionary Biology, 19*(1), 1-23. https://bmcecolevol.biomedcentral.com/track/pdf/10.1186/s12862-018-1342-7.pdf

Barker, M., & Rayens, W. (2003). Partial least squares for discrimination. *Journal of Chemometrics: A Journal of the Chemometrics Society, 17*(3), 166-173. https://analyticalsciencejournals.onlinelibrary.wiley.com/doi/epdf/10.1002/cem.785

Bassbasi, M., De Luca, M., Ioele, G., Oussama, A., & Ragno, G. (2014). Prediction of the geographical origin of butters by partial least square discriminant analysis (PLS-DA) applied to infrared spectroscopy (FTIR) data. *Journal of Food Composition and Analysis, 33*(2), 210-215. https://doi.org/https://doi.org/10.1016/j.jfca.2013.11.010

Baumel, J., & Witmer, L. (1993). Osteologia. In: Baumel JJ, King AS, Breazile JE, Evans HE, Van den Berge JC, editor. Handbook of avian anatomy: nomina anatomica avium. 2nd ed (pp. 45–132). *Nuttall Ornithological Club.*

Blender Online Community. (2019). Blender–a 3D modelling and rendering package. Blender Foundation, Stichting, Amsterdam.

Bookstein, F. L. (1977). The study of shape transformation after D'Arcy Thompson. *Mathematical Biosciences, 34*(3), 177-219. https://www.sciencedirect.com/science/article/pii/0025556477901018

Bookstein, F. L. (1991). *Morphometric tools for landmark data* Cambridge University Press.

Bookstein, F. L. (1997). Landmark methods for forms without landmarks: morphometrics of group differences in outline shape. *Medical Image Analysis, 1*(3), 225-243. https://reader.elsevier.com/reader/sd/pii/S1361841597850128?token=1A485093C71BC405E08A2A4556B4677B7D36EAED34E81385EFA09AB7E91A3157CFA108EAFA07373B681E9F082F549458

Borboroglu, P. G., & Boersma, P. D. (2015). *Penguins: natural history and conservation*. University of Washington Press.

Breno, M., Leirs, H., & Van Dongen, S. (2011). Traditional and geometric morphometrics for studying skull morphology during growth in *Mastomys natalensis* (Rodentia: Muridae). *Journal of Mammalogy, 92*(6), 1395-1406. https://doi.org/10.1644/10-mamm-a-331.1

Bright, J. A., Marugan-Lobon, J., Cobb, S. N., & Rayfield, E. J. (2016). The shapes of bird beaks are highly controlled by nondietary factors. *Proceedings of the National Academy of Sciences of the United States of America, 113*(19), 5352-5357. https://doi.org/10.1073/pnas.1602683113

Brownlee, J. (2020). Machine Learning Mastery: Making Developers Awesome at Machine Learning. https://machinelearningmastery.com/

Bruker. (2021). *3D X-RAY MICROSCOPY (XRM): Object Stages for In-Situ XRM*. https://www.bruker.com/en/products-and-solutions/microscopes/3d-x-ray-microscopes/object-stages-for-in-situ-examination.html

Bruker Optiks. (2021). SkyScan 1172 microCT system. Ettlingen, Germany.

Bruner, E. (2004). Geometric morphometrics and paleoneurology: brain shape evolution in the genus Homo. *Journal of Human Evolution, 47*(5), 279-303. https://www.sciencedirect.com/science/article/abs/pii/S0047248404001149?via%3Dihub

Bruner, E. (2006). From Verheyen to Bookstein: history of colobids and superimpositions. *Journal of Anthropological Sciences, 84*, 147-160. http://www.isita-org.com/jass/Contents/2006%20vol84/Jass2006Final/10-BRUNER.pdf

Bunce, A., Norman, F., Brothers, N., & Gales, R. (2002). Long-term trends in the Australasian gannet (*Morus serrator*) population in Australia: the effect of climate change and commercial fisheries. *Marine Biology, 141*(2), 263-269. https://link.springer.com/article/10.1007/s00227-002-0838-1

Buser, T. J., Boyd, O. F., Cortés, Á., Donatelli, C. M., Kolmann, M. A., Luparell, J. L., Pfeiffenberger, J. A., Sidlauskas, B. L., & Summers, A. P. (2020). The Natural Historian's guide to the CT galaxy: step-by-step instructions for preparing and analyzing computed tomographic (CT) data using cross-platform, open access software. *Integrative Organismal Biology, 2*(1), obaa009. https://doi.org/10.1093/iob/obaa009

Cardini, A., & Elton, S. (2007). Sample size and sampling error in geometric morphometric studies of size and shape. *Zoomorphology, 126*(2), 121-134. https://doi.org/10.1007/s00435-007-0036-2

Cardini, A., Elton, S., Kovarovic, K., Strand Viđarsdóttir, U., & Polly, P. D. (2021). On the misidentification of species: sampling error in primates and other mammals using geometric morphometrics in more than 4000 individuals. *Evolutionary Biology*. https://doi.org/10.1007/s11692-021-09531-3

Cardini, A., Seetah, K., & Barker, G. (2015). How many specimens do I need? Sampling error in geometric morphometrics: testing the sensitivity of means and variances in simple randomized selection experiments. *Zoomorphology, 134*(2), 149-163. https://doi.org/10.1007/s00435-015-0253-z

Cargill, C. P., Judkins, A. G., & Weir, J. S. (2020). Distribution of little penguins (*Eudyptula minor*) along the greater Kaikōura coastline, New Zealand. *New Zealand Journal of Marine Freshwater Research*, 1-16. https://www.tandfonline.com/doi/pdf/10.1080/00288330.2020.1844766

Cavaignac, E., Savall, F., Chantalat, E., Faruch, M., Reina, N., Chiron, P., & Telmon, N. (2017). Geometric morphometric analysis reveals age-related differences in the distal femur of Europeans. *Journal of Experimental Orthopaedics, 4*(1), 21. https://doi.org/10.1186/s40634-017-0095-3

Chiappe, L. M., & Witmer, L. M. (2002). *Mesozoic birds: Above the heads of dinosaurs*. University of California Press.

Chown, S. L., Gaston, K. J., & Williams, P. H. (1998). Global patterns in species richness of pelagic seabirds: the Procellariiformes. *Ecography, 21*(4), 342-350. https://onlinelibrary.wiley.com/doi/pdf/10.1111/j.1600-0587.1998.tb00399.x

Cole, T. L., Ksepka, D. T., Mitchell, K. J., Tennyson, A. J. D., Thomas, D. B., Pan, H., Zhang, G., Rawlence, N. J., Wood, J. R., Bover, P., Bouzat, J. L., Cooper, A., Fiddaman, S. R., Hart, T., Miller, G., Ryan, P. G., Shepherd, L. D., Wilmshurst, J. M., & Waters, J. M. (2019a). Mitogenomes uncover extinct penguin taxa and reveal island formation as a key driver of speciation. *Molecular Biology and Evolution, 36*(4), 784-797. https://doi.org/10.1093/molbev/msz017

Cole, T. L., Rawlence, N. J., Dussex, N., Ellenberg, U., Houston, D. M., Mattern, T., Miskelly, C. M., Morrison, K. W., Scofield, R. P., Tennyson, A. J. D., Thompson, D. R., Wood, J. R., & Waters, J. M. (2019b). Ancient DNA of crested penguins: testing for temporal genetic shifts in the world's

most diverse penguin clade. *Molecular Phylogenetics and Evolution, 131*, 72-79. https://www.sciencedirect.com/science/article/pii/S1055790318306274

Cooke, S. B., & Terhune, C. E. (2015). Form, function, and geometric morphometrics. *The Anatomical Record, 298*(1), 5-28. https://doi.org/10.1002/ar.23065

Cooper, A., Rhymer, J., James, H. F., Olson, S. L., McIntosh, C., Sorenson, M. D., & Fleischer, R. C. (1996). Ancient DNA and island endemics. *Nature*. https://www.nature.com/articles/381484a0.pdf?origin=ppub

Creaform Inc. (2015). *An introduction to 3D scanning*. Creaform Inc. https://www.creaform3d.com/sites/default/files/assets/technological-fundamentals/ebook1_an_introduction_to_3d_scanning_en_26082014.pdf

Creaform Inc. (2020). *CREAFORM: BLOG*. https://www.creaform3d.com/blog/explore-3d-scanners-and-3d-measurement-technologies/#gref

Creaform Inc. (2021a). HandySCAN 3D BLACK laser scanner. Quebec, Canada.

Creaform Inc. (2021b). VXelements software. Version 7.0. Quebec, Canada.

Croxall, J. P., Butchart, S. H., Lascelles, B., Stattersfield, A. J., Sullivan, B., Symes, A., & Taylor, P. (2012). Seabird conservation status, threats and priority actions: a global assessment. *Bird Conservation International, 22*(1), 1-34. https://www.cambridge.org/core/journals/bird-conservation-international/article/seabird-conservation-status-threats-and-priority-actions-a-global-assessment/29944BD8AA1EED41210B777389F34952

Daboul, A., Ivanovska, T., Bülow, R., Biffar, R., & Cardini, A. (2018). Procrustes-based geometric morphometrics on MRI images: An example of inter-operator bias in 3D landmarks and its impact on big datasets. *PLoS One, 13*(5), e0197675. https://doi.org/10.1371/journal.pone.0197675

Degrange, F. J., Ksepka, D. T., & Tambussi, C. P. (2018). Redescription of the oldest crown clade penguin: cranial osteology, jaw myology, neuroanatomy, and phylogenetic affinities of Madrynornis mirandus. *Journal of Vertebrate Paleontology, 38*(2), e1445636. https://doi.org/10.1080/02724634.2018.1445636

del Hoyo, J., Elliot, A., & Sargatal, J. (1994). Handbook of the Birds of the World. Volume 1. Ostrich to Ducks. *Lynx Edicions*.

Dhoop, T., Stark, S., Olaberria, J. P., & Whitewright, J. (2020). Quantifying ship shape in archaeology: evaluating 3D geometric morphometrics. *International Journal of Nautical Archaeology, 49*(1), 49-64. https://onlinelibrary.wiley.com/doi/pdf/10.1111/1095-9270.12413

Douglass, K., Antonites, A. R., Quintana Morales, E. M., Grealy, A., Bunce, M., Bruwer, C., & Gough, C. (2018). Multi-analytical approach to zooarchaeological assemblages elucidates Late Holocene coastal lifeways in southwest Madagascar. *Quaternary International, 471*, 111-131. https://www.sciencedirect.com/science/article/pii/S1040618217305165

Dowle, M., Srinivasan, A., Gorecki, J., Chirico, M., Stetsenko, P., Short, T., Lianoglou, S., Antonyan, E., Bonsch, M., & Parsonage, H. (2019). Package 'data.table'. Extension of 'data.frame'.

Drake, A. G., Coquerelle, M., & Colombeau, G. (2015). 3D morphometric analysis of fossil canid skulls contradicts the suggested domestication of dogs during the late Paleolithic. *Scientific Reports, 5*, 8299. https://doi.org/10.1038/srep08299

Dujardin, J.-P. (2011). Modern morphometrics of medically important insects. In M. Tibayrenc (Ed.), *Genetics and Evolution of Infectious Disease* (pp. 473-501). Elsevier. https://doi.org/https://doi.org/10.1016/B978-0-12-384890-1.00016-9

Duncan, R. P., & Blackburn, T. M. (2004). Extinction and endemism in the New Zealand avifauna. *Global Ecology and Biogeography, 13*(6), 509-517. http://www.jstor.org/stable/3697456

Eda, M., Koike, H., & Higuchi, H. (2016a). Understanding prehistoric maritime adaptations in northern Japan: Indirect evidence from ancient DNA and histological observations of albatross (Aves: Diomedeidae) bones. *Quaternary International, 419*, 159-164. https://www.sciencedirect.com/science/article/pii/S1040618215006679

Eda, M., Lu, P., Kikuchi, H., Li, Z., Li, F., & Yuan, J. (2016b). Reevaluation of early Holocene chicken domestication in northern China. *Journal of Archaeological Science, 67*, 25-31. https://www.sciencedirect.com/science/article/pii/S0305440316000212

Fedorov, A., Beichel, R., Kalpathy-Cramer, J., Finet, J., Fillion-Robin, J.-C., Pujol, S., Bauer, C., Jennings, D., Fennessy, F., & Sonka, M. (2012). 3D Slicer as an image computing platform for the quantitative imaging network. *Magnetic Resonance Imaging, 30*(9), 1323-1341. https://www.sciencedirect.com/science/article/pii/S0730725X12001816

Fernández de la Ossa, M. Á., Amigo, J. M., & García-Ruiz, C. (2014). Detection of residues from explosive manipulation by near infrared hyperspectral imaging: A promising forensic tool. *Forensic Science International, 242*, 228-235. https://www.sciencedirect.com/science/article/pii/S037907381400259X

Fischer, J. (2016). *Ecology, taxonomic status, and conservation of the South Georgian diving petrel (Pelecanoides georgicus) in New Zealand*. [unpublished master's thesis]. Victoria University of Wellington.

Fisher, R. A. (1936). The use of multiple measurements in taxonomic problems. *Annals of Eugenics, 7*(2), 179-188. https://onlinelibrary.wiley.com/doi/abs/10.1111/j.1469-1809.1936.tb02137.x

Forest & Bird. (2018). *Forest & Bird: Te Reo o te Taiao Giving Nature a Voice*. https://www.forestandbird.org.nz/resources/important-bird-areas-new-zealand-seabirds

Geng, J. (2011). Structured-light 3D surface imaging: a tutorial. *Advances in Optics and Photonics, 3*(2), 128-160. https://doi.org/10.1364/aop.3.000128

Gill, B., Bell, B. D., Chambers, G., Medway, D. G., Palma, R., Scofield, R., Tennyson, A., & Worthy, T. (2010). *Checklist of the Birds of New Zealand, Norfolk and Macquarie Islands, and the Ross Dependency, Antarctica, 4th edn*. Te Papa Press Ornithological Society of New Zealand.

Gill, B. J. (2006). Birds in Australian and New Zealand museums—a major resource for ornithology. *New Zealand Journal of Zoology, 33*(4), 299-315. https://doi.org/10.1080/03014223.2006.9518458

Gill, F., Donsker, D., & Rasmussen, P. (2021). *IOC World Bird List: Version 11.1.* IOC World Bird List. https://www.worldbirdnames.org/new/

Goodman, S. M., Raherilalao, M. J., & Muldoon, K. (2013). Bird fossils from Ankilitelo Cave: inference about Holocene environmental changes in Southwestern Madagasca. *Zootaxa, 3750*(5), 534-548. https://www.mapress.com/j/zt/article/view/zootaxa.3750.5.6/30985

Gould, F. D. H. (2014). To 3D or not to 3D, that is the question: Do 3D surface analyses improve the ecomorphological power of the distal femur in placental mammals? *PLoS One, 9*(3), e91719. https://doi.org/10.1371/journal.pone.0091719

Gower, J. C. (1975). Generalized Procrustes analysis. *Psychometrika, 40*(1), 33-51. https://link.springer.com/content/pdf/10.1007/BF02291478.pdf

Grealy, A., Rawlence, N. J., & Bunce, M. (2017). Time to spread your wings: a review of the avian ancient DNA field. *Genes, 8*(7), 184. https://www.mdpi.com/2073-4425/8/7/184

Gunnell, G. F., Boyer, D. M., Friscia, A. R., Heritage, S., Manthi, F. K., Miller, E. R., Sallam, H. M., Simmons, N. B., Stevens, N. J., & Seiffert, E. R. (2018). Fossil lemurs from Egypt and Kenya suggest an African origin for Madagascar's aye-aye. *Nature Communications, 9*(1), 3193. https://doi.org/10.1038/s41467-018-05648-w

Hanot, P., Guintard, C., Lepetz, S., & Cornette, R. (2017). Identifying domestic horses, donkeys and hybrids from archaeological deposits: A 3D morphological investigation on skeletons. *Journal of Archaeological Science, 78*, 88-98. https://www.sciencedirect.com/science/article/pii/S0305440316301844

Henderson, N., & Gill, B. J. (2010). A mid-Pliocene shearwater skull (Aves: Procellariidae: *Puffinus*) from the Taihape Mudstone, central North Island, New Zealand. *New Zealand Journal of Geology and Geophysics, 53*(4), 327-332. https://doi.org/10.1080/00288306.2010.505944

Hipsley, C. A., Aguilar, R., Black, J. R., & Hocknull, S. A. (2020). High-throughput microCT scanning of small specimens: preparation, packing, parameters and post-processing. *Scientific Reports, 10*(1), 1-10. https://www.nature.com/articles/s41598-020-70970-7

Hoffmeister, M. C. (2014). Phylogenetic characters in the humerus and tarsometatarsus of penguins. *Polish Polar Research*, 469-496. https://journals.pan.pl/Content/99586/PDF/10183_Volume35_Issue3_02_paper.pdf

Holdaway, R. (1989). New Zealand's pre-human avifauna and its vulnerability. *New Zealand Journal of Ecology*, 11-25. https://www.jstor.org/stable/24053244?seq=1#metadata_info_tab_contents

Horn, I. R., Kenens, Y., Palmblad, N. M., van der Plas-Duivesteijn, S. J., Langeveld, B. W., Meijer, H. J. M., Dalebout, H., Marissen, R. J., Fischer, A., Vincent Florens, F. B., Niemann, J., Rijsdijk, K. F., Schulp, A. S., Laros, J. F. J., & Gravendeel, B. (2019). Palaeoproteomics of bird bones for taxonomic classification. *Zoological Journal of the Linnean Society, 186*(3), 650-665. https://doi.org/10.1093/zoolinnean/zlz012

Höskuldsson, A. (1988). PLS regression methods. *Journal of Chemometrics, 2*(3), 211-228. https://doi.org/https://doi.org/10.1002/cem.1180020306

HP Inc. (2009). DAVID 3 software. Version 3.10.4.4657. CA, USA.

IUCN. (2021). *The IUCN Red List of Threatened Species. Version 2020-3*. https://www.iucnredlist.org. Downloaded on 31 January 2021

Jensen, R. J. (2003). The conundrum of morphometrics. *Taxon, 52*(4), 663-671.

Jouventin, P., & Dobson, F. S. (2018). In P. Jouventin & F. S. Dobson (Eds.), *Why penguins communicate* (pp. 1-43). Academic Press. https://doi.org/10.1016/B978-0-12-811178-9.00001-9

Klingenberg, C. P. (2011). MorphoJ: an integrated software package for geometric morphometrics. *Molecular Ecology Resources, 11*(2), 353-357.

Ksepka, D. T., Fordyce, R. E., Ando, T., & Jones, C. M. (2012). New fossil penguins (Aves, Sphenisciformes) from the Oligocene of New Zealand reveal the skeletal plan of stem penguins. *Journal of Vertebrate Paleontology, 32*(2), 235-254. https://doi.org/10.1080/02724634.2012.652051

Ksepka, D. T., & Thomas, D. B. (2012). Multiple Cenozoic invasions of Africa by penguins (Aves, Sphenisciformes). *Proceedings of the Royal Society B: Biological Sciences, 279*(1730), 1027-1032. https://royalsocietypublishing.org/doi/full/10.1098/rspb.2011.1592

Kuhn, M. (2008). Building predictive models in R using the caret package. *Journal of Statistical Software, 28*(5), 1-26. https://doi.org/10.18637/jss.v028.i05

Kuhn, M. (2009). The caret package. *Journal of Statistical Software, 28*(5). https://topepo.github.io/caret/

Kuhn, M. (2015). A Short Introduction to the caret Package. *R Found Stat Comput, 1*. https://cran.r-project.org/web/packages/caret/vignettes/caret.html#:~:text=The%20caret%20package%20(short%20for,complex%20regression%20and%20classification%20problems.&text=caret%20loads%20packages%20as%20needed,a%20prompt%20to%20install%20it.

Kuhn, M., & Johnson, K. (2013). *Applied predictive modeling* (Vol. 26). Springer.

Kuhn, M., Wing, J., Weston, S., Williams, A., Keefer, C., & Engelhardt, A. (2020). Caret: Classification and Regression Training; R package version 6.0-86; 2020.

Lee, L. C., Liong, C.-Y., & Jemain, A. A. (2018). Partial least squares-discriminant analysis (PLS-DA) for classification of high-dimensional (HD) data: a review of contemporary practice strategies and knowledge gaps [10.1039/C8AN00599K]. *Analyst, 143*(15), 3526-3539. https://doi.org/10.1039/C8AN00599K

Liu, W., Wang, H., Du, J., & Jing, C. (2017). Raman microspectroscopy of nucleus and cytoplasm for human colon cancer diagnosis. *Biosensors and Bioelectronics, 97*, 70-74. https://www.sciencedirect.com/science/article/pii/S0956566317303639

Livingston, S. D. (1989). The taphonomic interpretation of avian skeletal part frequencies. *Journal of Archaeological Science, 16*(5), 537-547. https://doi.org/10.1016/0305-4403(89)90072-1

Marchant, S. H., Peter J. (1990). Handbook of Australian, New Zealand & Antarctic birds. Volume 1, ratites to ducks, part A, ratites to petrels. *Oxford University Press*.

Marcy, A. E., Guillerme, T., Sherratt, E., Rowe, K. C., Phillips, M. J., & Weisbecker, V. (2020). Australian rodents reveal conserved cranial evolutionary allometry across 10 million years of murid evolution. *The American Naturalist, 196*(6), 755-768. https://doi.org/10.1086/711398

Mattern, T., Ellenberg, U., Houston, D. M., & Davis, L. S. (2007). Consistent foraging routes and benthic foraging behaviour in yellow-eyed penguins. *Marine Ecology Progress Series, 343*, 295-306. https://www.int-res.com/abstracts/meps/v343/p295-306/

Mattern, T., Rexer-Huber, K., Parker, G., Amey, J., Green, C.-P., Tennyson, A. J., Sagar, P. M., & Thompson, D. R. (2021). Erect-crested penguins on the Bounty Islands: population size and trends determined from ground counts and drone surveys. *Notornis, 68*(1), 37-50. https://notornis.osnz.org.nz/system/files/Marttern_68_etal_37-50.v2.pdf

Mayr, G., & Smith, T. (2012). Phylogenetic affinities and taxonomy of the Oligocene Diomedeoididae, and the basal divergences amongst extant procellariiform birds. *Zoological Journal of the Linnean Society, 166*(4), 854-875. https://doi.org/10.1111/j.1096-3642.2012.00858.x

Mayr, G., & Tennyson, A. J. D. (2020, 2020). A small, narrow-beaked albatross from the Pliocene of New Zealand demonstrates a higher past diversity in the feeding ecology of the Diomedeidae. *Ibis, 162*(3), 723-734. https://doi.org/10.1111/ibi.12757

Mevik, B., Wehrens, R., & Hovde Liland, K. (2020). pls: Partial Least Squares and Principal Component Regression. R package version 2.7-3.

Miskelly, C. M., Dowding, J. E., Elliott, G. P., Hitchmough, R. A., Powlesland, R. G., Robertson, H. A., Sagar, P. M., Scofield, R. P., & Taylor, G. A. (2008). Conservation status of New Zealand birds, 2008. *Notornis, 55*(3), 117-135. https://notornis.osnz.org.nz/system/files/Notornis_55_3_117.pdf

Mitchell, K. J., Wood, J. R., Scofield, R. P., Llamas, B., & Cooper, A. (2014). Ancient mitochondrial genome reveals unsuspected taxonomic affinity of the extinct Chatham duck (*Pachyanas chathamica*) and resolves divergence times for New Zealand and sub-Antarctic brown teals. *Molecular Phylogenetics and Evolution, 70*, 420-428. https://www.sciencedirect.com/science/article/pii/S1055790313003394

Newton, A. H., Weisbecker, V., Pask, A. J., & Hipsley, C. A. (2021). Ontogenetic origins of cranial convergence between the extinct marsupial thylacine and placental gray wolf. *Communications Biology, 4*(1), 51. https://doi.org/10.1038/s42003-020-01569-x

Niven, L., Steele, T. E., Finke, H., Gernat, T., & Hublin, J.-J. (2009). Virtual skeletons: using a structured light scanner to create a 3D faunal comparative collection. *Journal of Archaeological Science, 36*(9), 2018-2023. https://doi.org/https://doi.org/10.1016/j.jas.2009.05.021

Oliveri, P., Malegori, C., & Casale, M. (2018). Multivariate classification techniques. In *Encyclopedia of Analytical Science, Reference Module in Chemistry, Molecular Sciences and Chemical Engineering*. Elsevier.

Plate, T., Heiberger, R., & Plate, M. T. (2016). abind: Combine Multidimensional arrays. R package version 1.4-5.

Pomidor, B. J., Makedonska, J., & Slice, D. E. (2016). A landmark-free method for three-dimensional shape analysis. *PLoS One, 11*(3), e0150368. https://doi.org/10.1371/journal.pone.0150368

Puckett, E. E., Sherratt, E., Combs, M., Carlen, E. J., Harcourt-Smith, W., & Munshi-South, J. (2020). Variation in brown rat cranial shape shows directional selection over 120 years in New York City. *Ecology and Evolution*. https://onlinelibrary.wiley.com/doi/pdf/10.1002/ece3.6228

R Core Team. (2020). R: A language and environment for statistical computing. (Version 4.0.2). R Foundation for Statistical Computing, Vienna, Austria.

R Team. (2019). RStudio: Integrated Development Environment for R. (Version 1.2.1335). RStudio, Inc.

Randau, M., Cuff, A. R., Hutchinson, J. R., Pierce, S. E., Goswami, A., & Evolution. (2017). Regional differentiation of felid vertebral column evolution: a study of 3D shape trajectories. *Organisms Diversity & Evolution, 17*(1), 305-319. https://link.springer.com/content/pdf/10.1007/s13127-016-0304-4.pdf

RangeVision. (2021). *How to choose the right 3D scanner* https://rangevision.com/upload/Electronic-book/How%20to%20choose%20the%20right%203D%20scanner.pdf

Rawlence, N. J., Kardamaki, A., Easton, L. J., Tennyson, A. J. D., Scofield, R. P., & Waters, J. M. (2017a). Ancient DNA and morphometric analysis reveal extinction and replacement of New Zealand's unique black swans. *Proceedings of the Royal Society B: Biological Sciences, 284*(1859), 20170876. https://doi.org/10.1098/rspb.2017.0876

Rawlence, N. J., Metcalf, J. L., Wood, J. R., Worthy, T. H., Austin, J. J., & Cooper, A. (2012). The effect of climate and environmental change on the megafaunal moa of New Zealand in the absence of humans. *Quaternary Science Reviews, 50*, 141-153. https://www.sciencedirect.com/science/article/pii/S0277379112002636

Rawlence, N. J., Perry, G. L. W., Smith, I. W. G., Scofield, R. P., Tennyson, A. J. D., Matisoo-Smith, E. A., Boessenkool, S., Austin, J. J., & Waters, J. M. (2015). Radiocarbon-dating and ancient DNA reveal rapid replacement of extinct prehistoric penguins. *Quaternary Science Reviews, 112*, 59-65. https://www.sciencedirect.com/science/article/pii/S0277379115000359

Rawlence, N. J., Till, C. E., Easton, L. J., Spencer, H. G., Schuckard, R., Melville, D. S., Scofield, R. P., Tennyson, A. J. D., Rayner, M. J., Waters, J. M., & Kennedy, M. (2017b). Speciation, range contraction and extinction in the endemic New Zealand King shag complex. *Molecular Phylogenetics and Evolution, 115*, 197-209. https://www.sciencedirect.com/science/article/pii/S105579031630389X

Rawlence, N. J., Wood, J. R., Bocherens, H., & Rogers, K. M. (2016). Dietary interpretations for extinct megafauna using coprolites, intestinal contents and stable isotopes: complimentary or contradictory? *Quaternary Science Reviews, 142*, 173-178. https://www.sciencedirect.com/science/article/pii/S0277379116301548

Robertson, H. A., Dowding, J. E., Elliott, G., Hitchmough, R., Miskelly, C., O'Donnell, C. F., Powlesland, R., Sagar, P. M., Scofield, R. P., & Taylor, G. A. (2016). *Conservation status of New Zealand birds, 2016* (0478226624). https://www.doc.govt.nz/documents/science-and-technical/nztcs19entire.pdf

Rohlf, F. J., & Marcus, L. F. (1993). A revolution morphometrics. *Trends in Ecology & Evolution, 8*(4), 129-132. https://www.sciencedirect.com/science/article/pii/016953479390024J

Rohlf, F. J., & Slice, D. (1990). Extensions of the Procrustes method for the optimal superimposition of landmarks. *Systematic Biology, 39*(1), 40-59. https://doi.org/10.2307/2992207

Rueden, C. T., Schindelin, J., Hiner, M. C., DeZonia, B. E., Walter, A. E., Arena, E. T., & Eliceiri, K. W. (2017). ImageJ2: ImageJ for the next generation of scientific image data. *BMC Bioinformatics, 18*(1), 1-26. https://link.springer.com/article/10.1186/s12859-017-1934-z

Sagar, P. M., Tennyson, A. J., & Scofield, R. P. (2001). Birds of the Snares Islands, New Zealand. *Notornis, 48*, 1-40. https://notornis.osnz.org.nz/system/files/Notornis_48_1_1.pdf

Sattlecker, M., Stone, N., & Bessant, C. (2014). Current trends in machine-learning methods applied to spectroscopic cancer diagnosis. *Trends in Analytical Chemistry, 59*, 17-25. https://www.sciencedirect.com/science/article/pii/S016599361400079X

Schindelin, J., Arganda-Carreras, I., Frise, E., Kaynig, V., Longair, M., Pietzsch, T., Preibisch, S., Rueden, C., Saalfeld, S., Schmid, B., Tinevez, J.-Y., White, D. J., Hartenstein, V., Eliceiri, K., Tomancak, P., & Cardona, A. (2012). Fiji: an open-source platform for biological-image analysis. *Nature Methods, 9*(7), 676-682. https://doi.org/10.1038/nmeth.2019

Schlager, S. (2017). Morpho and Rvcg–Shape Analysis in R: R-Packages for geometric morphometrics, shape analysis and surface manipulations. In *Statistical shape and deformation analysis* (pp. 217-256). Elsevier.

Schneider, C. A., Rasband, W. S., & Eliceiri, K. W. (2012). NIH Image to ImageJ: 25 years of image analysis. *Nature Methods, 9*(7), 671-675. https://www.ncbi.nlm.nih.gov/pmc/articles/PMC5554542/

Seersholm, F. V., Cole, T. L., Grealy, A., Rawlence, N. J., Greig, K., Knapp, M., Stat, M., Hansen, A. J., Easton, L. J., & Shepherd, L. (2018). Subsistence practices, past biodiversity, and anthropogenic impacts revealed by New Zealand-wide ancient DNA survey. *Proceedings of the National Academy of Sciences, 115*(30), 7771-7776. https://www.pnas.org/content/115/30/7771

Serrano-Cinca, C., & Gutiérrez-Nieto, B. (2013). Partial least square discriminant analysis for bankruptcy prediction. *Decision Support Systems, 54*(3), 1245-1255. https://www.sciencedirect.com/science/article/pii/S0167923612003478

Sghaier, A., Ben Jabeur, S., & Bannour, B. (2018). Using partial least square discriminant analysis to distinguish between Islamic and conventional banks in the MENA region. *Review of Financial Economics, 36*(2), 133-148. https://doi.org/10.1002/rfe.1018

Siegel, A. F., & Benson, R. H. (1982). A robust comparison of biological shapes. *Biometrics, 38*(2), 341-350. http://www.jstor.org/stable/2530448

Skyscan NV. (2011). NRecon User Manual. Bruker microCT. Kontich, Belgium. https://umanitoba.ca/faculties/health_sciences/medicine/units/cacs/sam/media/NReconUserManual.pdf

Slack, K. E., Jones, C. M., Ando, T., Harrison, G. L., Fordyce, R. E., Arnason, U., & Penny, D. (2006). Early penguin fossils, plus mitochondrial genomes, calibrate avian evolution. *Molecular Biology and Evolution, 23*(6), 1144-1155. https://doi.org/10.1093/molbev/msj124

Smith, N. A., & Clarke, J. A. (2011). An alphataxonomic revision of extinct and extant razorbills (Aves, Alcidae): a combined morphometric and phylogenetic approach. *Ornithological Monographs, 72*(1), 1-61. https://www.jstor.org/stable/10.1525/om.2011.72.1.1?seq=1#metadata_info_tab_contents

Stayton, C. T., & Ruta, M. (2006). Geometric morphometrics of the skull roof of stereospondyls (Amphibia: Temnospondyli). *Palaeontology, 49*(2), 307-337. https://onlinelibrary.wiley.com/doi/abs/10.1111/j.1475-4983.2006.00523.x

Stidworthy, M. F., & Denk, D. (2018). In K. A. Terio, D. McAloose, & J. S. Leger (Eds.), *Pathology of Wildlife and Zoo Animals* (pp. 653-686). Academic Press. https://doi.org/10.1016/B978-0-12-805306-5.00027-4

Taylor, G. A. (2000). Action plan for seabird conservation in New Zealand. *Department of Conservation, Wellington, NZ.*

Tennyson, A., & Mannering, A. (2018). A new species of Pliocene shearwater (Aves: Procellariidae) from New Zealand. *Tuhinga, 29*, 1-19. https://www.tepapa.govt.nz/sites/default/files/tuhinga29_1-shearwater.pdf

Tennyson, A. J. (2010). The origin and history of New Zealand's terrestrial vertebrates. *New Zealand Journal of Ecology, 34*(1), 6. https://www.researchgate.net/profile/Alan_Tennyson/publication/281253499_The_origin_and_history_of_New_Zealand's_terrestrial_vertebrates/links/5653b6be08ae4988a7afc130.pdf

Tennyson, A. J., Cooper, J. H., & Shepherd, L. D. (2015). A new species of extinct *Pterodroma* petrel (Procellariiformes: Procellariidae) from the Chatham Islands, New Zealand. *Bulletin of the British Ornithologists' Club, 135*, 267-276. https://boc-online.org/bulletins/downloads/BBOC1353-Tennyson.pdf

Tennyson, A. J. D., & Martinson, P. (2006). *Extinct birds of New Zealand*. Te Papa Press.

Thomas, D. B., Hiscox, J. D., Dixon, B. J., & Potgieter, J. (2016). 3D scanning and printing skeletal tissues for anatomy education. *Journal of Anatomy, 229*(3), 473-481. https://onlinelibrary.wiley.com/doi/full/10.1111/joa.12484

Thomas, D. B., Ksepka, D. T., Holvast, E. J., Tennyson, A. J. D., & Scofield, P. (2020a). Re-evaluating New Zealand's endemic Pliocene penguin genus. *New Zealand Journal of Geology and Geophysics, 63*(3), 324-330. https://doi.org/10.1080/00288306.2019.1699583

Thomas, D. B., Tennyson, A. J. D., Scofield, R. P., Heath, T. A., Pett, W., & Ksepka, D. T. (2020b). Ancient crested penguin constrains timing of recruitment into seabird hotspot. *Proceedings of the Royal Society B: Biological Sciences, 287*(1932), 20201497. https://doi.org/10.1098/rspb.2020.1497

Tobias, R. D. (1995). An introduction to partial least squares regression. Proceedings of the twentieth annual SAS users group international conference, Cary.

Tocheri, M. W. (2009). Laser scanning: 3D analysis of biological surfaces. In *Advanced Imaging in Biology and Medicine* (pp. 85-101). Springer.

Tocheri, M. W., Razdan, A., Williams, R. C., & Marzke, M. W. (2005). A 3D quantitative comparison of trapezium and trapezoid relative articular and nonarticular surface areas in modern humans and great apes. *Journal of Human Evolution, 49*(5), 570-586. https://doi.org/https://doi.org/10.1016/j.jhevol.2005.06.005

Tokita, M., Yano, W., James, H. F., & Abzhanov, A. (2017). Cranial shape evolution in adaptive radiations of birds: comparative morphometrics of Darwin's finches and Hawaiian honeycreepers. *Philosophical Transactions of the Royal Society B: Biological Sciences, 372*(1713), 20150481. https://royalsocietypublishing.org/doi/pdf/10.1098/rstb.2015.0481

Vermeersch, P. M., Linseele, V., Marinova, E., Van Neer, W., Moeyersons, J., & Rethemeyer, J. (2015). Early and middle Holocene human occupation of the Egyptian eastern desert: Sodmein cave. *African Archaeological Review, 32*(3), 465-503. https://link.springer.com/article/10.1007/s10437-015-9195-6

Vermeesch, P., & Garzanti, E. (2015). Making geological sense of 'Big Data' in sedimentary provenance analysis. *Chemical Geology, 409*, 20-27. https://www.sciencedirect.com/science/article/pii/S0009254115002387

Watanabe, J., Matsuoka, H., & Hasegawa, Y. (2018). Pleistocene seabirds from Shiriya, northeast Japan: systematics and oceanographic context. *Historical Biology, 32*(5), 671-729. https://www.tandfonline.com/doi/10.1080/08912963.2018.1529764

Weber, G. W., Schäfer, K., Prossinger, H., Gunz, P., Mitteröcker, P., Seidler, H., & Science, A. H. (2001). Virtual anthropology: the digital evolution in anthropological sciences. *Journal of Physiological Anthropology, 20*(2), 69-80. https://www.jstage.jst.go.jp/article/jpa/20/2/20_2_69/_pdf

Webster, M., & Sheets, H. D. (2010). A practical introduction to landmark-based geometric morphometrics. *The Paleontological Society Papers, 16*, 163-188. https://geosci.uchicago.edu/~mwebster/Webster_and_Sheets_2010.pdf

Wehrens, R., & Mevik, B.-H. (2007). The pls package: principal component and partial least squares regression in R.

Wiley, D. F., Amenta, N., Alcantara, D. A., Ghosh, D., Kil, Y. J., Delson, E., Harcourt-Smith, W., Rohlf, F. J., St. John, K., & Hamann, B. (2005). Evolutionary morphing. IEEE Conference on Visualization 2005 (VIS'05), pp.55, Minneapolis, MN, USA.

Wold, S., Sjöström, M., & Eriksson, L. (2001). PLS-regression: a basic tool of chemometrics. *Chemometrics and Intelligent Laboratory Systems, 58*(2), 109-130. https://doi.org/https://doi.org/10.1016/S0169-7439(01)00155-1

Wood, J. R. (2016). Spatial distribution of late Holocene bird bones in the Mason Bay dune system, Stewart Island, New Zealand. *Journal of the Royal Society of New Zealand, 46*(2), 103-116. https://doi.org/10.1080/03036758.2016.1149497

Wood, J. R., Rawlence, N. J., Rogers, G. M., Austin, J. J., Worthy, T. H., & Cooper, A. (2008). Coprolite deposits reveal the diet and ecology of the extinct New Zealand megaherbivore moa (Aves, Dinornithiformes). *Quaternary Science Reviews, 27*(27), 2593-2602. https://www.sciencedirect.com/science/article/pii/S0277379108002631

Wood, J. R., Scofield, R. P., Hamel, J., Lalas, C., & Wilmshurst, J. M. (2017). Bone stable isotopes indicate a high trophic position for New Zealand's extinct South Island adzebill (*Aptornis defossor*) (Gruiformes: Aptornithidae). *New Zealand Journal of Ecology, 41*(2), 240-244. http://www.jstor.org/stable/26198805

Worthy, T. H., De Pietri, V. L., & Scofield, R. P. (2017). Recent advances in avian palaeobiology in New Zealand with implications for understanding New Zealand's geological, climatic and evolutionary histories. *New Zealand Journal of Zoology, 44*(3), 177-211. https://doi.org/10.1080/03014223.2017.1307235

Worthy, T. H., & Holdaway, R. N. (2002). *The lost world of the moa: prehistoric life of New Zealand*. Indiana University Press.

Worthy, T. H., & Scofield, R. P. (2012). Twenty-first century advances in knowledge of the biology of moa (Aves: Dinornithiformes): a new morphological analysis and moa diagnoses revised. *New Zealand Journal of Zoology, 39*(2), 87-153. https://doi.org/10.1080/03014223.2012.665060

Worthy, T. H., Tennyson, A. J., Jones, C., McNamara, J. A., & Douglas, B. J. (2007). Miocene waterfowl and other birds from Central Otago, New Zealand. *Journal of Systematic Palaeontology, 5*(1), 1-39. https://www.tandfonline.com/doi/pdf/10.1017/S1477201906001957

Wu, L., Du, B., Vander Heyden, Y., Chen, L., Zhao, L., Wang, M., & Xue, X. (2017). Recent advancements in detecting sugar-based adulterants in honey – a challenge. *Trends in Analytical Chemistry, 86*, 25-38. https://www.sciencedirect.com/science/article/pii/S0165993616300954

Yravedra, J., Aramendi, J., Maté-González, M. Á., Austin Courtenay, L., & González-Aguilera, D. (2018). Differentiating percussion pits and carnivore tooth pits using 3D reconstructions and geometric morphometrics. *PLoS One, 13*(3), e0194324. https://doi.org/10.1371/journal.pone.0194324

Yuri, T., Kimball, R. T., Harshman, J., Bowie, R. C., Braun, M. J., Chojnowski, J. L., Han, K.-L., Hackett, S. J., Huddleston, C. J., & Moore, W. S. (2013). Parsimony and model-based analyses of indels in avian nuclear genes reveal congruent and incongruent phylogenetic signals. *Biology, 2*(1), 419-444. https://doi.org/10.3390/biology2010419

Zeder, M. A., & Lapham, H. A. (2010). Assessing the reliability of criteria used to identify postcranial bones in sheep, Ovis, and goats, *Capra*. *Journal of Archaeological Science, 37*(11), 2887-2905. https://www.sciencedirect.com/science/article/pii/S0305440310002293

Zeder, M. A., & Spitzer, M. D. (2016). New insights into broad spectrum communities of the Early Holocene Near East: The birds of Hallan Çemi. *Quaternary Science Reviews, 151*, 140-159. https://doi.org/https://doi.org/10.1016/j.quascirev.2016.08.024

7 Appendices
_____

Appendix A
A.1 Landmark scheme

Fixed landmarks are discrete positions and consist of a single point (i.e. each point comprises a set of x, y, z coordinates) (Figure A.1). In the context of my work, a fixed landmark represents a homologous point for every bone in the sample. Semi-landmarks comprise several points placed along an outline such as a curve or border with a fixed landmark defining the beginning and end points of the curve. Curves included ten equally-spaced semi-landmarks which are optimally slid along the curve between these points in order for their spacing to have the least effect possible on the degree of shape difference between specimens (Webster & Sheets, 2010). Patches included 25 equally spaced (surface sliding semi-) landmarks with four fixed landmarks defining the outer boundaries and a further five fixed or semi-landmarks.

Table A.1. Definitions of landmarks.
_____

Femur fixed landmarks

s0   Most caudally-projecting point on lateral ridge of lateral condyle.

s1   Most caudally-projecting point on medial ridge of lateral condyle.

s2   Most caudally-projecting point on medial condyle.

s3   Most medially-projecting point of impression of ligamentum (lig.) collateralis medialis.

s4   Central point of fovea tendineus musculus (m.) tibialis cranialis.

s5   Most distally-projecting point on medial condyle.

s6   Most cranially-projecting point on medial condyle. Note that s6 was initially placed on specimens but subsequently removed from all analyses after it was found to be non-replicable across all specimens.

s7   Most cranially-projecting point on lateral condyle.

Femur curves

c0   Curve tracing the crista trochanteris beginning at the meeting point between the crista trochanteris and the proximal margin of the diaphysis (p01) and ending at the meeting point of the scar for the insertion of m. iliotrochantericus and the linea intermuscularis cranialis with the midpoint adjusted to follow the curve.

c1	Curve along the medial margin of the diaphysis beginning at p07 and ending at the base of the medial condyle.
c2	Curve across the caudal surface of the diaphysis connecting c1 and c3, with the first point placed centrally on the lateral margin and in line with c1, and with the midpoint placed centrally on the caudal surface to keep a straight line across the diaphysis.
c3	Curve across the cranial surface of the diaphysis connecting c1 and c2, with the midpoint placed centrally on the cranial surface to keep a straight line across the diaphysis.

Femur patch

p0	The patch encompasses the entire region of the femoral head (see p01-p09).
p01	Meeting point between the trochanter femoris and the proximal margin of the diaphysis.
p02-p04	Points scattered between p01 and p05 to trace the proximo-lateral margin of the diaphysis in both dorsal and lateral views.
p05	Meeting point between the crista trochanteris and the proximal margin of the diaphysis.
p06	Midpoint between p05 and p07, keeping the curve on the proximal margin of the diaphysis.
p07	Medial-most point of the margin between the articular surface of the femoral head and the diaphysis.
p08	Midpoint between p07 and p09, keeping the curve on the proximal margin of the diaphysis.
p09	Central point of fovea capitis.

_____
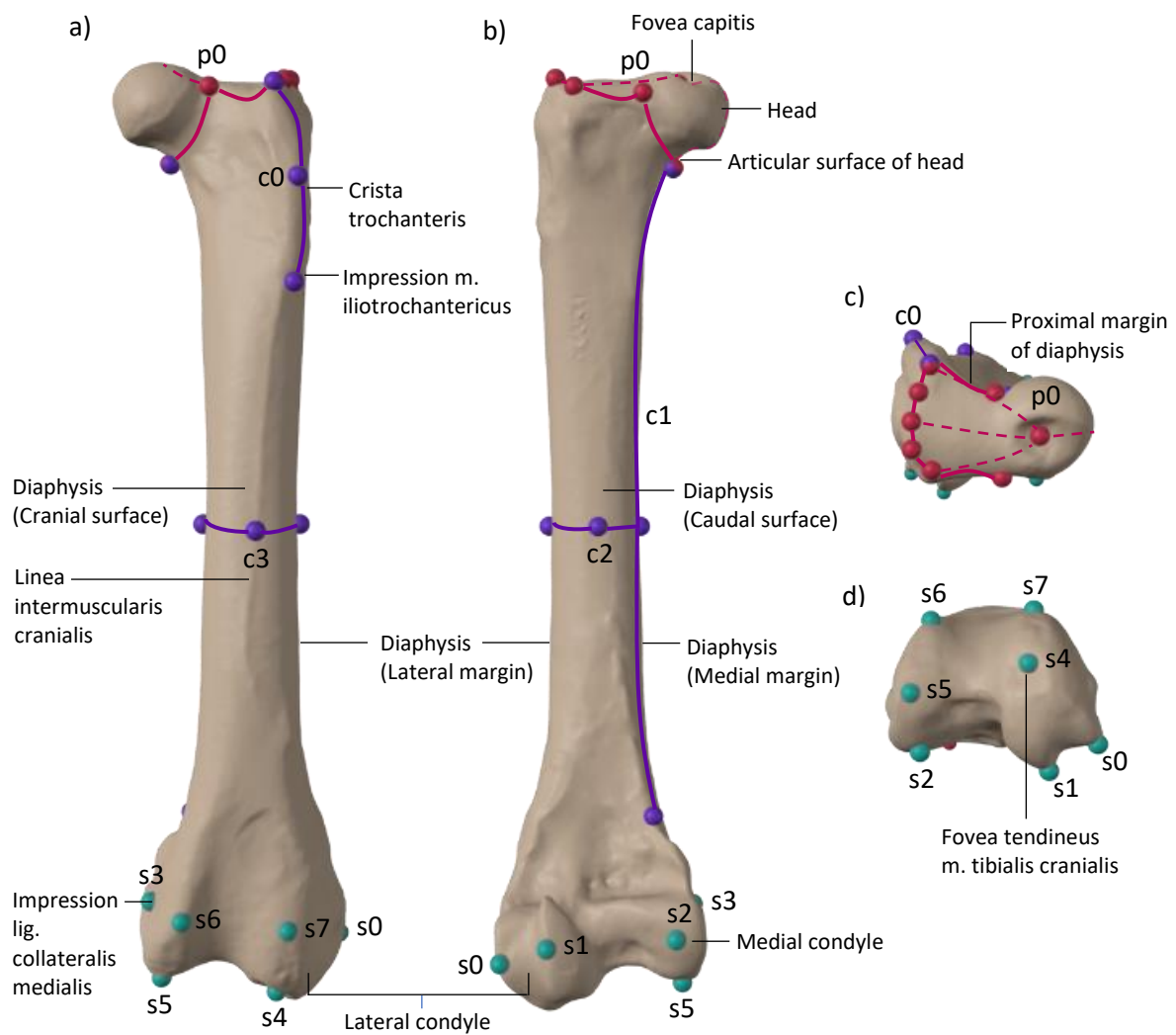
Figure A.1. Landmark positions on left femur of *Diomedea antipodensis* AM 13539 in a) cranial view, b) caudal view, and on c) proximal surface, and d) distal surface. Key: s, fixed landmark (s is default label in IDAV software) = green; c, sliding semi-landmarks (curves) = purple; p, surface sliding-semi-landmark (patch) = magenta.

Appendix B

B.1   Complete specimen list

Table B.1. Bones that were 3D scanned and analysed in 3D geometric morphometric analyses. Institution abbreviations: AM, Auckland War Memorial Museum, Auckland, New Zealand; CM, Canterbury Museum, Christchurch, New Zealand; NMNZ, Museum of New Zealand Te Papa Tongarewa, Wellington, New Zealand.

Specimen				Element		
Accession number	Family	Genus	Species	Femur	Humerus	Institution
9597	Diomedeidae	*Diomedea*	*antipodensis*	left	left	AM
13539	Diomedeidae	*Diomedea*	*antipodensis*	left	left	AM
25131	Diomedeidae	*Diomedea*	*antipodensis*	left	left	NMNZ
25212	Diomedeidae	*Diomedea*	*antipodensis*	left	right (mirrored)	NMNZ
25214	Diomedeidae	*Diomedea*	*antipodensis*	left	right (mirrored)	NMNZ
25215	Diomedeidae	*Diomedea*	*antipodensis*	left	left	NMNZ
25628a	Diomedeidae	*Diomedea*	*antipodensis*	left	left	NMNZ
25629a	Diomedeidae	*Diomedea*	*antipodensis*	left	left	NMNZ
25631	Diomedeidae	*Diomedea*	*antipodensis*	left	left	NMNZ
26744	Diomedeidae	*Diomedea*	*antipodensis*	left	left	NMNZ
27007	Diomedeidae	*Diomedea*	*antipodensis*	left	left	NMNZ
27008	Diomedeidae	*Diomedea*	*antipodensis*	left	left	NMNZ
30064	Diomedeidae	*Diomedea*	*dabbenena*	left	right (mirrored)	NMNZ
580	Diomedeidae	*Diomedea*	*epomophora* (possibly)	left	n/a	AM
DM16187	Diomedeidae	*Diomedea*	*epomophora*	left	left	NMNZ
1516	Diomedeidae	*Diomedea*	*epomophora*	left	n/a	AM
15257	Diomedeidae	*Diomedea*	*epomophora*	right (mirrored)	left	NMNZ
27589	Diomedeidae	*Diomedea*	*epomophora*	left	left	AM
DM12651	Diomedeidae	*Diomedea*	*exulans*	left	left	NMNZ
DM12652	Diomedeidae	*Diomedea*	*exulans*	left	left	NMNZ
LB14835	Diomedeidae	*Diomedea*	*exulans*	left	n/a	AM
14932	Diomedeidae	*Diomedea*	*exulans*	left	n/a	AM
15259	Diomedeidae	*Diomedea*	*exulans*	left	left	NMNZ
15258	Diomedeidae	*Diomedea*	*sanfordi*	left	left	NMNZ
30688	Diomedeidae	*Diomedea*	*sanfordi*	left	left	NMNZ
30689	Diomedeidae	*Diomedea*	*sanfordi*	left	left	NMNZ
3619	Diomedeidae	*Diomedea*	sp.	left	left	AM
013306	Diomedeidae	*Diomedea*	sp.	left	left	AM
13670	Diomedeidae	*Diomedea*	sp.	left	n/a	AM

ORO30673a	Diomedeidae	*Phoebastria*	*nigripes*	right (mirrored)	left	NMNZ
22146	Diomedeidae	*Phoebastria*	*nigripes*	left	n/a	AM
AV12743	Diomedeidae	*Phoebetria*	*palpebrata*	right (mirrored)	n/a	CM
DM17604	Diomedeidae	*Phoebetria*	*palpebrata*	left	left	NMNZ
DM17606	Diomedeidae	*Phoebetria*	*palpebrata*	left	left	NMNZ
AV13722	Diomedeidae	*Phoebetria*	*palpebrata*	left	n/a	CM
AV15304	Diomedeidae	*Phoebetria*	*palpebrata*	left	n/a	CM
AV28467	Diomedeidae	*Phoebetria*	*palpebrata*	n/a	right (mirrored)	CM
DM740s	Diomedeidae	*Phoebetria*	*palpebrata*	left	n/a	NMNZ
DM741s	Diomedeidae	*Phoebetria*	*palpebrata*	right (mirrored)	n/a	NMNZ
214	Diomedeidae	*Phoebetria*	*palpebrata*	right (mirrored)	left	AM
340	Diomedeidae	*Phoebetria*	*palpebrata*	left	left	AM
13310	Diomedeidae	*Phoebetria*	*palpebrata*	left	left	AM
14698	Diomedeidae	*Phoebetria*	*palpebrata*	left	left	AM
14810	Diomedeidae	*Phoebetria*	*palpebrata*	left	left	AM
015027	Diomedeidae	*Phoebetria*	*palpebrata*	left	n/a	AM
17605	Diomedeidae	*Phoebetria*	*palpebrata*	left	left	NMNZ
19325	Diomedeidae	*Phoebetria*	*palpebrata*	left	left	NMNZ
AV10963	Diomedeidae	*Thalassarche*	*bulleri*	left	n/a	AM
338	Diomedeidae	*Thalassarche*	*bulleri*	left	n/a	AM
24200	Diomedeidae	*Thalassarche*	*bulleri*	left	left	NMNZ
24202	Diomedeidae	*Thalassarche*	*bulleri*	left	left	NMNZ
30066	Diomedeidae	*Thalassarche*	*bulleri*	left	left	NMNZ
22417	Diomedeidae	*Thalassarche*	*carteri*	left	left	NMNZ
28477a	Diomedeidae	*Thalassarche*	*carteri*	right (mirrored)	left	NMNZ
DM14406	Diomedeidae	*Thalassarche*	*cauta*	left	left	NMNZ
DM15261	Diomedeidae	*Thalassarche*	*cauta*	left	left	NMNZ
DM15780	Diomedeidae	*Thalassarche*	*cauta*	left	left	NMNZ
558	Diomedeidae	*Thalassarche*	*cauta*	left	n/a	AM
558	Diomedeidae	*Thalassarche*	*cauta*	left	n/a	AM
012894	Diomedeidae	*Thalassarche*	*cauta salvini*	left	left	AM
AV1997	Diomedeidae	*Thalassarche*	*chlororhynchos*	left	n/a	AM
DM907	Diomedeidae	*Thalassarche*	*chrysostoma*	left	n/a	NMNZ
DM15858	Diomedeidae	*Thalassarche*	*chrysostoma*	left	left	NMNZ
DM16188	Diomedeidae	*Thalassarche*	*chrysostoma*	left	left	NMNZ
DM16461	Diomedeidae	*Thalassarche*	*chrysostoma*	left	left	NMNZ
ORO29649	Diomedeidae	*Thalassarche*	*chrysostoma*	left	left	NMNZ
198	Diomedeidae	*Thalassarche*	*chrysostoma*	left	left	AM
199	Diomedeidae	*Thalassarche*	*chrysostoma*	right (mirrored)	left	AM
350	Diomedeidae	*Thalassarche*	*chrysostoma*	left	left	AM

16459	Diomedeidae	*Thalassarche*	*chrysostoma*	left	left	NMNZ
16459	Diomedeidae	*Thalassarche*	*chrysostoma*	left	left	NMNZ
24196	Diomedeidae	*Thalassarche*	*chrysostoma*	left	left	NMNZ
17252	Diomedeidae	*Thalassarche*	*eremita*	left	left	NMNZ
26352	Diomedeidae	*Thalassarche*	*eremita*	left	left	NMNZ
26353	Diomedeidae	*Thalassarche*	*eremita*	left	left	NMNZ
26954	Diomedeidae	*Thalassarche*	*eremita*	n/a	right (mirrored)	NMNZ
ORO29464	Diomedeidae	*Thalassarche*	*impavida*	n/a	left	NMNZ
DM16456	Diomedeidae	*Thalassarche*	*melanophris*	left	n/a	NMNZ
333	Diomedeidae	*Thalassarche*	*melanophris*	left	n/a	AM
538	Diomedeidae	*Thalassarche*	*melanophris*	left	n/a	AM
ORO29128a	Diomedeidae	*Thalassarche*	*melanophris impavida*	n/a	left	NMNZ
26442	Diomedeidae	*Thalassarche*	*melanophris melanophris*	left	left	NMNZ
22116	Diomedeidae	*Thalassarche*	*salvini*	left	left	NMNZ
29526	Diomedeidae	*Thalassarche*	*salvini*	left	left	NMNZ
29856	Diomedeidae	*Thalassarche*	*salvini*	left	left	NMNZ
014928	Diomedeidae	*Thalassarche*	sp.	left	left	AM
24182	Diomedeidae	*Thalassarche*	*steadi*	left	left	NMNZ
29465	Diomedeidae	*Thalassarche*	*steadi*	left	left	NMNZ
24184	Diomedeidae	*Thalassarche*	*cauta steadi*	left	right (mirrored)	NMNZ
24204	Diomedeidae	*Thalassarche*	*cauta steadi*	left	left	NMNZ
LB13471	Oceanitidae	*Fregetta*	*tropica*	n/a	left	AM
13327	Oceanitidae	*Fregetta*	*tropica*	left	n/a	AM
LB14573	Oceanitidae	*Garrodia*	*nereis*	right (mirrored)	left	AM
AV5183	Oceanitidae	*Garrodia*	*nereis*	left	left	CM
7477	Oceanitidae	*Garrodia*	*nereis*	n/a	right (mirrored)	AM
13102	Oceanitidae	*Garrodia*	*nereis*	left	n/a	AM
AV22964	Oceanitidae	*Oceanites*	*oceanicus*	left	left	CM
LB676	Oceanitidae	*Oceanites*	*oceanicus*	n/a	left	AM
676	Oceanitidae	*Oceanites*	*oceanicus*	left	n/a	AM
2016-28-1	Oceanitidae	*Oceanites*	*oceanicus*	left	n/a	AM
AV22960	Oceanitidae	*Oceanites*	*oceanicus exasperatus*	right (mirrored)	n/a	CM
LB15174	Oceanitidae	*Oceanites*	sp.	right (mirrored)	left	AM
LB13699	Oceanitidae	*Pelagodroma*	*marina*	n/a	left	AM
LB14267	Oceanitidae	*Pelagodroma*	*marina*	left	n/a	AM
LB14590	Oceanitidae	*Pelagodroma*	*marina*	left	left	AM
LB15101	Oceanitidae	*Pelagodroma*	*marina*	left	left	AM
LB176	Oceanitidae	*Pelagodroma*	*marina*	left	left	AM
LB15098	Oceanitidae	*Pelagodroma*	*marina*	right (mirrored)	left	AM

AV524	Oceanitidae	*Pelagodroma*	*marina*	right (mirrored)	n/a	AM
LB9396	Oceanitidae	*Pelagodroma*	*marina*	n/a	left	AM
1366	Oceanitidae	*Pelagodroma*	*marina*	n/a	left	AM
12841	Oceanitidae	*Pelagodroma*	*marina*	left	n/a	AM
12866	Oceanitidae	*Pelagodroma*	*marina*	left	n/a	AM
13468	Oceanitidae	*Pelagodroma*	*marina*	left	n/a	AM
13966	Oceanitidae	*Pelagodroma*	*marina*	left	n/a	AM
014301	Oceanitidae	*Pelagodroma*	*marina* (possibly)	right (mirrored)	n/a	AM
AV14535	Oceanitidae	*Pelagodroma*	*marina maoriana*	left	n/a	CM
AV12757	Procellariidae	*Aphrodroma*	*brevirostris*	left	left	CM
NM21105	Procellariidae	*Aphrodroma*	*brevirostris*	left	left	NMNZ
AV25543	Procellariidae	*Aphrodroma*	*brevirostris*	left	n/a	CM
AV28171	Procellariidae	*Aphrodroma*	*brevirostris*	left	n/a	CM
NM18324	Procellariidae	*Aphrodroma*	*brevirostris*	n/a	right (mirrored)	AM
DM13604	Procellariidae	*Ardenna*	*bulleri*	left	right (mirrored)	NMNZ
NMNZ23906	Procellariidae	*Ardenna*	*bulleri*	right (mirrored)	right (mirrored)	NMNZ
26394	Procellariidae	*Ardenna*	*bulleri*	left	n/a	NMNZ
ORO30363	Procellariidae	*Ardenna*	*carneipes*	left	left	NMNZ
DM13607	Procellariidae	*Ardenna*	*carneipes*	left	left	NMNZ
DM13608	Procellariidae	*Ardenna*	*carneipes*	left	left	NMNZ
ORO29584	Procellariidae	*Ardenna*	*creatopus*	n/a	left	NMNZ
2006-48-5	Procellariidae	*Ardenna*	*creatopus*	left	n/a	CM
2006-48-4	Procellariidae	*Ardenna*	*creatopus*	left	left	CM
27756	Procellariidae	*Ardenna*	*creatopus*	left	n/a	NMNZ
LB15004	Procellariidae	*Ardenna*	*grisea*	left	left	AM
ORO29656	Procellariidae	*Ardenna*	*grisea*	right (mirrored)	right (mirrored)	NMNZ
ORO30619	Procellariidae	*Ardenna*	*grisea*	left	right (mirrored)	NMNZ
ORO30660	Procellariidae	*Ardenna*	*grisea*	left	right (mirrored)	NMNZ
LB15004	Procellariidae	*Ardenna*	*grisea*	n/a	left	AM
LB14929	Procellariidae	*Ardenna*	*grisea*	n/a	left	AM
40	Procellariidae	*Ardenna*	*grisea*	left	left	AM
2147	Procellariidae	*Ardenna*	*grisea*	left	left	AM
3676	Procellariidae	*Ardenna*	*grisea*	left	right (mirrored)	AM
10377	Procellariidae	*Ardenna*	*grisea*	left	left	AM
13889	Procellariidae	*Ardenna*	*grisea*	left	left	AM
14523	Procellariidae	*Ardenna*	*grisea*	left	right (mirrored)	AM
LB430	Procellariidae	*Ardenna*	*pacifica*	left	n/a	AM

ORO30198	Procellariidae	*Ardenna*	*pacifica*	n/a	right (mirrored)	NMNZ
ORO29471	Procellariidae	*Ardenna*	*tenuirostris*	left	left	NMNZ
DM13313	Procellariidae	*Ardenna*	*tenuirostris*	left	left	NMNZ
DM13314	Procellariidae	*Ardenna*	*tenuirostris*	left	left	NMNZ
ORO30042	Procellariidae	*Ardenna*	*tenuirostris*	left	left	NMNZ
15908	Procellariidae	*Ardenna*	*tenuirostris*	left	left	NMNZ
21102	Procellariidae	*Ardenna*	*tenuirostris*	left	left	NMNZ
2015-17-46	Procellariidae	*Calonectris*	*diomedea*	left	left	CM
22143	Procellariidae	*Calonectris*	*diomedea borealis*	right (mirrored)	right (mirrored)	NMNZ
27733	Procellariidae	*Calonectris*	*diomedea borealis*	left	left	NMNZ
ORO29195a	Procellariidae	*Calonectris*	*leucomelas*	left	left	NMNZ
AV18031	Procellariidae	*Daption*	*capense*	right (mirrored)	left	CM
LB1549	Procellariidae	*Daption*	*capense*	left	left	AM
DM12452	Procellariidae	*Fulmarus*	*glacialis*	left	left	NMNZ
NM17595	Procellariidae	*Fulmarus*	*glacialoides*	left	n/a	NMNZ
15252	Procellariidae	*Fulmarus*	*glacialoides*	Left	n/a	AM
AV142	Procellariidae	*Halobaena*	*caerula*	right (mirrored)	left	AM
AV28168	Procellariidae	*Halobaena*	*caerula*	left	left	CM
DM15010	Procellariidae	*Halobaena*	*caerula*	left	left	NMNZ
DM15011	Procellariidae	*Halobaena*	*caerula*	left	left	NMNZ
DM15012	Procellariidae	*Halobaena*	*caerula*	left	left	NMNZ
407	Procellariidae	*Halobaena*	*caerula*	n/a	left	AM
473	Procellariidae	*Halobaena*	*caerula*	n/a	right (mirrored)	AM
01438	Procellariidae	*Halobaena*	*caerula*	left	n/a	AM
13615	Procellariidae	*Halobaena*	*caerula*	left	left	AM
15927	Procellariidae	*Halobaena*	*caerula*	left	left	NMNZ
AV22997	Procellariidae	*Macronectes*	*giganteus*	right (mirrored)	left	CM
AV22997	Procellariidae	*Macronectes*	*giganteus*	right (mirrored)	left	CM
556	Procellariidae	*Macronectes*	*giganteus*	right (mirrored)	right (mirrored)	AM
561	Procellariidae	*Macronectes*	*giganteus*	left	left	AM
NM17608	Procellariidae	*Macronectes*	*giganteus* (possibly)	left	n/a	NMNZ
DM704s	Procellariidae	*Macronectes*	*halli*	left	left	NMNZ
AV28597	Procellariidae	*Macronectes*	*halli*	left	left	NMNZ
ORO30324	Procellariidae	*Macronectes*	*halli*	left	right (mirrored)	NMNZ
ORO30385	Procellariidae	*Macronectes*	*halli*	left	left	NMNZ
NMNZ23904	Procellariidae	*Pachyptila*	*belcheri*	left	left	NMNZ
LB12934	Procellariidae	*Pachyptila*	*belcheri*	left	n/a	AM
DM15921	Procellariidae	*Pachyptila*	*belcheri*	left	left	NMNZ

344	Procellariidae	*Pachyptila*	*belcheri*	left	n/a	AM
416	Procellariidae	*Pachyptila*	*belcheri*	left	n/a	AM
LB1265	Procellariidae	*Pachyptila*	*crassirostris*	left	n/a	AM
21088	Procellariidae	*Pachyptila*	*crassirostris crassirostris*	left	left	NMNZ
ORO29594	Procellariidae	*Pachyptila*	*desolata*	left	left	NMNZ
ORO29596	Procellariidae	*Pachyptila*	*desolata*	left	left	NMNZ
11610	Procellariidae	*Pachyptila*	*desolata*	left	n/a	AM
12788	Procellariidae	*Pachyptila*	*desolata*	left	n/a	AM
ORO29591	Procellariidae	*Pachyptila*	*salvini*	right (mirrored)	left	NMNZ
LB4665	Procellariidae	*Pachyptila*	*turtur*	left	n/a	AM
LB15170	Procellariidae	*Pachyptila*	*turtur*	left	n/a	AM
ORO29190	Procellariidae	*Pachyptila*	*turtur*	left	left	NMNZ
12155	Procellariidae	*Pachyptila*	*turtur*	right (mirrored)	n/a	AM
12513	Procellariidae	*Pachyptila*	*turtur*	left	n/a	AM
14300	Procellariidae	*Pachyptila*	*turtur*	left	n/a	AM
14744	Procellariidae	*Pachyptila*	*turtur*	left	n/a	AM
15173	Procellariidae	*Pachyptila*	*turtur*	left	n/a	AM
15255	Procellariidae	*Pachyptila*	*turtur*	left	n/a	AM
15259	Procellariidae	*Pachyptila*	*turtur*	left	n/a	AM
110	Procellariidae	*Pachyptila*	*vittata*	right (mirrored)	left	AM
422	Procellariidae	*Pachyptila*	*vittata*	left	left	AM
806	Procellariidae	*Pachyptila*	*vittata*	left	right (mirrored)	AM
012815	Procellariidae	*Pachyptila*	*vittata*	left	n/a	AM
14495	Procellariidae	*Pachyptila*	*vittata*	left	n/a	AM
015182	Procellariidae	*Pachyptila*	*vittata*	left	left	AM
015217	Procellariidae	*Pachyptila*	*vittata*	left	left	AM
15247	Procellariidae	*Pachyptila*	*vittata*	left	left	AM
15251	Procellariidae	*Pachyptila*	*vittata*	left	left	AM
12055	Procellariidae	*Pachyptila*	*vittata macgillivrayi*	left	n/a	AM
AV22863	Procellariidae	*Pagodroma*	*nivea*	right (mirrored)	n/a	CM
DM11946	Procellariidae	*Pagodroma*	*nivea*	left	left	NMNZ
AV22697	Procellariidae	*Pagodroma*	*nivea*	left	n/a	CM
27468	Procellariidae	*Pagodroma*	*nivea nivea*	left	left	NMNZ
AV39574	Procellariidae	*Pelecanoides*	*exsul* cf. *georgicus*	left	left	CM
ORO27549a	Procellariidae	*Pelecanoides*	*georgicus*	n/a	left	NMNZ
2006471	Procellariidae	*Pelecanoides*	*georgicus*	left	left	NMNZ
AV600	Procellariidae	*Pelecanoides*	*urinatrix*	left	n/a	AM
AV601	Procellariidae	*Pelecanoides*	*urinatrix*	left	n/a	AM
AV27281	Procellariidae	*Pelecanoides*	*urinatrix*	n/a	right (mirrored)	CM

AV27303	Procellariidae	*Pelecanoides*	*urinatrix exsul salvia*	right (mirrored)	left	CM
AV27304	Procellariidae	*Pelecanoides*	*urinatrix exsul salvia*	left	left	CM
NM18333	Procellariidae	*Procellaria*	*aequinoctialis*	left	n/a	NMNZ
DM15931	Procellariidae	*Procellaria*	*aequinoctialis*	left	left	NMNZ
AV30697	Procellariidae	*Procellaria*	*cinera*	left	left	CM
AV32401	Procellariidae	*Procellaria*	*cinera*	left	n/a	CM
24975	Procellariidae	*Procellaria*	*cinera*	left	left	NMNZ
ORO29637	Procellariidae	*Procellaria*	*parkinsoni*	left	left	NMNZ
NM18905	Procellariidae	*Procellaria*	*parkinsoni*	n/a	left	NMNZ
1625	Procellariidae	*Procellaria*	*parkinsoni*	left	left	AM
27119a	Procellariidae	*Procellaria*	*parkinsoni*	n/a	right (mirrored)	NMNZ
DM13566	Procellariidae	*Procellaria*	*westlandica*	left	left	NMNZ
23734	Procellariidae	*Procellaria*	*westlandica*	left	left	NMNZ
NMNZ23900	Procellariidae	*Pseudobulweria*	*rostrata*	n/a	left	NMNZ
22140	Procellariidae	*Pterodroma*	*arminjoniana*	left	right (mirrored)	NMNZ
24551	Procellariidae	*Pterodroma*	*axillaris*	right (mirrored)	n/a	NMNZ
24691	Procellariidae	*Pterodroma*	*axillaris*	left	left	NMNZ
25103	Procellariidae	*Pterodroma*	*axillaris*	right (mirrored)	left	NMNZ
28123a	Procellariidae	*Pterodroma*	*axillaris*	left	left	NMNZ
ORO29250	Procellariidae	*Pterodroma*	*brevipes*	right (mirrored)	n/a	NMNZ
NM24075	Procellariidae	*Pterodroma*	*cervicalis*	left	right (mirrored)	NMNZ
27496	Procellariidae	*Pterodroma*	*cervicalis*	left	left	NMNZ
23984	Procellariidae	*Pterodroma*	*cervicalis cervicalis*	left	left	NMNZ
LB458	Procellariidae	*Pterodroma*	*cookii*	left	n/a	AM
LB685	Procellariidae	*Pterodroma*	*cookii*	left	n/a	AM
LB1489	Procellariidae	*Pterodroma*	*cookii*	left	n/a	AM
LB7462	Procellariidae	*Pterodroma*	*cookii*	left	n/a	AM
LB15323	Procellariidae	*Pterodroma*	*cookii*	left	n/a	AM
255	Procellariidae	*Pterodroma*	*cookii*	right (mirrored)	n/a	AM
9755	Procellariidae	*Pterodroma*	*cookii*	left	n/a	AM
13944	Procellariidae	*Pterodroma*	*cookii*	left	n/a	AM
14721	Procellariidae	*Pterodroma*	*cookii*	left	n/a	AM
27331	Procellariidae	*Pterodroma*	*defilippiana*	left	n/a	NMNZ
27742	Procellariidae	*Pterodroma*	*defilippiana*	n/a	left	NMNZ
NM24356	Procellariidae	*Pterodroma*	*externa*	left	right (mirrored)	NMNZ
22426	Procellariidae	*Pterodroma*	*incerta*	n/a	right (mirrored)	NMNZ
DM12046	Procellariidae	*Pterodroma*	*inexpectata*	left	left	NMNZ

DM12047	Procellariidae	*Pterodroma*	*inexpectata*	left	left	NMNZ
DM13316	Procellariidae	*Pterodroma*	*inexpectata*	left	left	NMNZ
DM14984	Procellariidae	*Pterodroma*	*inexpectata*	left	left	NMNZ
369	Procellariidae	*Pterodroma*	*inexpectata*	left	left	AM
450	Procellariidae	*Pterodroma*	*inexpectata*	left	left	AM
12880	Procellariidae	*Pterodroma*	*inexpectata*	left	left	AM
013510	Procellariidae	*Pterodroma*	*inexpectata*	left	n/a	AM
13539	Procellariidae	*Pterodroma*	*inexpectata*	left	left	AM
015136	Procellariidae	*Pterodroma*	*inexpectata*	left	n/a	AM
19816	Procellariidae	*Pterodroma*	*inexpectata*	left	left	NMNZ
23459	Procellariidae	*Pterodroma*	*inexpectata*	left	left	NMNZ
28682	Procellariidae	*Pterodroma*	*inexpectata*	left	left	NMNZ
LB335	Procellariidae	*Pterodroma*	*lessonii*	left	left	AM
3740	Procellariidae	*Pterodroma*	*leucoptera*	n/a	left	AM
23141	Procellariidae	*Pterodroma*	*leucoptera caledonica*	left	left	NMNZ
NM23450	Procellariidae	*Pterodroma*	*longirostris*	left	left	NMNZ
DM23454	Procellariidae	*Pterodroma*	*longirostris*	left	left	NMNZ
27767a	Procellariidae	*Pterodroma*	*longirostris*	left	left	NMNZ
11050	Procellariidae	*Pterodroma*	*macroptera*	right (mirrored)	left	AM
15114	Procellariidae	*Pterodroma*	*macroptera*	n/a	left	AM
DM11426	Procellariidae	*Pterodroma*	*macroptera gouldi*	left	left	NMNZ
DM13605	Procellariidae	*Pterodroma*	*macroptera gouldi*	left	left	NMNZ
ORO30261	Procellariidae	*Pterodroma*	*macroptera gouldi*	left	right (mirrored)	NMNZ
13597	Procellariidae	*Pterodroma*	*macroptera gouldi*	left	left	NMNZ
21103	Procellariidae	*Pterodroma*	*macroptera gouldi*	left	left	NMNZ
25209a	Procellariidae	*Pterodroma*	*magentae*	left	left	NMNZ
NM16583a	Procellariidae	*Pterodroma*	*mollis*	left	left	NMNZ
ORO30555a	Procellariidae	*Pterodroma*	*mollis*	right (mirrored)	left	NMNZ
25195a	Procellariidae	*Pterodroma*	*mollis*	left	left	NMNZ
28008a	Procellariidae	*Pterodroma*	*mollis*	right (mirrored)	right (mirrored)	NMNZ
ORO30274	Procellariidae	*Pterodroma*	*neglecta*	right (mirrored)	left	NMNZ
28192	Procellariidae	*Pterodroma*	*neglecta*	left	left	NMNZ
28439	Procellariidae	*Pterodroma*	*neglecta*	left	left	NMNZ
28534	Procellariidae	*Pterodroma*	*neglecta*	left	left	NMNZ
LB2007	Procellariidae	*Pterodroma*	*nigripennis*	n/a	left	AM
ORO29088	Procellariidae	*Pterodroma*	*nigripennis*	n/a	right (mirrored)	NMNZ
NM22368	Procellariidae	*Pterodroma*	*phaeopygia sandwichensis*	left	right (mirrored)	NMNZ

76

LB752	Procellariidae	*Pterodroma*	*pycrofti*	left	left	AM
NM24371	Procellariidae	*Pterodroma*	*pycrofti*	left	left	NMNZ
NM24421	Procellariidae	*Pterodroma*	*pycrofti*	left	left	NMNZ
ORO29759b	Procellariidae	*Pterodroma*	*solandri*	left	left	NMNZ
ORO30288	Procellariidae	*Pterodroma*	*solandri*	left	right (mirrored)	NMNZ
28126a	Procellariidae	*Pterodroma*	*ultima*	right (mirrored)	right (mirrored)	NMNZ
26629	Procellariidae	*Puffinus*	*assimilis*	n/a	left	NMNZ
15509	Procellariidae	*Puffinus*	*assimilis elegans*	left	left	NMNZ
18912	Procellariidae	*Puffinus*	*assimilis elegans*	left	left	NMNZ
28686	Procellariidae	*Puffinus*	*assimils elegans*	left	left	NMNZ
LB9375	Procellariidae	*Puffinus*	*gavia*	right (mirrored)	right (mirrored)	AM
DM12664	Procellariidae	*Puffinus*	*gavia*	n/a	left	NMNZ
DM17257	Procellariidae	*Puffinus*	*gavia*	left	n/a	NMNZ
22144	Procellariidae	*Puffinus*	*gravis*	n/a	right (mirrored)	NMNZ
LB14496	Procellariidae	*Puffinus*	*huttoni*	n/a	left	AM
ORO30169	Procellariidae	*Puffinus*	*huttoni*	left	left	NMNZ
27570	Procellariidae	*Puffinus*	*huttoni*	left	right (mirrored)	NMNZ
NM19307	Procellariidae	*Puffinus*	*nativitis*	left	left	NMNZ
ORO30143	Procellariidae	*Puffinus*	*nativitis*	n/z	left	NMNZ
24682	Procellariidae	*Puffinus*	*nativitis*	left	left	NMNZ
22764	Procellariidae	*Puffinus*	*newelli*	right (mirrored)	right (mirrored)	NMNZ
25004	Procellariidae	*Puffinus*	*newelli*	left	n/a	NMNZ
23335	Procellariidae	*Puffinus*	*puffinus puffinus*	left	left	NMNZ
AV36020	Procellariidae	*Puffinus*	sp.	left	left	CM
OR27407	Procellariidae	*Thalassoica*	*antartica*	left	n/a	NMNZ
AV19569	Spheniscidae	*Aptenodytes*	*forsteri*	n/a	right (mirrored)	CM
NM23039	Spheniscidae	*Aptenodytes*	*forsteri*	n/a	left	NMNZ
NM29039	Spheniscidae	*Aptenodytes*	*forsteri*	left	n/a	NMNZ
AV6623	Spheniscidae	*Aptenodytes*	*patagonicus*	left	n/a	CM
20131257	Spheniscidae	*Aptenodytes*	*patagonicus*	left	right (mirrored)	CM
17176	Spheniscidae	*Eudyptes*	*pachyrhynchus*	left	n/a	NMNZ
AV5367	Spheniscidae	*Eudyptes*	*chrysocome*	left	n/a	CM
19303	Spheniscidae	*Eudyptes*	*chrysocome filholi*	left	n/a	NMNZ
DM12840	Spheniscidae	*Eudyptes*	*chrysolophus*	left	n/a	NMNZ
DM11236	Spheniscidae	*Eudyptes*	*filholi*	left	right (mirrored)	NMNZ

NM19303	Spheniscidae	*Eudyptes*	*filholi*	left	right (mirrored)	NMNZ
DM17176	Spheniscidae	*Eudyptes*	*pachyrhynchus*	left	left	NMNZ
29154	Spheniscidae	*Eudyptes*	*pachyrhynchus*	left	left	NMNZ
23746	Spheniscidae	*Eudyptes*	*robustus*	left	left	NMNZ
30196	Spheniscidae	*Eudyptes*	*robustus*	left	left	NMNZ
26959	Spheniscidae	*Eudyptes*	*schlegeli*	left	n/a	NMNZ
27787	Spheniscidae	*Eudyptes*	*schlegeli*	left	right (mirrored)	NMNZ
25560	Spheniscidae	*Eudyptes*	*sclateri*	left	right (mirrored)	NMNZ
LB1521	Spheniscidae	*Eudyptula*	*minor*	left	n/a	AM
LB1523	Spheniscidae	*Eudyptula*	*minor*	left	n/a	AM
18415	Spheniscidae	*Eudyptula*	*minor*	right (mirrored)	right (mirrored)	AM
18425	Spheniscidae	*Eudyptula*	*minor*	left	right (mirrored)	NMNZ
LB670	Spheniscidae	*Megadyptes*	*antipodes*	left	left	AM
18335	Spheniscidae	*Megadyptes*	*antipodes*	right (mirrored)	right (mirrored)	NMNZ
26794	Spheniscidae	*Megadyptes*	*antipodes*	left	right (mirrored)	NMNZ
NMNZ12033	Spheniscidae	*Pygoscelis*	*adeliae*	n/a	right (mirrored)	NMNZ
AV5134	Spheniscidae	*Pygoscelis*	*adeliae*	left	n/a	CM
AV38751	Spheniscidae	*Pygoscelis*	*adeliae*	n/a	right (mirrored)	CM
29460	Spheniscidae	*Pygoscelis*	*adeliae*	left	n/a	NMNZ
AV32995	Spheniscidae	*Pygoscelis*	*antarctica*	n/a	right (mirrored)	CM
DM13309	Spheniscidae	*Pygoscelis*	*papua*	left	n/a	NMNZ
AV38694	Spheniscidae	*Pygoscelis*	*papua*	n/a	right (mirrored)	CM
2749	Spheniscidae	*Spheniscus*	*demersus*	right (mirrored)	right (mirrored)	NMNZ
22800	Spheniscidae	*Spheniscus*	*demersus*	left	right (mirrored)	NMNZ
27239	Spheniscidae	*Spheniscus*	*magellanicus*	n/a	right (mirrored)	NMNZ
27329	Spheniscidae	*Spheniscus*	*magellanicus*	left	right (mirrored)	NMNZ

Appendix C

C.1   3D scanning equipment

a)

b)

c)
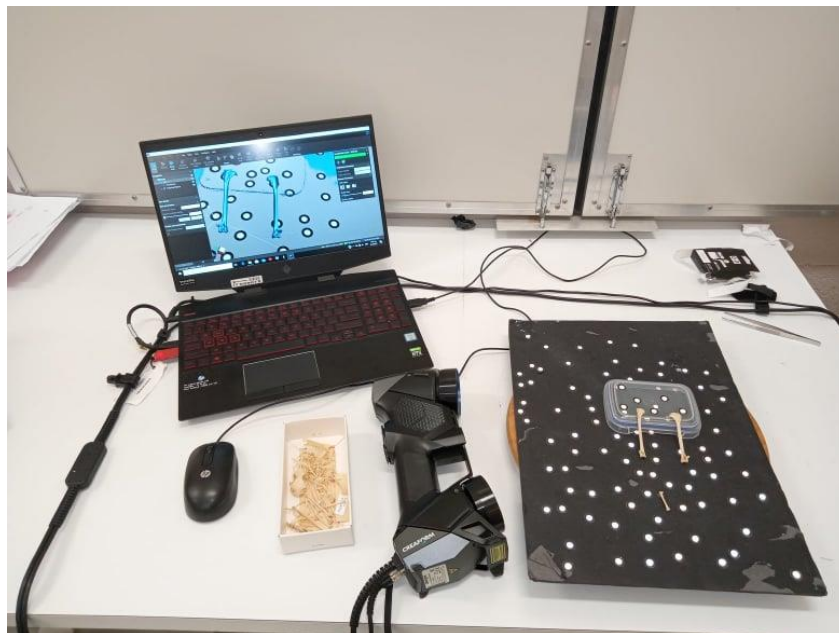
Figure C.1. HandySCAN BLACK 3D laser scanner (Creaform Inc., 2021a) used for data collection in this study. a) 3D scanning equipment, b) 3D scanner in position, c) 3D scanning setup including 3D scanner, monitor, specimen (Auckland War Memorial Museum) and board with targets.

Appendix D

D.1   microCT imaging
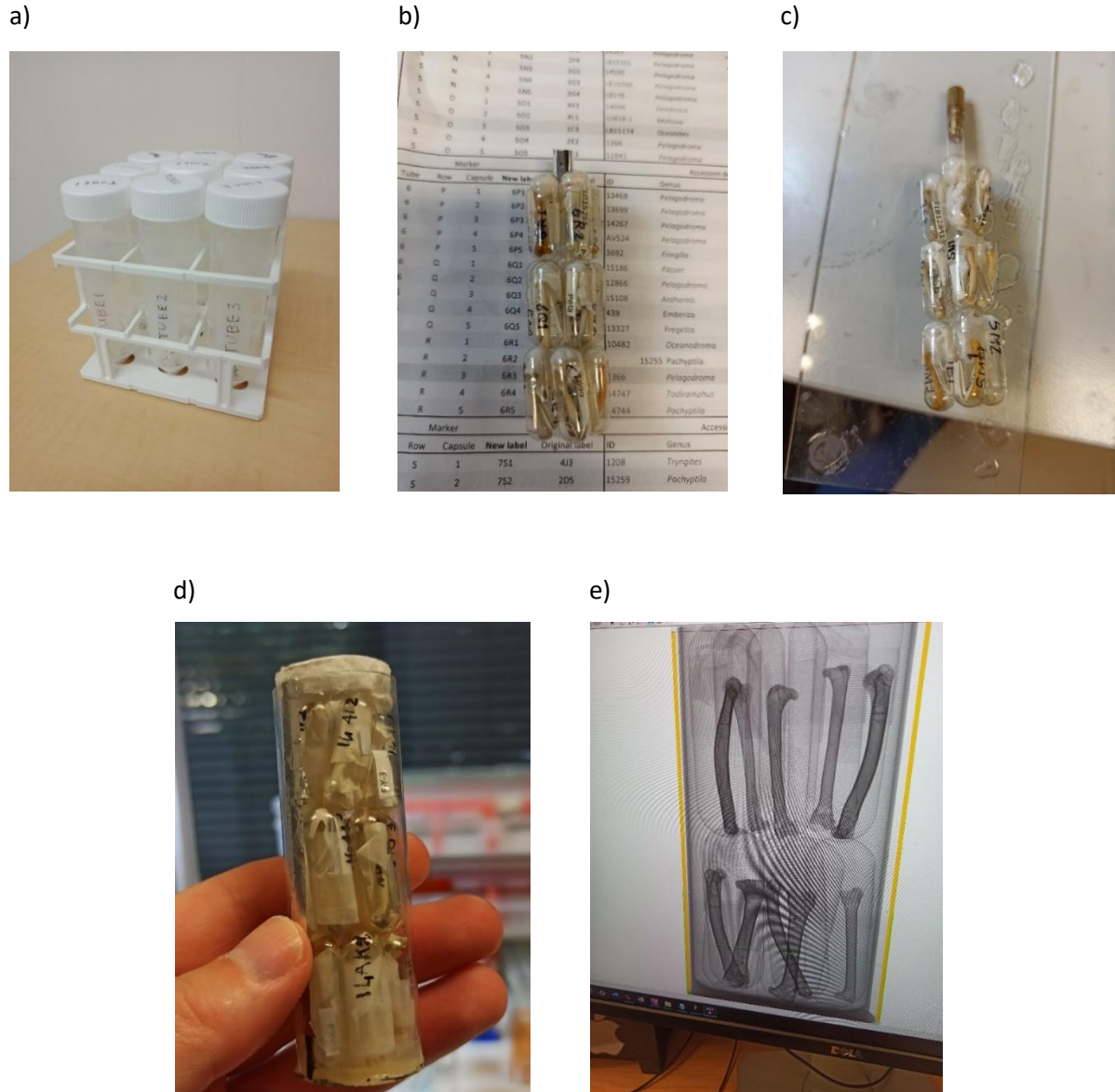
Figure D.1. MicroCT protocol for grouping and imaging multiple small bones as adapted from Hipsley et al. (2020). a) Capsules in labelled storage tubes, b) specimen holder aligned to sampling scheme showing corresponding capsule and row assignment for each bone, c) assembly of specimen holder, d) fully enclosed specimen holder ready for imaging and e) imaging window for a single scanning session with ten bones (i.e. two rows of capsules).

Appendix E

E.1   R code for landmark-based analyses

```
## Required packages ##
#install.packages("Morpho")
library(Morpho)
#install.packages("rgl")
library(rgl)
#install.packages("Rvcg")
library(Rvcg)
#install.packages("xfun")
library(xfun)
#install.packages("promises")
library(promises)
#install.packages("mime")
library(mime)
#install.packages("fastmap")
library(fastmap)
#install.packages("RRPP")
library(RRPP)
#install.packages("geomorph")
library(geomorph)
#install.packages("car")
library(car)
#install.packages("adephylo")
library(adephylo)
#install.packages("phytools")
library(phytools)
#install.packages("pls")
library(pls)
#install.packages("caret")
#install.packages("caret", dependencies = c("Depends",
"Suggests"))
library(caret)
library(e1071)
library(abind)

wd="..." #update with relevant working directory
file.list=list.files(wd,full.names=T,pattern="\\.pts$")

## Species labels ##
sp.lab=c()

for(i in 1:length(file.list)){

sp.lab[i]=paste(unlist(strsplit(list.files(wd,pattern="\\.pts$")[i],"
"))[c(2,3)],collapse=" ")
}
gen.lab.step1=gsub("_"," ",file.list)
gen.lab.step2=gsub(wd,"",gen.lab.step1)
gen.lab.step3=c()
for(i in 1:length(gen.lab.step2)){
  gen.lab.step3[i]=strsplit(gen.lab.step2," ")[[i]][2]
}

# Just species
species.list=c()
for (i in 1:length(sp.lab)){
  species.list[i]=strsplit(sp.lab," ")[[i]][2]
}

genus.lab=gen.lab.step3

family.lab=gen.lab.step3
```

```
family.lab[which(match(family.lab,c("Aptenodytes","Eudyptes",
"Eudyptula","Megadyptes","Pygoscelis","Spheniscus"),nomatch
=0)>0)]="Spheniscidae"
family.lab[which(match(family.lab,c("Diomedea","Thalassarche
","Phoebetria","Phoebastria"),nomatch=0)>0)]="Diomedeidae"
family.lab[which(match(family.lab,c("Oceanites","Garrodia","Pe
lagodroma", "Fregetta"),nomatch=0)>0)]="Oceanitidae"
family.lab[which(match(family.lab,c("Aphrodroma","Puffinus","
Ardenna","Procellaria","Macronectes","Pterodroma","Pachyptil
a","Halobaena","Calonectris","Thalassoica","Pelecanoides","Da
ption","Fulmarus","Pagodroma"),nomatch=0)>0)]="Procellariid
ae"

family.col=family.lab
family.col[which(family.lab=="Spheniscidae")]="lightseagreen"
family.col[which(family.lab=="Diomedeidae")]="darkmagenta"
family.col[which(family.lab=="Oceanitidae")]="plum1"
family.col[which(family.lab=="Procellariidae")]="violetred2"

order.lab=gen.lab.step3
order.lab[which(match(order.lab,c("Aptenodytes","Eudyptes","
Eudyptula","Megadyptes","Pygoscelis","Spheniscus"),nomatch=
0)>0)]="Sphenisciformes"
order.lab[which(match(order.lab,c("Aphrodroma","Diomedea",
"Thalassarche","Phoebetria","Phoebastria","Oceanites","Garro
dia","Pelagodroma","Fregetta","Puffinus","Ardenna","Procellari
a","Macronectes","Pterodroma","Pachyptila","Halobaena","Cal
onectris","Thalassoica","Pelecanoides","Fulmarus","Daption","
Pagodroma"),nomatch=0)>0)]="Procellariiformes"
order.col=order.lab
order.col[which(order.lab=="Sphenisciformes")]="lightseagreen
"
order.col[which(order.lab=="Procellariiformes")]="violetred2"

genus.lab=gen.lab.step3
genus.lab[which(match(genus.lab,c("Diomedea"),nomatch=0)>
0)]="Diomedea"
genus.lab[which(match(genus.lab,c("Thalassarche"),nomatch=0
)>0)]="Thalassarche"
genus.lab[which(match(genus.lab,c("Phoebastria"),nomatch=0)
>0)]="Phoebastria"
genus.lab[which(match(genus.lab,c("Phoebetria"),nomatch=0)>
0)]="Phoebetria"
genus.lab[which(match(genus.lab,c("Puffinus"),nomatch=0)>0)]
="Puffinus"
genus.lab[which(match(genus.lab,c("Ardenna"),nomatch=0)>0)
]="Ardenna"
genus.lab[which(match(genus.lab,c("Procellaria"),nomatch=0)>
0)]="Procellaria"
genus.lab[which(match(genus.lab,c("Macronectes"),nomatch=0
)>0)]="Macronectes"
genus.lab[which(match(genus.lab,c("Pterodroma"),nomatch=0)
>0)]="Pterodroma"
genus.lab[which(match(genus.lab,c("Pachyptila"),nomatch=0)>
0)]="Pachyptila"
genus.lab[which(match(genus.lab,c("Halobaena"),nomatch=0)>
0)]="Halobaena"
genus.lab[which(match(genus.lab,c("Calonectris"),nomatch=0)>
0)]="Calonectris"
genus.lab[which(match(genus.lab,c("Thalassoica"),nomatch=0)
>0)]="Thalassoica"
genus.lab[which(match(genus.lab,c("Pelecanoides"),nomatch=0
)>0)]="Pelecanoides"
```

```r
genus.lab[which(match(genus.lab,c("Daption"),nomatch=0)>0)]
="Daption"
genus.lab[which(match(genus.lab,c("Fulmarus"),nomatch=0)>0
)]="Fulmarus"
genus.lab[which(match(genus.lab,c("Pagodroma"),nomatch=0)
>0)]="Pagodroma"
genus.lab[which(match(genus.lab,c("Oceanites"),nomatch=0)>0
)]="Oceanites"
genus.lab[which(match(genus.lab,c("Garrodia"),nomatch=0)>0)
]="Garrodia"
genus.lab[which(match(genus.lab,c("Pelagodroma"),nomatch=
0)>0)]="Pelagodroma"
genus.lab[which(match(genus.lab,c("Aphrodroma"),nomatch=0
)>0)]="Aphrodroma"
genus.lab[which(match(genus.lab,c("Fregetta"),nomatch=0)>0)]
="Fregetta"
genus.lab[which(match(genus.lab,c("Eudyptula"),nomatch=0)>
0)]="Eudyptula"
genus.lab[which(match(genus,c("Eudyptes"),nomatch=0)>0)]="
Eudyptes"
genus.lab[which(match(genus,c("Pygoscelis"),nomatch=0)>0)]=
"Pygoscelis"
genus.lab[which(match(genus,c("Megadyptes"),nomatch=0)>0)
]="Megadyptes"
genus.lab[which(match(genus,c("Aptenodytes"),nomatch=0)>0)
]="Aptenodytes"
genus.lab[which(match(genus,c("Spheniscus"),nomatch=0)>0)]
="Spheniscus"
```

Plotting symbols and legend
```r
# family-level
pch.vector=rep(0,length(family.lab))
pch.vector[which(family.lab=="Spheniscidae")]=24
pch.vector[which(family.lab=="Diomedeidae")]=21
pch.vector[which(family.lab=="Oceanitidae")]=21
pch.vector[which(family.lab=="Procellariidae")]=21
pch.legend.fam=c(21,21,21,24)

cex.vector=rep(0,length(family.lab))
cex.vector[which(family.lab=="Spheniscidae")]=1.2
cex.vector[which(family.lab=="Diomedeidae")]=1.5
cex.vector[which(family.lab=="Oceanitidae")]=1.5
cex.vector[which(family.lab=="Procellariidae")]=1.5
```

Plotting symbols and legend
```r
# genus-level
pch.vector3=rep(0,length(genus.lab))
pch.vector3[which(genus.lab=="Diomedea")]=0
pch.vector3[which(genus.lab=="Thalassarche")]=22
pch.vector3[which(genus.lab=="Phoebastria")]=22
pch.vector3[which(genus.lab=="Phoebetria")]=22
pch.vector3[which(genus.lab=="Aphrodroma")]=21
pch.vector3[which(genus.lab=="Puffinus")]=21
pch.vector3[which(genus.lab=="Ardenna")]=10
pch.vector3[which(genus.lab=="Procellaria")]=21
pch.vector3[which(genus.lab=="Macronectes")]=21
pch.vector3[which(genus.lab=="Pterodroma")]=1
pch.vector3[which(genus.lab=="Pachyptila")]=21
pch.vector3[which(genus.lab=="Halobaena")]=21
pch.vector3[which(genus.lab=="Calonectris")]=21
pch.vector3[which(genus.lab=="Thalassoica")]=21
pch.vector3[which(genus.lab=="Pelecanoides")]=21
pch.vector3[which(genus.lab=="Daption")]=21
pch.vector3[which(genus.lab=="Fulmarus")]=21
pch.vector3[which(genus.lab=="Pagodroma")]=21
pch.vector3[which(genus.lab=="Oceanites")]=23
pch.vector3[which(genus.lab=="Garrodia")]=9
pch.vector3[which(genus.lab=="Pelagodroma")]=5
pch.vector3[which(genus.lab=="Fregetta")]=23
pch.vector3[which(genus.lab=="Aptenodytes")]=24
pch.vector3[which(genus.lab=="Eudyptula")]=24
```

```r
pch.vector3[which(genus.lab=="Eudyptes")]=24
pch.vector3[which(genus.lab=="Megadyptes")]=24
pch.vector3[which(genus.lab=="Pygoscelis")]=24
pch.vector3[which(genus.lab=="Spheniscus")]=24
pch.legend.gen=c(2,17,24,24,24,24,23,)

cex.vector3=rep(0,length(genus.lab))
cex.vector3[which(genus.lab=="Diomedea")]=1.4
cex.vector3[which(genus.lab=="Thalassarche")]=1.4
cex.vector3[which(genus.lab=="Phoebastria")]=1.4
cex.vector3[which(genus.lab=="Phoebetria")]=1.4
cex.vector3[which(genus.lab=="Puffinus")]=1.5
cex.vector3[which(genus.lab=="Aphrodroma")]=1.5
cex.vector3[which(genus.lab=="Ardenna")]=1.5
cex.vector3[which(genus.lab=="Procellaria")]=1.5
cex.vector3[which(genus.lab=="Macronectes")]=1.5
cex.vector3[which(genus.lab=="Pterodroma")]=1.5
cex.vector3[which(genus.lab=="Pachyptila")]=1.5
cex.vector3[which(genus.lab=="Halobaena")]=1.5
cex.vector3[which(genus.lab=="Calonectris")]=1.5
cex.vector3[which(genus.lab=="Thalassoica")]=1.5
cex.vector3[which(genus.lab=="Pelecanoides")]=1.5
cex.vector3[which(genus.lab=="Daption")]=1.5
cex.vector3[which(genus.lab=="Fulmarus")]=1.5
cex.vector3[which(genus.lab=="Pagodroma")]=1.5
cex.vector3[which(genus.lab=="Oceanites")]=1.3
cex.vector3[which(genus.lab=="Garrodia")]=1.3
cex.vector3[which(genus.lab=="Pelagodroma")]=1.3
cex.vector3[which(genus.lab=="Fregetta")]=1.3
cex.vector3[which(genus.lab=="Aptenodytes")]=1.2
cex.vector3[which(genus.lab=="Eudyptula")]=1.2
cex.vector3[which(genus.lab=="Eudyptes")]=1.2
cex.vector3[which(genus.lab=="Megadyptes")]=1.2
cex.vector3[which(genus.lab=="Pygoscelis")]=1.2
cex.vector3[which(genus.lab=="Spheniscus")]=1.2
```

Landmark PCA start
```r
LM.read=as.matrix(read.pts(file.list[1]))

#Extra landmarks to remove
landmark.rm=c("S006")
LM.rm=c()
for(i in 1:length(landmark.rm)){
  LM.x=which(substr(rownames(LM.read),0,4)==landmark.rm[i])
  LM.rm=c(LM.rm,LM.x)
}

LM.edit=LM.read
if(length(landmark.rm)>0){
  LM.edit=LM.read[-c(LM.rm),]}

LM.fixed.ID=which(substring(unlist(dimnames(LM.edit)),0,1)=="
S")
LM.curve.ID=which(substring(unlist(dimnames(LM.edit)),0,1)==
"C")
LM.patch.ID=which(substring(unlist(dimnames(LM.edit)),0,1)==
"P")

#Build the landmark matrix for further analysis
LM.matrix.all=as.matrix(LM.edit)[1:nrow(LM.edit),]
for(i in 2:length(file.list)){
  LM.read=as.matrix(read.pts(file.list[i]))
  LM.edit=LM.read

  if(length(landmark.rm)>0){
    LM.edit=LM.read[-c(LM.rm),]}

LM.matrix.all=rbind(LM.matrix.all,LM.edit[1:nrow(LM.edit),])
}
LM.all.3D=arrayspecs(unname(LM.matrix.all),nrow(LM.edit),3)
```

```
#Build input values for semi landmarks
LM.curve.count=length(which(substring(rownames(LM.read),0,
4)=="C000"))
if(LM.curve.count>0){

curves.map=c()
for(i                                                          in
((1:(length(LM.curve.ID)/LM.curve.count))*LM.curve.count)-
(LM.curve.count-1)){

m.curve=define.sliders(c(LM.curve.ID[i]:(LM.curve.ID[i]+LM.cur
ve.count-1))))
  curves.map=rbind(curves.map,m.curve)
}
}


# Procrustes calculation
LM.proc.all=gpagen(LM.all.3D,curves=curves.map,surfaces=LM.
patch.ID,ProcD=T)
LM.proc.coords=LM.proc.all$coords

##Principal component analysis
result.all=gm.prcomp(LM.proc.coords)
str(LM.proc.coords)#, axis=1, axis=2
summary(result.all)

#graphics.off()
while (rgl.cur() > 0) { rgl.close() }
eigenval=result.all$sdev^2
explained=round(eigenval/sum(eigenval) * 100, digits = 1)
morph.scores=result.all$x #pc.scores

PCx=1
PCy=4

##Screeplot
plot(explained, type = "b", pch = 16, ylab = "Explained variance
(%)", xlab = "Principal component", xlim = c(0,20))
explained
cumsum(explained)

## PCA plot ##
#order-level
plot(result.all$x[,PCx],result.all$x[,PCy],cex=cex.vector,pch=pch
.vector,font=5, xaxt='n', yaxt='n', ann=FALSE, col="black",
bg=order.col,lwd=1)

# family-level
plot(result.all$x[,PCx],result.all$x[,PCy],cex=cex.vector,pch=pch
.vector,font=5, xaxt='n', yaxt='n', ann=FALSE, col="black",
bg=family.col, lwd=1)

# genus-level
plot(result.all$x[,PCx],result.all$x[,PCy],cex=cex.vector3,pch=pc
h.vector3,font=5, xaxt='n', yaxt='n', ann=FALSE, col="black",
bg=family.col, lwd=1)

axis(1,at=c(-0.05,0.05))
axis(2,at=c(-0.05,0.05))
title(xlab=paste("Principal    component    ",   PCx,    "
(",explained[PCx],"%)",sep=""))
title(ylab=paste("Principal    component    ",   PCy,    "
(",explained[PCy],"%)",sep=""))

## Ellipses ##
# family-level
for(seabird in unique(family.lab)[-5]){
  car::dataEllipse(result.all$x[which(family.lab==seabird),PCx],
result.all$x[which(family.lab==seabird),PCy],add=T,levels=0.75,
center.pch=NULL, plot.points=F,
```

```
col=family.col[which(family.lab==seabird)][1],fill=T,fill.alpha=0.
05,ellipse.label=NULL)
}

## Loadings ##
 axis1=1
 A=LM.proc.coords
 x=two.d.array(A)
 pc.res=prcomp(x)
 k <- dim(A)[2]
 p <- dim(A)[1]
 n <- dim(A)[3]
 ref <- mshape(A)
 x <- two.d.array(A)
 pc.res <- prcomp(x)
 pcdata <- pc.res$x
 pcaxis.min.1 <- min(pcdata[, axis1])
 pcaxis.max.1 <- max(pcdata[, axis1])
 pc.min.1 <- pc.max.1 <- rep(0, dim(pcdata)[2])
 pc.min.1[axis1] <- pcaxis.min.1
 pc.max.1[axis1] <- pcaxis.max.1
 shape.min.1    <-    arrayspecs(as.matrix(pc.min.1    %*%
(t(pc.res$rotation))),p, k)[, , 1] + ref
 shape.max.1    <-    arrayspecs(as.matrix(pc.max.1    %*%
(t(pc.res$rotation))),p, k)[, , 1] + ref

 diff.a=shape.max.1[,1]-shape.min.1[,1]
 diff.b=shape.max.1[,2]-shape.min.1[,2]
 diff.c=shape.max.1[,3]-shape.min.1[,3]
 diff.h=sqrt((diff.a^2)+(diff.b^2))
 diff.g=sqrt((diff.c^2)+(diff.h^2))
 diff.min=min(diff.g)
 diff.max=max(diff.g)
 diff.minmax=(diff.g-diff.min)/(diff.max-diff.min)

 plot3d(shape.min.1,col="blue",add=T,size=6,bg="black")
 points3d(shape.max.1,col="orange",add=T,size=6)
 for(i in 1:nrow(shape.min.1)){
  x.seg=c(shape.min.1[i,1],shape.max.1[i,1])
  y.seg=c(shape.min.1[i,2],shape.max.1[i,2])
  z.seg=c(shape.min.1[i,3],shape.max.1[i,3])
  segments3d(x.seg[1:2],y.seg[1:2],z.seg[1:2],col=rgb(1,1-
diff.minmax[i],1-diff.minmax[i]),lwd=2)
 }

 ## Add legend
 legend3d("topright", legend = paste('Principal   component',
axis1, c('positive loadings','negative loadings')), pch = 16, col =
c("blue", "orange"), cex=1, inset=c(0.02))

### Perform PLSDA ###
# Training and test sets #

LM.plsda=matrix(ncol=dim(LM.proc.coords)[3],nrow=length(LM
.proc.coords[,,1]))

for (i in 1:dim(LM.proc.coords)[3]){
 LM.plsda[,i]=as.vector(t(LM.proc.coords[,,i]))
}

LM.plsda=as.data.frame(t(LM.plsda))

## Order-level PLS-DA models ##

groups.plsda=order.lab
allClass <- factor(groups.plsda)

set.seed(107)
LM.plsdaTest = cbind(LM.plsda, allClass)
str(LM.plsdaTest)
```

```r
inTrain <- createDataPartition(
  y = LM.plsdaTest$allClass,
  ## the outcome data are needed
  p = .75,
  ## The percentage of data in the
  ## training set
  list = FALSE
)

training <- LM.plsdaTest[ inTrain,]
testing  <- LM.plsdaTest[-inTrain,]

nrow(training)
nrow(testing)
```

 # Model 1: Bootstrap (order-level) #
```r
ctrl <- trainControl(
  method = "boot",
  number = 25,
  classProbs = TRUE,
  summaryFunction = twoClassSummary
)

set.seed(123)
OrdModel1 <- train(
  allClass ~ .,
  data = training,
  method = "pls",
  preProc = c("center", "scale"),
  tuneLength = 20,
  ## added:
  trControl = ctrl,
  metric = "ROC"
)

OrdModel1
```

 # Model 2: Repeated CV (order-level) #
```r
ctrl <- trainControl(
  method = "repeatedcv",
  repeats = 10,
  number = 3,## resampling method
  classProbs = TRUE, ## Since the ROC curve is based on the
predicted class probabilities (which are not computed
automatically), another option is required. The classProbs =
TRUE option is used to include these calculations.
  summaryFunction = twoClassSummary ## summaryFunction
argument takes the observed and predicted values and
estimates some measure of performance
)

set.seed(123)
OrdModel2 <- train(
  allClass ~ .,
  data = training,
  method = "pls",
  preProc = c("center", "scale"),
  tuneLength = 20,
  trControl = ctrl,
  metric = "ROC"
)
OrdModel2
```

Predict new samples using test set
 # Model 1 (order-level)
```r
plsClasses <- predict(OrdModel1, newdata = testing)
#predictions of test set using model
str(plsClasses)
```

```r
plsProbs <- predict(OrdModel1, newdata = testing, type =
"prob") ## type = "prob" can be used to compute class
probabilities from the model.
head(plsProbs)
caret::confusionMatrix(data =     plsClasses,   testing$allClass,
positive = "Sphenisciformes") ## confusion matrix and
associated statistics for the model fit.
```

 # Model 2 (order-level)
```r
plsClasses <-   predict(OrdModel2,   newdata =   testing)
#predictions of test set using model
str(plsClasses)
plsProbs <- predict(OrdModel2, newdata = testing, type =
"prob") ## type = "prob" can be used to compute class
probabilities from the model.
head(plsProbs)
caret::confusionMatrix(data =     plsClasses,   testing$allClass,
positive = "Sphenisciformes") ## confusion matrix and
associated statistics for the model fit.
```

Family-level PLS-DA models
```r
groups.plsda=family.lab
allClass <- factor(groups.plsda)

set.seed(107)
LM.plsdaTest = cbind(LM.plsda, allClass)
str(LM.plsdaTest)

inTrain <- createDataPartition(
  y = LM.plsdaTest$allClass,
  ## the outcome data are needed
  p = .75,
  ## The percentage of data in the
  ## training set
  list = FALSE
)

training <- LM.plsdaTest[ inTrain,]
testing  <- LM.plsdaTest[-inTrain,]

nrow(training)
nrow(testing)
```

 # Model 1: Bootstrap (family-level) #
```r
ctrl <- trainControl(
  method = "boot",
  classProbs = TRUE,
  number = 25,
  summaryFunction = defaultSummary
)

set.seed(123)
FamModel1 <- train(
  allClass ~ .,
  data = training,
  method = "pls",
  preProc = c("center", "scale"),
  tuneLength = 20,
  ## added:
  trControl = ctrl
)
FamModel1
```

 # Model 2: Repeated CV (family-level) #
```r
ctrl <- trainControl(
  method = "repeatedcv",
  repeats = 10,
  number = 3,## resampling method
  classProbs = TRUE, ## Since the ROC curve is based on the
predicted class probabilities (which are not computed
```

automatically), another option is required. The classProbs = TRUE option is used to include these calculations.
  summaryFunction = defaultSummary ## summaryFunction argument takes the observed and predicted values and estimates some measure of performance
)

```
set.seed(123)
FamModel2 <- train(
  allClass ~ .,
  data = training,
  method = "pls",
  preProc = c("center", "scale"),
  tuneLength = 20,
  trControl = ctrl
)
FamModel2
```

Predict new samples using test set
Model 1 (family-level)
```
plsClasses <- predict(FamModel1, newdata = testing)
#predictions of test set using model
str(plsClasses)
plsProbs <- predict(FamModel1, newdata = testing, type = "prob") ##  type = "prob" can be used to compute class probabilities from the model.
head(plsProbs)
caret::confusionMatrix(data = plsClasses, testing$allClass) ## confusion matrix and associated statistics for the model fit.
```

Model 2 (family-level)
```
plsClasses <- predict(FamModel2, newdata = testing)
#predictions of test set using model
str(plsClasses)
plsProbs <- predict(FamModel2, newdata = testing, type = "prob") ##  type = "prob" can be used to compute class probabilities from the model.
head(plsProbs)
caret::confusionMatrix(data = plsClasses, testing$allClass) ## confusion matrix and associated statistics for the model fit.
```

Appendix F

F.1   PLS-DA models

Table F.1. Order-level PLS-DA optimal model fits based on femur shape. Model 1 (number of components = 1, n = 142), model 2 (ncomp = 1, n = 95). ROC = (area under the) receiver operating characteristic (curve).

	Resampling method	ROC	Sensitivity (%)	Specificity (%)
Model 1	Bootstrapped (25 repeats)	1	100	99
Model 2	Cross-Validated (3-fold, repeated 10 times)	1	100	99

Table F.2. Family-level PLS-DA optimal model fits based on femur shape. Model 1 (ncomp = 6, n = 142), model 2 (ncomp = 6, n = 94).

	Resampling method	Accuracy (%)
Model 1	Bootstrapped (25 repeats)	96.7
Model 2	Cross-Validated (3-fold, repeated 10 times)	96.8

Appendix G

G.1   Genus-level morphospace

Figure G.1. Morphospace reflecting disparity in the shape of the femur from tubenosed birds (Diomedeidae, Oceanitidae, Procellariidae) and penguins (Spheniscidae), as shown by scores from principal component analysis of Procrustes-transformed landmark data data (PC1 vs PC4). Specimens from selected genera are marked with distinct symbols to show how they cluster in this morphospace e.g. *Ardenna* ⊕ within Procellariidae. See key above for examples of these selected genera. 95% confidence ellipses ($a = 0.05$).

Appendix H

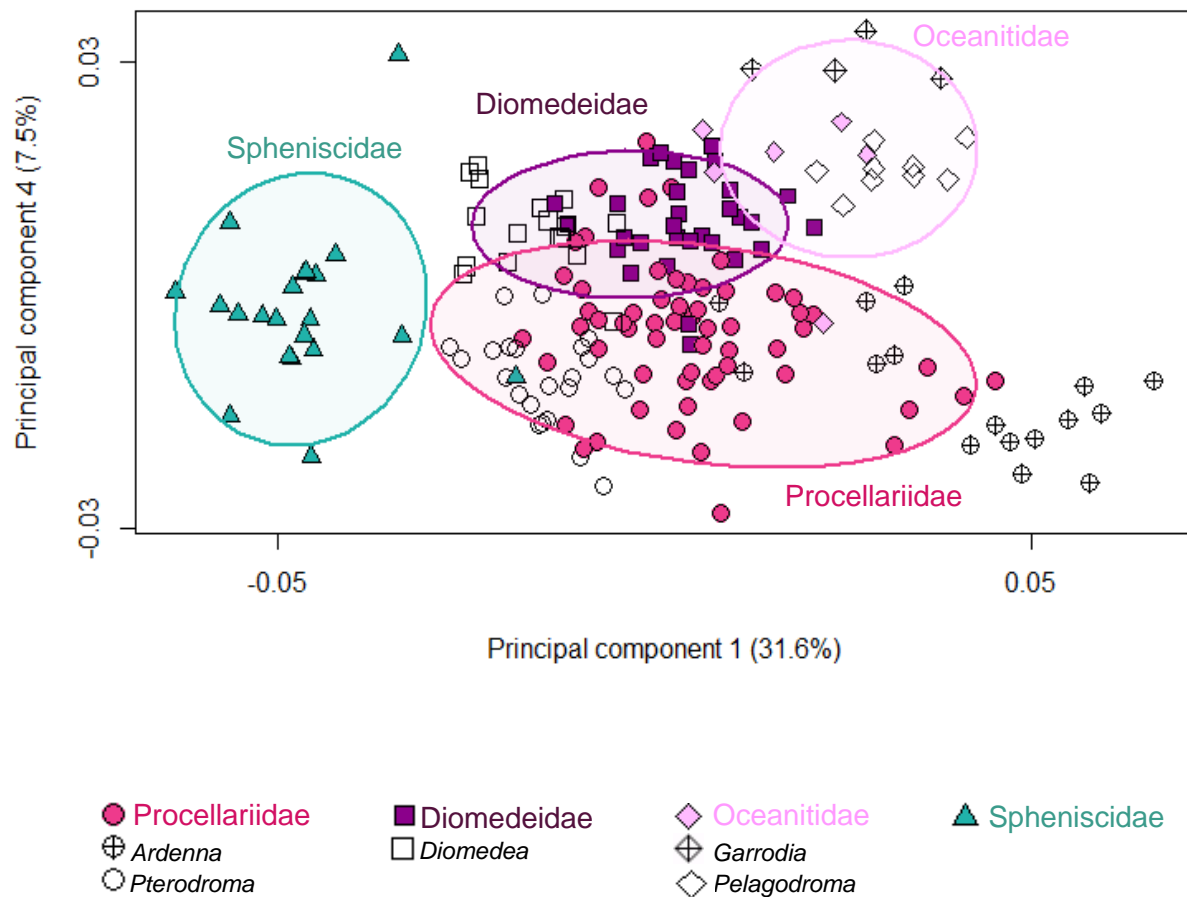## H.1   Genus-level morphospace

Figure H.1. Morphospace reflecting disparity in the shape of the femur from tubenosed birds (Diomedeidae, Oceanitidae, Procellariidae) and penguins (Spheniscidae), as shown by scores from principal component analysis of Procrustes-transformed pseudolandmark data (PC1 vs PC5). Specimens from selected genera are marked with distinct symbols to show how they cluster in this morphospace e.g. *Pterodroma* ◯ within Procellariidae. See key above for examples of these selected genera.
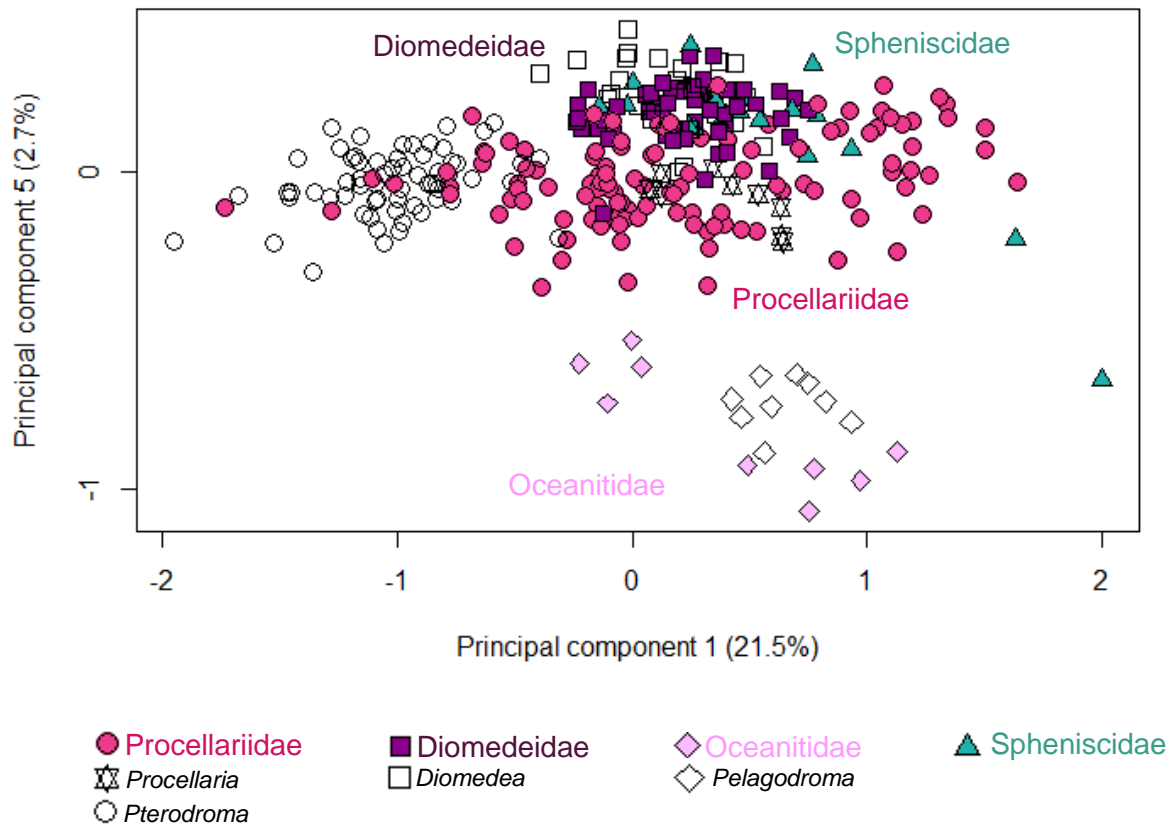
Figure H.2. Morphospace reflecting disparity in the shape of the humerus from tubenosed birds (Diomedeidae, Oceanitidae, Procellariidae) and penguins (Spheniscidae), as shown by scores from principal component analysis of Procrustes-transformed pseudolandmark data (PC2 vs PC3). Specimens from selected genera are marked with distinct symbols to show how they cluster in this morphospace e.g. *Pterodroma* ○ within Procellariidae. See key above for examples of these selected genera.
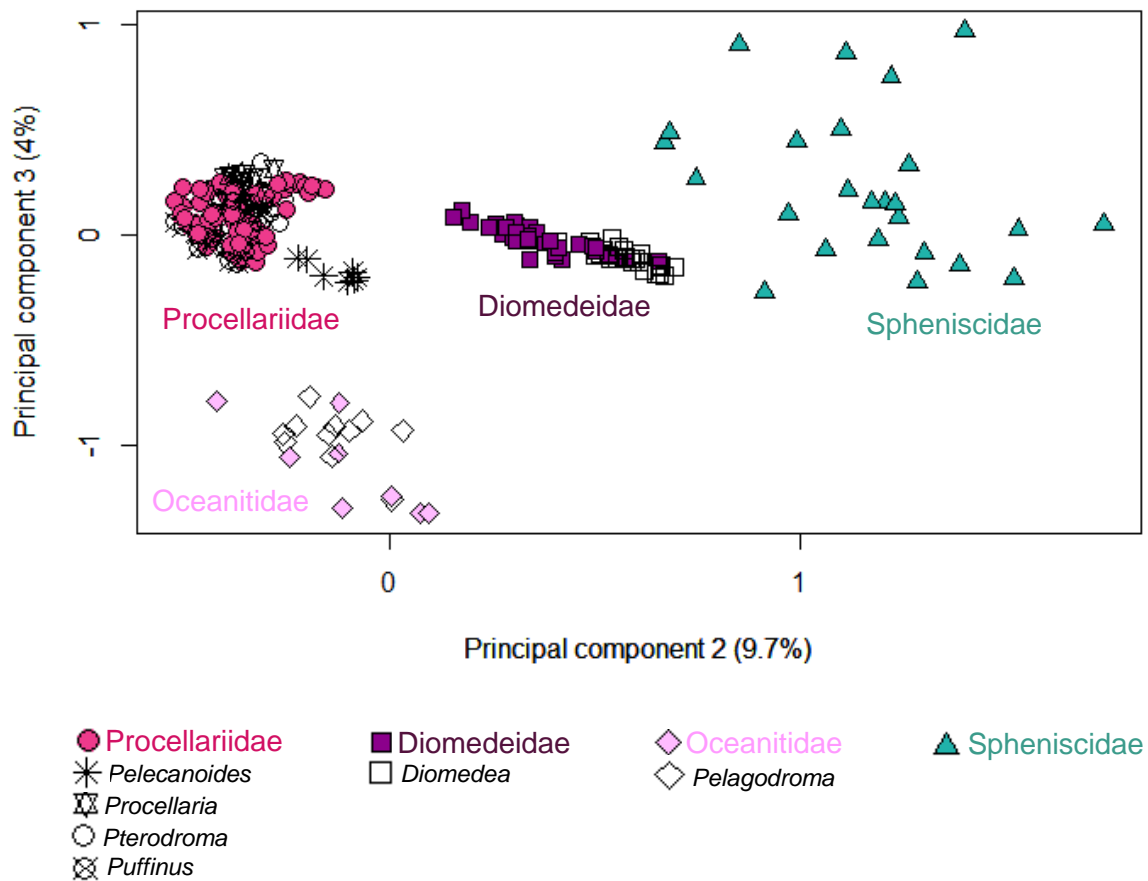
Appendix I

I.1 R code for GPSA pseudolandmark-based analyses

```r
## Required packages ##
library(Morpho)
#install.packages("rgl")
library(rgl)
#install.packages("Rvcg")
library(Rvcg)
#install.packages("xfun")
library(xfun)
#install.packages("promises")
library(promises)
#install.packages("mime")
library(mime)
#install.packages("fastmap")
library(fastmap)
library(Rvcg)
library(geomorph)
library(pls)
library(caret)
#install.packages("lifecycle")
library(lifecycle)
#install.packages("ellipsis")
library(ellipsis)
#install.packages("pkgconfig")
library(pkgconfig)
#install.packages("gower")
library(gower)
#install.packages("ModelMetrics")
library(ModelMetrics)
library(e1071)
library(abind)

wd="..." #update with relevant working directory
sp.list.step1 = list.files(wd, pattern = "*.ply")

#remove gpsa files from list
list.gpsa = which(substr(sp.list.step1, 1, 5) == "_gpsa")

## Generate labels and colors
if (length(list.gpsa) > 0) {
  sp.list = sp.list.step1[-which(substr(sp.list.step1, 1, 5) ==
"_gpsa")] #remove which ones have _gpsa as first five characters
} else {
  sp.list = sp.list.step1
}

# Genus labels
gen.list = c()
for (i in 1: length(sp.list)) {
  gen.list[i] = strsplit(sp.list, " ")[[i]][2]
}

# Just species
species.list = c()
for (i in 1: length(sp.list)) {
  species.list[i] = strsplit(sp.list, " ")[[i]][3]
}

# Species labels
sp.list2 = c()
for (i in 1: length(sp.list)) {
```

```r
sp.list[i] = paste(strsplit(sp.list, " ")[[i]][2], strsplit(sp.list, "
")[[i]][3])
 }

# Order
order.lab = gen.list
order.lab[which(match(order.lab, c("Ardenna", "Calonectris",
"Daption", "Pelecanoides", "Diomedea", "Thalassarche",
"Phoebetria", "Pachyptila", "Macronectes", "Pterodroma",
"Oceanites", "Garrodia", "Pelagodroma", "Phoebastria",
"Pagodroma", "Halobaena", "Puffinus", "Fulmarus",
"Procellaria", "Thalassoica", "Fregetta", "Aphrodroma",
"Lugensa", "Pachyptila", "Oceanodroma"), nomatch = 0) > 0)] =
"Procellariiformes"
order.lab[which(match(order.lab, c("Eudyptes", "Megadyptes",
"Spheniscus", "Pygoscelis", "Aptenodytes", "Eudyptula"),
nomatch = 0) > 0)] = "Sphenisciformes"

order.col = order.lab
order.col[which(order.lab    ==    "Sphenisciformes")]    =
"lightseagreen"
order.col[which(order.lab == "Procellariiformes")] = "violetred2"

# Family
family.lab = gen.list
family.lab[which(match(family.lab, c("Oceanodroma"), nomatch
= 0) > 0)] = "Hydrobatidae"
family.lab[which(match(family.lab,           c("Diomedea",
"Thalassarche", "Phoebetria", "Phoebastria"), nomatch = 0) > 0)]
= "Diomedeidae"
family.lab[which(match(family.lab, c("Oceanites", "Garrodia",
"Pelagodroma", "Fregetta"), nomatch = 0) > 0)] = "Oceanitidae"
family.lab[which(match(family.lab, c("Aphrodroma", "Puffinus",
"Ardenna", "Procellaria", "Macronectes", "Pterodroma",
"Pachyptila", "Halobaena", "Calonectris", "Thalassoica",
"Pelecanoides", "Daption", "Fulmarus", "Pagodroma",
"Lugensa", "Pachyptila"), nomatch = 0) > 0)] = "Procellariidae"
family.lab[which(match(family.lab,           c("Eudyptes",
"Megadyptes", "Spheniscus", "Pygoscelis", "Aptenodytes",
"Eudyptula"), nomatch = 0) > 0)] = "Spheniscidae"

family.col = family.lab
family.col[which(family.lab    ==    "Spheniscidae")]    =
"lightseagreen"
family.col[which(family.lab    ==    "Diomedeidae")]    =
"darkmagenta"
family.col[which(family.lab == "Hydrobatidae")] = "orange"
family.col[which(family.lab == "Oceanitidae")] = "plum1"
family.col[which(family.lab == "Procellariidae")] = "violetred2"

# Genus
gen.lab = gen.list
gen.lab[which(match(gen.lab, c("Diomedea"), nomatch = 0) > 0)]
= "Diomedea"
gen.lab[which(match(family.lab, c("Thalassarche"), nomatch =
0) > 0)] = "Thalassarche"
gen.lab[which(match(gen.lab, c("Phoebastria"), nomatch = 0) >
0)] = "Phoebastria"
gen.lab[which(match(gen.lab, c("Phoebetria"), nomatch = 0) >
0)] = "Phoebetria"
gen.lab[which(match(family.lab, c("Puffinus"), nomatch = 0) >
0)] = "Puffinus"
gen.lab[which(match(family.lab, c("Ardenna"), nomatch = 0) >
0)] = "Ardenna"
```

```
gen.lab[which(match(family.lab, c("Procellaria"), nomatch = 0) >
0)] = "Procellaria"
gen.lab[which(match(family.lab, c("Macronectes"), nomatch =
0) > 0)] = "Macronectes"
gen.lab[which(match(family.lab, c("Pterodroma"), nomatch = 0)
> 0)] = "Pterodroma"
gen.lab[which(match(family.lab, c("Pachyptila"), nomatch = 0) >
0)] = "Pachyptila"
gen.lab[which(match(family.lab, c("Halobaena"), nomatch = 0) >
0)] = "Halobaena"
gen.lab[which(match(family.lab, c("Calonectris"), nomatch = 0) >
0)] = "Calonectris"
gen.lab[which(match(family.lab, c("Thalassoica"), nomatch = 0)
> 0)] = "Thalassoica"
gen.lab[which(match(family.lab, c("Pelecanoides"), nomatch =
0) > 0)] = "Pelecanoides"
gen.lab[which(match(family.lab, c("Daption"), nomatch = 0) > 0)]
= "Daption"
gen.lab[which(match(family.lab, c("Fulmarus"), nomatch = 0) >
0)] = "Fulmarus"
gen.lab[which(match(family.lab, c("Pagodroma"), nomatch = 0)
> 0)] = "Pagodroma"
gen.lab[which(match(family.lab,    c("Oceanites    oceanicus"),
nomatch = 0) > 0)] = "Oceanites"
gen.lab[which(match(gen.lab, c("Garrodia"), nomatch = 0) > 0)]
= "Garrodia"
gen.lab[which(match(gen.lab, c("Pelagodroma"), nomatch = 0) >
0)] = "Pelagodroma"
gen.lab[which(match(gen.lab, c("Fregetta"), nomatch = 0) > 0)] =
"Fregetta"
```

Plotting symbols
Family
```
pch.vector = rep(0, length(family.lab))
pch.vector[which(family.lab == "Spheniscidae")] = 24
pch.vector[which(family.lab == "Diomedeidae")] = 21
pch.vector[which(family.lab == "Oceanitidae")] = 21
pch.vector[which(family.lab == "Procellariidae")] = 21
pch.legend.fam = c(21, 21, 21, 24)

cex.vector = rep(0, length(family.lab))
cex.vector[which(family.lab == "Spheniscidae")] = 1.2
cex.vector[which(family.lab == "Diomedeidae")] = 1.5
cex.vector[which(family.lab == "Oceanitidae")] = 1.5
cex.vector[which(family.lab == "Procellariidae")] = 1.5
```

Genus
```
pch.vector3=rep(0,length(gen.lab))
pch.vector3[which(gen.lab=="Diomedea")]=0
pch.vector3[which(gen.lab=="Thalassarche")]=22
pch.vector3[which(gen.lab=="Phoebastria")]=22
pch.vector3[which(gen.lab=="Phoebetria")]=22
pch.vector3[which(gen.lab=="Aphrodroma")]=21
pch.vector3[which(gen.lab=="Puffinus")]=13
pch.vector3[which(gen.lab=="Ardenna")]=21
pch.vector3[which(gen.lab=="Procellaria")]=11
pch.vector3[which(gen.lab=="Macronectes")]=21
pch.vector3[which(gen.lab=="Pterodroma")]=1
pch.vector3[which(gen.lab=="Pachyptila")]=21
pch.vector3[which(gen.lab=="Halobaena")]=21
pch.vector3[which(gen.lab=="Calonectris")]=21
pch.vector3[which(gen.lab=="Thalassoica")]=21
pch.vector3[which(gen.lab=="Pelecanoides")]=8
pch.vector3[which(gen.lab=="Daption")]=21
pch.vector3[which(gen.lab=="Fulmarus")]=21
pch.vector3[which(gen.lab=="Pagodroma")]=21
pch.vector3[which(gen.lab=="Oceanites")]=23
pch.vector3[which(gen.lab=="Garrodia")]=23
pch.vector3[which(gen.lab=="Pelagodroma")]=11
pch.vector3[which(gen.lab=="Fregetta")]=23
pch.vector3[which(gen.lab=="Aptenodytes")]=24
```

```
pch.vector3[which(gen.lab=="Eudyptula")]=24
pch.vector3[which(gen.lab=="Eudyptes")]=24
pch.vector3[which(gen.lab=="Megadyptes")]=24
pch.vector3[which(gen.lab=="Pygoscelis")]=24
pch.vector3[which(gen.lab=="Spheniscus")]=24

cex.vector3=rep(0,length(gen.lab))
cex.vector3[which(gen.lab=="Diomedea")]=1.4
cex.vector3[which(gen.lab=="Thalassarche")]=1.4
cex.vector3[which(gen.lab=="Phoebastria")]=1.4
cex.vector3[which(gen.lab=="Phoebetria")]=1.4
cex.vector3[which(gen.lab=="Puffinus")]=1.5
cex.vector3[which(gen.lab=="Aphrodroma")]=1.5
cex.vector3[which(gen.lab=="Ardenna")]=1.5
cex.vector3[which(gen.lab=="Procellaria")]=1.1
cex.vector3[which(gen.lab=="Macronectes")]=1.5
cex.vector3[which(gen.lab=="Pterodroma")]=1.5
cex.vector3[which(gen.lab=="Pachyptila")]=1.5
cex.vector3[which(gen.lab=="Halobaena")]=1.5
cex.vector3[which(gen.lab=="Calonectris")]=1.5
cex.vector3[which(gen.lab=="Thalassoica")]=1.5
cex.vector3[which(gen.lab=="Pelecanoides")]=1.5
cex.vector3[which(gen.lab=="Daption")]=1.5
cex.vector3[which(gen.lab=="Fulmarus")]=1.5
cex.vector3[which(gen.lab=="Pagodroma")]=1.5
cex.vector3[which(gen.lab=="Oceanites")]=1.3
cex.vector3[which(gen.lab=="Garrodia")]=1.3
cex.vector3[which(gen.lab=="Pelagodroma")]=1.1
cex.vector3[which(gen.lab=="Fregetta")]=1.3
cex.vector3[which(gen.lab=="Aptenodytes")]=1.2
cex.vector3[which(gen.lab=="Eudyptula")]=1.2
cex.vector3[which(gen.lab=="Eudyptes")]=1.2
cex.vector3[which(gen.lab=="Megadyptes")]=1.2
cex.vector3[which(gen.lab=="Pygoscelis")]=1.2
cex.vector3[which(gen.lab=="Spheniscus")]=1.2
```

Read GPSA pseudolandmarks into R, e.g:
```
femora=fread(list.files(wd,           pattern            =
"gpsa_homologized_points.dat", full.names = T))
```

Format pseudolandmarks into useable matrix, e.g.:
```
femora.m=matrix(as.numeric(unlist(femora)),nrow=dim(femora
)[1])
```

Run PCA in R on pseudolandmark matrix, e.g.:
```
femora.pc=prcomp(femora.m)
femora.loadings=femora.pc$rotation
femora.scores=femora.pc$x

eigenval=femora.pc$sdev^2
explained=round(eigenval/sum(eigenval) * 100, digits = 1)
plot(explained, type = "b", pch = 16, ylab = "Explained variance
        (%)", xlab = "Principal component", xlim = c(0,20))
cumsum(explained)

PCx=1
PCy=2

femora.scores.PCx=femora.scores[,PCx]
femora.scores.PCy=femora.scores[,PCy]
femora.loadings.PCx=femora.loadings[,PCx]
femora.loadings.PCy=femora.loadings[,PCy]
```

Screeplot
```
plot(explained, type = "b", pch = 16, ylab = "Explained variance
        (%)", xlab = "Principal component", xlim = c(0,20))
cumsum(explained)
```

Family-level PCA plot

```r
plot(femora.scores.PCx,femora.scores.PCy,cex=cex.vector,pch=
        pch.vector,font=5,xaxt='n',yaxt='n',ann=FALSE,col="
        black",bg=family.col,lwd=1)
axis(1,at=c(-4:4))
axis(2,at=c(-4:4))
title(xlab=paste("Principal        component        ",   PCx,    "
        (",explained[PCx],"%)",sep=""))
title(ylab=paste("Principal        component        ",   PCy,    "
        (",explained[PCy],"%)",sep=""))
```

Genus-level PCA plot
```r
plot(femora.scores.PCx,femora.scores.PCy,cex=cex.vector3,pch
        =pch.vector3,font=5,                          xaxt='n',
        yaxt='n',ann=FALSE,col="black",bg=family.col,lwd=1)
axis(1,at=c(-4:4))
axis(2,at=c(-4:4))
title(xlab=paste("Principal        component        ",   PCx,    "
        (",explained[PCx],"%)",sep=""))
title(ylab=paste("Principal        component        ",   PCy,    "
        (",explained[PCy],"%)",sep=""))
```

Ellipses
```r
for(seabird in unique(family.lab)[-5]){

            car::dataEllipse(femora.scores.PCx[which(family.lab
            ==seabird)],
            femora.scores.PCy[which(family.lab==seabird)],add=
            T,levels=0.75,center.pch=NULL, plot.points=F,

            col=family.col[which(family.lab==seabird)][1],fill=T,fi
            ll.alpha=0.05,ellipse.label=NULL)
}
plot3d(femora.scores[,1], femora.scores[,2], femora.scores[,3],
        xlab = "Principal component 1", ylab = "Principal
        component 2", zlab = "Principal component 3",
        col=family.col, size=6, box = FALSE)
legend("bottom",   legend =   unique(family.lab),   col   =
        c("darkmagenta",        "violetred2",       "plum1",
        "lightseagreen"), pch = c(16, 16, 16, 16), inset = -0.35,
        xpd = TRUE, horiz = TRUE, bty = "n")
```

Spinning 3Dscatterplot
```r
plot3d(femora.scores[,3], femora.scores[,4], femora.scores[,5],
xlab = "Principal component 3", ylab = "Principal component 4",
zlab = "Principal component 5", col=family.col, size=6, box =
FALSE, legend = TRUE, cex.legend = 1)

legend3d("bottom",   legend =   unique(family.lab),   col   =
        c("darkmagenta",        "violetred2",       "plum1",
        "turquoise3"), pch = 16, cex=1, inset=c(0.02), bty =
        "n")
```

Loadings
```r
ldPlot = function (fit, PC = 1) {
 m = fit$m
 ld = fit$loadings
 m.array = array(dim = c(ncol(m) / 3, 3, nrow(m)))
 for (i in 1: nrow(m)) {
  m.array[, , i] = matrix(m[i, ], ncol = 3, byrow = T)
 }

 nsample = dim(m.array)[3]
 nvert = dim(m.array)[1]

 A = m.array
 ref = mshape(A)

 loadings.bone = ld[, PC]
 loadings.PC = matrix(loadings.bone, ncol = 3, byrow = T)
 loadings.len = sqrt(((loadings.PC[, 1] ^ 2) + (loadings.PC[, 3] ^ 2))
        + (loadings.PC[, 2] ^ 2))
```

```r
 loadings.minmax   =   (loadings.len  -   min(loadings.len))   /
        (max(loadings.len) - min(loadings.len))

 plot3d(ref, add = F, col = rgb(loadings.minmax, 0.5, 1 -
        loadings.minmax), aspect = "iso", axes = F, xlab = "",
        ylab = "", zlab = "", size = 10)

 #legend3d("topright",  legend = paste('Principal component',
        PC, 'loadings'), pch = 16, cex = 1, inset = c(0.02))

}
```

Perform PLSDA
```r
# Training and test sets #

LM.plsda=matrix(ncol=dim(LM.proc.coords)[3],nrow=length(LM
.proc.coords[,,1]))

for (i in 1:dim(LM.proc.coords)[3]){
 LM.plsda[,i]=as.vector(t(LM.proc.coords[,,i]))
}

LM.plsda=as.data.frame(t(LM.plsda))
```

Order-level PLS-DA models
```r
groups.plsda=order.lab
allClass <- factor(groups.plsda)

set.seed(107)
LM.plsdaTest = cbind(LM.plsda, allClass)
str(LM.plsdaTest)

inTrain <- createDataPartition(
 y = LM.plsdaTest$allClass,
 ## the outcome data are needed
 p = .75,
 ## The percentage of data in the
 ## training set
 list = FALSE
)


training <- LM.plsdaTest[ inTrain,]
testing  <- LM.plsdaTest[-inTrain,]

nrow(training)
nrow(testing)
```

Model 1: Bootstrap (order-level)
```r
ctrl <- trainControl(
 method = "boot",
 number = 25,
 classProbs = TRUE,
 summaryFunction = twoClassSummary
)

set.seed(123)
OrdModel1 <- train(
 allClass ~ .,
 data = training,
 method = "pls",
 preProc = c("center", "scale"),
 tuneLength = 20,
 ## added:
 trControl = ctrl,
 metric = "ROC"
)

OrdModel1
```

Model 2: Repeated CV (order-level)

```
ctrl <- trainControl(
  method = "repeatedcv",
  repeats = 10,
  number = 3,## resampling method
  classProbs = TRUE, ## Since the ROC curve is based on the
predicted class probabilities (which are not computed
automatically), another option is required. The classProbs =
TRUE option is used to include these calculations.
  summaryFunction = twoClassSummary ## summaryFunction
argument takes the observed and predicted values and
estimates some measure of performance
)

set.seed(123)
OrdModel2 <- train(
  allClass ~ .,
  data = training,
  method = "pls",
  preProc = c("center", "scale"),
  tuneLength = 20,
  trControl = ctrl,
  metric = "ROC"
)
OrdModel2
```

Predict new samples using test set
Model 1 (order-level)

```
plsClasses  <-  predict(OrdModel1, newdata  =  testing)
#predictions of test set using model
str(plsClasses)
plsProbs <- predict(OrdModel1, newdata = testing, type =
"prob") ##  type = "prob" can be used to compute class
probabilities from the model.
head(plsProbs)
caret::confusionMatrix(data  =  plsClasses,  testing$allClass,
positive  =  "Sphenisciformes")  ##  confusion  matrix  and
associated statistics for the model fit.
```

Model 2 (order-level)

```
plsClasses  <-  predict(OrdModel2, newdata  =  testing)
#predictions of test set using model
str(plsClasses)
plsProbs <- predict(OrdModel2, newdata = testing, type =
"prob") ##  type = "prob" can be used to compute class
probabilities from the model.
head(plsProbs)
caret::confusionMatrix(data  =  plsClasses,  testing$allClass,
positive  =  "Sphenisciformes")  ##  confusion  matrix  and
associated statistics for the model fit.
```

Family-level PLS-DA models

```
groups.plsda=family.lab
allClass <- factor(groups.plsda)

set.seed(107)
LM.plsdaTest = cbind(LM.plsda, allClass)
str(LM.plsdaTest)

inTrain <- createDataPartition(
  y = LM.plsdaTest$allClass,
  ## the outcome data are needed
  p = .75,
  ## The percentage of data in the
  ## training set
  list = FALSE
)

training <- LM.plsdaTest[ inTrain,]
testing  <- LM.plsdaTest[-inTrain,]
```

```
nrow(training)
nrow(testing)
```

Model 1: Bootstrap (family-level)
```
ctrl <- trainControl(
  method = "boot",
  classProbs = TRUE,
  number = 25,
  summaryFunction = defaultSummary
)

set.seed(123)
FamModel1 <- train(
  allClass ~ .,
  data = training,
  method = "pls",
  preProc = c("center", "scale"),
  tuneLength = 20,
  ## added:
  trControl = ctrl
)
FamModel1
```

Model 2: Repeated CV (family-level)
```
ctrl <- trainControl(
  method = "repeatedcv",
  repeats = 10,
  number = 3,## resampling method
  classProbs = TRUE, ## Since the ROC curve is based on the
predicted class probabilities (which are not computed
automatically), another option is required. The classProbs =
TRUE option is used to include these calculations.
  summaryFunction = defaultSummary ## summaryFunction
argument takes the observed and predicted values and
estimates some measure of performance
)

set.seed(123)
FamModel2 <- train(
  allClass ~ .,
  data = training,
  method = "pls",
  preProc = c("center", "scale"),
  tuneLength = 20,
  trControl = ctrl
)
FamModel2
```

Predict new samples using test set
Model 1 (family-level)

```
plsClasses  <-  predict(FamModel1, newdata  =  testing)
#predictions of test set using model
str(plsClasses)
plsProbs <- predict(FamModel1, newdata = testing, type =
"prob") ##  type = "prob" can be used to compute class
probabilities from the model.
head(plsProbs)
caret::confusionMatrix(data = plsClasses, testing$allClass) ##
confusion matrix and associated statistics for the model fit.
```

Model 2 (family-level)

```
plsClasses  <-  predict(FamModel2, newdata  =  testing)
#predictions of test set using model
str(plsClasses)
plsProbs <- predict(FamModel2, newdata = testing, type =
"prob") ##  type = "prob" can be used to compute class
probabilities from the model.
head(plsProbs)
caret::confusionMatrix(data = plsClasses, testing$allClass) ##
confusion matrix and associated statistics for the model fit.
```